Maximum Torque Control of a High Speed Switched Reluctance Starter/Generator used in More/All Electric Aircraft

vorgelegt von
M.Sc. Minh Dinh Bui
aus Hanoi, Viet Nam

von der Fakultät IV- Elektrotechnik und Informatik
der Technischen Universität Berlin
Fachgebiet Elektrische Antriebstechnik

Doktor der Ingenieurwissenschaften
- Dr.-Ing. -

genehmigte Dissertation

Promotionsausschuss:

Vorsitzender: Prof. Dr.-Ing. Kai Strunz
Gutachter: Prof. Dr.-Ing. Uwe Schäfer
Gutachter: Prof. Dr.-Ing. Sibylle Dieckerhoff
Gutachter: Prof. Dr.-Ing. Nguyen Phung Quang
Tag der wissenschaftlichen Aussprache: 27.03.2014

Berlin 2014
D83

ACKNOWLEDGEMENTS

This dissertation is the crop yielded from my work at the Department of Electrical Drives (EA) in TU-Berlin. From the very first day at EA, many people have come into my life and given direct or indirect contributions to my research. To all of them, I am most grateful and wish to acknowledge in the following. First of all, I would like to thank my supervisor, Professor Dr.-Ing. Uwe Schaefer for his valuable advice on the dissertation, his continued guidance and support during the completion of the work, and the careful reviews of the simulation and measurement results. Due to his expertise in the switched reluctance machine, I could start the scientific research in the right direction and complete the work successfully. I also would like to thank Mr. Jürgen Federspiel, Mr. Arno Hellemann, Dr. Thomas Wörther, Mr. Hartmut Zutsch and Mr. Dirk Fischer for their assistance and concerns. I would like to express my gratitude to my colleagues Mr. Jan-Philipp von Klitzing, Mr. Alexander Kreim, Mr. Lorenz Taus Beti, Mr. Christian Dinca, Mr. Andreas Amberger, Mr. Yingnan Wang, Mr. Mohammad-Ali Sarmadi, Mr. Stefan Hoffmann, Mr. Simon Schneider, Mr. Samy Arnaout and Mr. Daniel Kreuzer from whom I have learned a lot and who supported me during 4 years. I would like to thank Prof. Dr.-Ing. Sibylle Dieckerhoff and Prof. Dr.-Ing.habil. Nguyen Phung Quang for the their comments and reviews. I also would like to thank the German Academic Exchange Service (DAAD) and Vietnamese International Education Development (VIED) for their supporting of my studies in Germany. Most of all, I would like to express deep gratitude to my wife and my parents who have provided endless encouragement.

Kurzfassung

Die vorliegende Dissertation behandelt die Drehmomentregelung eines hochdrehenden Switched Reluctance Starter-Generators (SR S/G) für die Anwendung in Flugzeugen. Das Starter-Generatorsystem ist für ein konstantes Drehmoment von 15 Nm bis zur Drehzahl von 27.000 min^{-1} im Starterbetrieb und für eine konstante Leistung von 30 kW bis zur Drehzahl von 50.000 min^{-1} im Generatorbetrieb sowie eine Bordnetzspannung von 270 V spezifiziert.

Im ersten Kapitel wird ein Überblick über die Literatur gegeben Darauf folgt eine Motivation aufgrund offener Forschungsfragen, die insbesondere eine optimierte Regelung unter Berücksichtigung der nichtlinearen magnetischen Eigenschaften von SRM betreffen.

Im zweiten Kapitel wird ein 2D-FEA Modell vorgestellt, mit dem die Flussverkettung und das innere Drehmoment der SRM berechnet werden können. Diese Simulationen werden durch experimentelle Ergebnisse unter Berücksichtigung der Ummagnetisierungsverluste ergänzt.

In Kapitel 3 werden Methoden zur Bestimmung der Ummagnetisierungsverluste und zur thermischen Analyse der SRM vorgestellt. Erstere ergeben sich durch Simulation auf Basis der Flussdichten in Stator und Rotor. Im nächsten Teil wird ein thermische Analyse auf Basis von Näherungsformeln und CFD-Simulation durchgeführt.

Kapitel 4 behandelt eine Regelungsstrategie zur Maximierung des Drehmoments. Die rechnerisch optimierten Schaltwinkel werden in einer Look-Up-Tabelle für im experimentellen Aufbau gespeichert. Die Evaluation erfolgt auf Basis eines speziell für hochdrehende Antriebe geeigneten Drehmomentmessverfahrens, welches auf Beschleunigungsmessungen basiert. Die Leistung im Generatorbetrieb ergibt sich analog durch einen Abbremsversuch.

Kapitel 5 fasst nochmals die wesentlichen Ergebnisse der Arbeit zusammen.

Abstract

The maximum torque control has an important role in improving the torque performances of a high speed Switched Reluctance Starter/Generator (SR S/G) drive system. Especially for high speed switched reluctance drives, optimal torque control is a big challenge due to the non-linear magnetization characteristics of the flux and electromagnetic torque with the current and rotor position. To realize the maximum torque control strategy, some improved measurement techniques were used to characterize performance and optimized control parameters were applied to maximize the starting torque by an experimental setup. Many electronics and mechanical design ideas have been implemented to set up the test bench. The SR S/G performances have been obtained in starting and generating modes within a wide speed range of up to 47,000 rpm.
High speed machines engineering spans multiple different high technologies. Some problems have occurred due to mechanical and electromagnetic structures, rotor bearings, power electronics and control methods, which will be treated in the appropriate chapters. The main contributions of this thesis are pointed out as follows:

1. The flux linkage and electromagnetic torque characteristics have been calculated by a FEA simulation method. The results have been validated by experiments with adequate measurement techniques which can remove iron loss current to improve the accuracy of the measurement method.

2. The iron losses calculation method for the high speed and flux density of the SRMs have been investigated by simulation and experiment. Based on the iron loss density of the SRM rotor and stator parts, the iron losses of the different components can be determined in both simulation and experimental models. Afterward, a thermal model of the SRM stator directly cooled the forced water system has been developed and verified experimentally.

3. The maximization of the average torque has been implemented by optimizing the turn-on and turn-off angles, torque and current controllers. The torque performance was validated by an indirect torque measurement based on the acceleration method. The torque performance was proven by the acceleration test and the results meet the requirements of the SR S/G performance.

4. The electric power of the switched reluctance generator has been measured by the deceleration test. The optimal turn-on and turn-off angles vs current and speed have been investigated to maximize the output power experimentally.

5. Conclusion and further work

Fig 0.1 shows the test bench for the three phase SR S/G including an additional inertia load, which was used to investigate torque and power performance in both motor and generator mode.

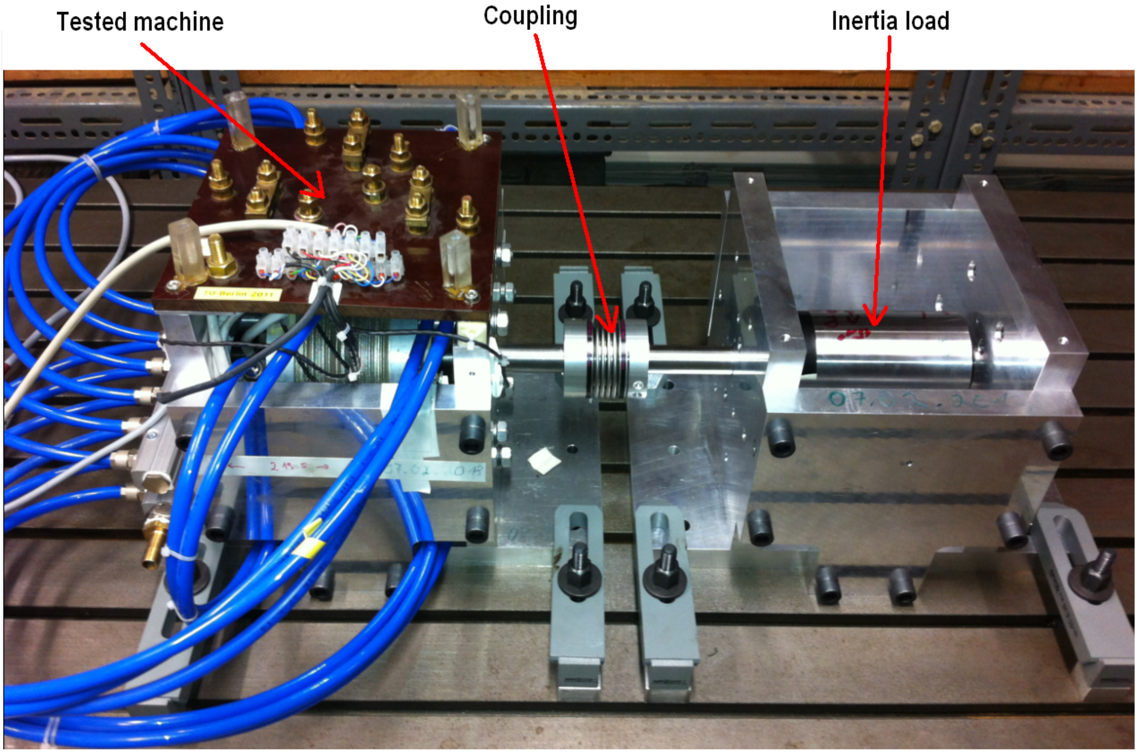

Figure 0.1: The setup of the SR S/G test bench

Contents

1 Introduction

1.1 Electrical Machines and Drives in More Electric Aircrafts

The More Electric Aircraft (MEA) is well known as an innovative concept to drive aircraft subsystems. Some mechanical, hydraulic and pneumatic drive subsystems have already been replaced by the electrical drives for several decades. The switched reluctance machines are considered to be a potential candidate for application as actuators, fuel pumps and other drive subsystems. In a typical configuration, the aircraft drive subsystems are fed from the auxiliary power unit (APU) via a secondary power system being either mechanical, or hydraulic, or electric [3], [12], and [13]. According to the more electric aircraft report in [1], the MEA was anticipated to achieve numerous advantages like higher performance and lower maintenance costs. Moreover, the emission of air pollutant gases from aircraft is reduced significantly. Recently, the aircraft industry has achieved tremendous progress in both civil and military sectors. Currently, some commercial aircrafts operate at weights of over 300,000 kg and are able to fly up to 16,000 km in non-stop journey at a speed of 1000 km/h [1].

The conventional aircraft has some drawbacks due to the complex power architecture. The primary power comes mainly from generators, batteries or ground sources. The secondary power of hydraulic, pneumatic, electrical and mechanical forms is supplied to subsystems such as landing gear, braking and flight control system, air conditioning, pressurization, deicing and avionics as shown in fig. 1.1 (a). Those disadvantages cause complexity, lower safety and higher volume. Therefore, the aircraft manufacturers trend towards the More Electric Aircraft (MEA) concept that is the wider adoption of electrical systems in preference to the others. A typical switched reluctance starter/generator system used in aircraft is shown in fig. 1.1 (b).

In order to reduce the complexity and improve the efficiency and reliability, some subsystems such as Environmental Control Systems (ECS), Ram Air Turbine (RAT) and High Pressure Air (HP Air) have been removed. The Start Air and Wing Anti-Ice Air are replaced by the Electric Start and the Electrical Wing Anti-Ice. The Auxiliary Power Unit (APU) is finally improved by a new design in fig. 1.1 (b)

1.1.1 Integral Starter/Generator (IS/G) topologies

Several electrical machine types being able to operate as high power starter/generator can be attached directly to the engine, mounted on the engine shaft, and used for the engine start in Integral Starter/Generator (IS/G) scheme [1]. Those machines will have to work in harsh operating conditions, and at high ambient temperatures, which require more innovative

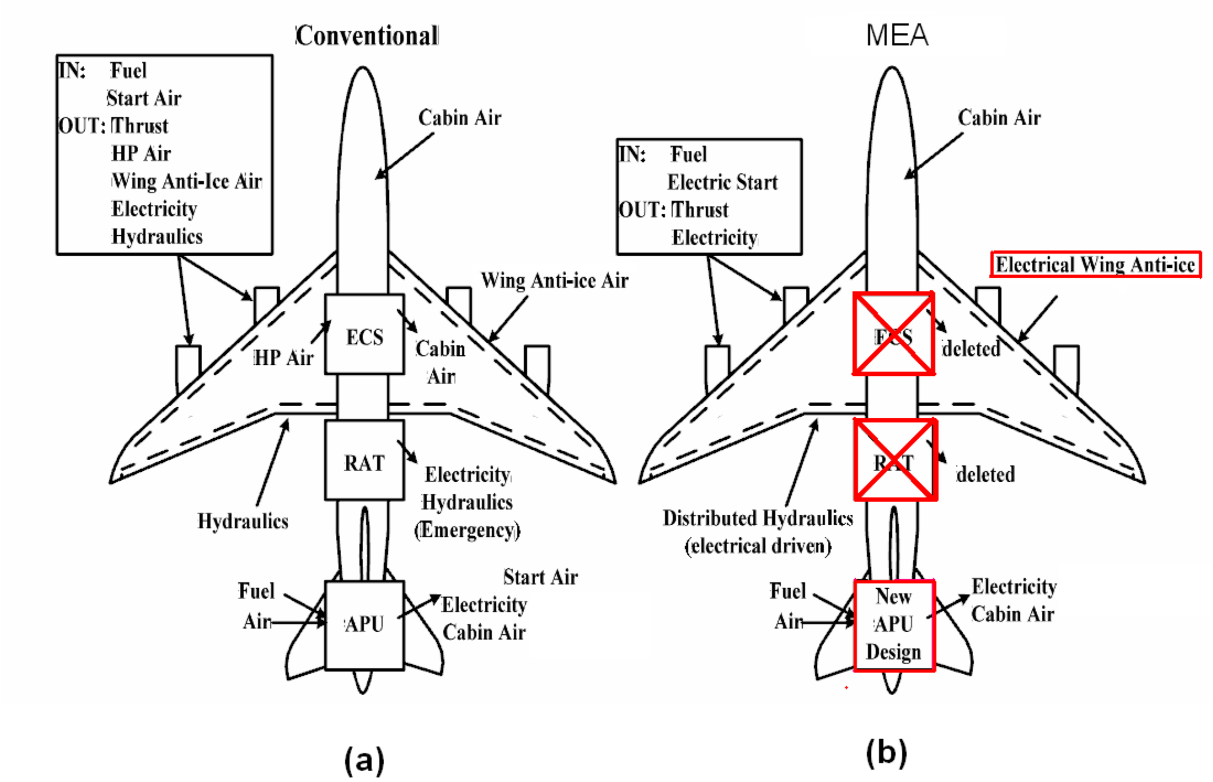

Figure 1.1: Comparison between conventional aircraft system (a) and MEA system (b) [1]

materials, processes and thermal management designs. Consequently, Switched Reluctance, Synchronous, Permanent Magnet, and Induction machine types have been considered for the MEA application due to their properties.

Switched Reluctance Generator (SRG):

The Switched Reluctance Generator has a very simple robust structure and can operate over a wide speed range. The three-phase type has a salient rotor similar to a salient pole synchronous machine. The stator consists of three phases and each phase is interfaced with the DC supply through two pairs of anti-parallel switch-diode combinations. Thus, the SR machine is inherently fault-tolerant. However, the machine has the disadvantages of producing high acoustic noise and torque ripple. Those drawbacks are of minor importance when the machine is mounted close to a noisy turbine. They can be improved by current and torque control methods in [10], [11].

Synchronous Generator (SG):

This machine is reliable and inherently safe because the field excitation can be removed. Synchronous generators of moderate power rating up to 150 kVA have been used for many aircrafts including e. g. the A320. The synchronous machine has the ability to generate reactive power, which enhances the stability of the aircraft power system. However, this machine requires an external DC excitation, which unfortunately decreases the reliability and the efficiency.

Permanent Magnet Generator (PMG):

The Permanent Magnet Generator (PMG) has some favourable characteristics such as rotor loss reduction, high power density and self excitation. However, conventional PM machines are claimed to have inferior fault tolerance compared with SR machines. The conventional PMG is intolerant to elevated temperatures. Those drawbacks have to be improved upon if they are to be used in the MEA system.

Induction Generator (IG):

Induction Generators (IGs) are characterized by their robustness, reduced cost, safety and ability to withstand harsh environments. However, the IGs include complex power electronics, because the induction machine requires more complicated control methods in comparison with other types of machines.

After different machine topologies are suggested for the IS/G, the SR and fault tolerant PM machines are most reliable. These machines do not require external excitation or sophisticated control techniques. Also, they are either inherently or artificially fault-tolerant.

1.1.2 Electrical Power Distribution

The power distribution system of civil aircrafts such as Boeing B747 and Airbus A320 combine both AC and DC transmission in parallel. An AC supply of 115V/400Hz is used to power large loads such as galleys, while the DC supply of 28V DC is used for avionics, flight control and battery-driven vital services [1].
In recent aircrafts, the generator power capabilities are 1.4 MW for the more electric Boeing B787 Dreamliner and 850kW for the Airbus. In order to reduce weight, electrical power should be transmitted around the aircraft at a higher voltage resulting in low current and low conduction losses [3]. Therefore, the generation and distribution voltage in these advanced aircrafts are mainly 270 V DC, 230 V AC at variable frequency, and 28 V DC for low power loads ([6] - [9]) due to several reasons:

- New generation options as variable frequency machines become feasible.
- Recent advances in the areas of interfacing circuits, control techniques, and protection systems.

- The advantages for DC distribution systems include reduction of the weight, size and losses, while increasing the levels of the transmitted power. The values of the system voltage under research are 270VDC. The value is determined by a number of factors such as the capabilities of DC switchgear and the availability of the components.

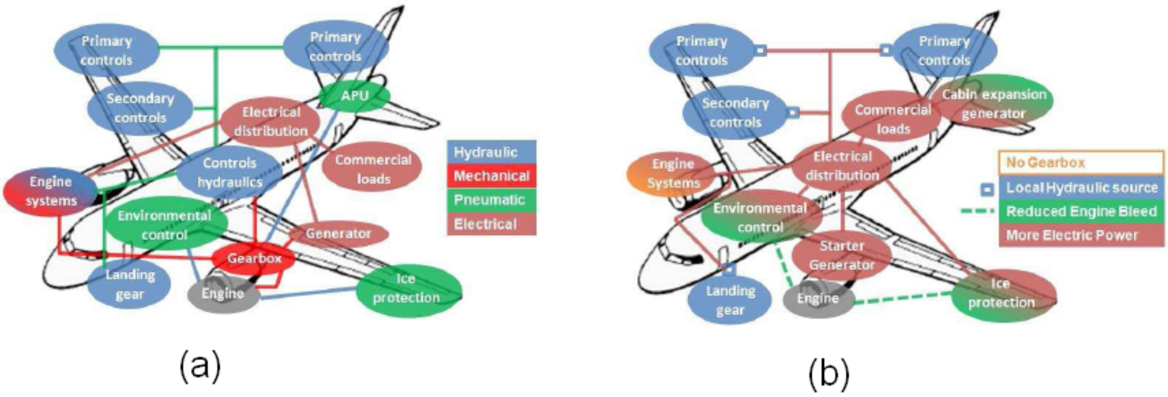

Figure 1.2: Schematic power distribution systems of the conventional aircraft (a) and the MEA (b) [2]

In comparison with the power distribution systems of the conventional aircraft in fig 1.2(a), the MEA in fig 1.2 (b) has some advantages such as:

- Removal of a conventional air starter as the engine is started electrically.
- Elimination of gearboxes and associated drive shafts by the direct coupling of generators to engine shafts.
- Exchange of traditional hydraulic actuators for electro-hydraulic and electro-mechanical actuators to increase reliability, eliminating the central hydraulic system and reduce maintenance.

Some different topologies were suggested for implementing the distribution system in MEA. In the following, four main candidates of these topologies are briefly reviewed:

- The Centralized Electrical Power Distribution System (CEPDS) is a point-to-point radial power distribution system as shown in fig 1.3 (a). It has only one distribution centre. The CEPDS is cumbersome, expensive and unreliable, as each load has to be wired from the avionics bay.
- The Semi-Distributed Electrical Power Distribution System (SDEPDS) has a large number of Power Distribution Centres (PDCs) as shown in fig 1.3 (b). The SDEPDS was proposed to overcome the problems of CEPDS. However, the close coupling between the loads in SDEPDS may reduce the reliability, as faults or disturbances can propagate to nearby loads.
- The Advanced Electrical Power Distribution System (AEPDS) is a flexible, fault-tolerant system controlled by a redundant microprocessor system. This system is developed to replace the conventionally centralized and semi-distributed systems.

- The Fault-Tolerant Electrical Power Distribution System (FTEPDS) is a mixed distribution system. The AC power from generators is connected to a source switch matrix, while the 270 V DC system is interfaced with the converters. An FTEPDS achieves some advantages such as fault tolerance, high redundancy, and ability to start the aircraft engine by a generator/starter scheme. However, the FTEPDS has one serious drawback because a fault in source/load switch matrices may interrupt the operation of the entire system.

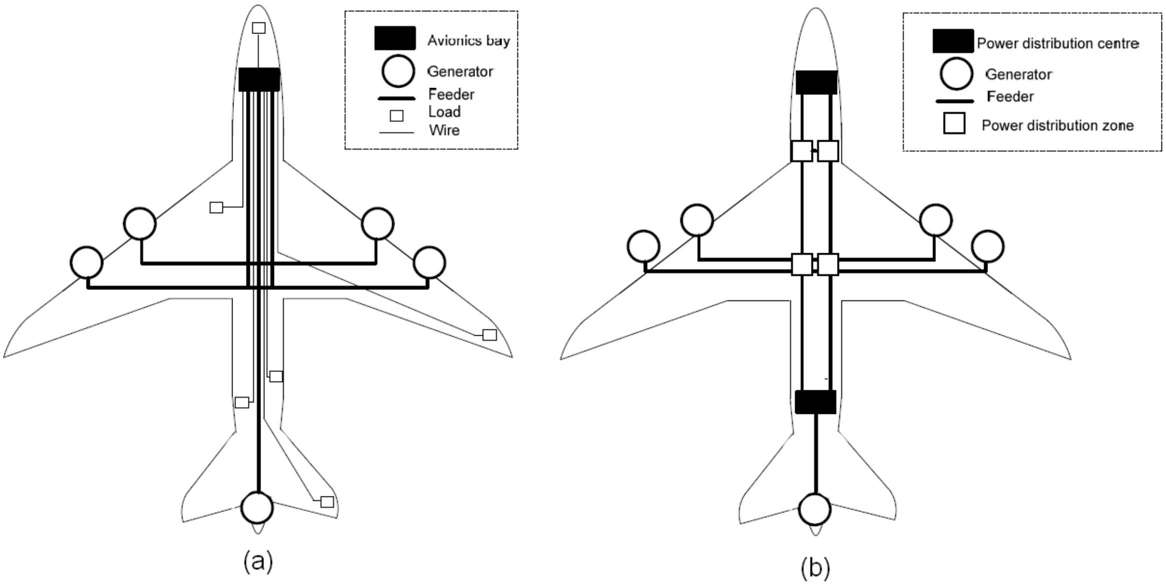

Figure 1.3: Centralized Electrical Power Distribution System CEPDS (a) and Semi-Distributed Electrical Power Distribution System (b) SDEPDS for the MEA [1]

1.1.3 The Switched Reluctance Starter/Generator (SR S/G) Drive System Requirement

The Switched Reluctance Starter/Generator (SR S/G) provides two primary functions. In starter operation, the 270 V DC bus supplies the electric power to the reluctance machine through the converter, thus accelerating the aircraft engine until it has achieved idle speed. In generator operation, the gas turbine acts as prime mover. The output electric power supplies to the DC bus in the aircraft. The technical parameters required were listed in [43] as below:

- Engine start:
    1. Constant torque 15 Nm up to 27,000 rpm
    2. Up to 40 s start duration (from zero to 27,000 rpm).

    3. 270 V DC, 30 kW.

- Power generation:
    1. 270 V DC, 30 kW .
    2. Continuous operation from 27,000 rpm to 50,000 rpm.
    3. 45 kW (1.5 pu) operation for 5 s.
- Power quality: MIL-STD-704E.
- Load types:
    1. 75% constant power loads.
    2. 25% resistive loads.
- Load profile: 30% (9 kW) load steps.
- Environment: operation temperature -51^{o}C to 121^{o}C.

According to the analysis of the engine starting process and the important performance parameters above, fig 1.4 shows the approximate requirements on torque-speed characteristics of the SR S/G for the electric aircraft.
During the engine start, the reluctance machine operates as a starter to supply a constant torque 15 Nm with the speed from standstill to 27,000 rpm. Once the engine has reached its idle speed of 27,000 rpm, the SR S/G becomes a generator and supplies the DC voltage power to run other subsystems.

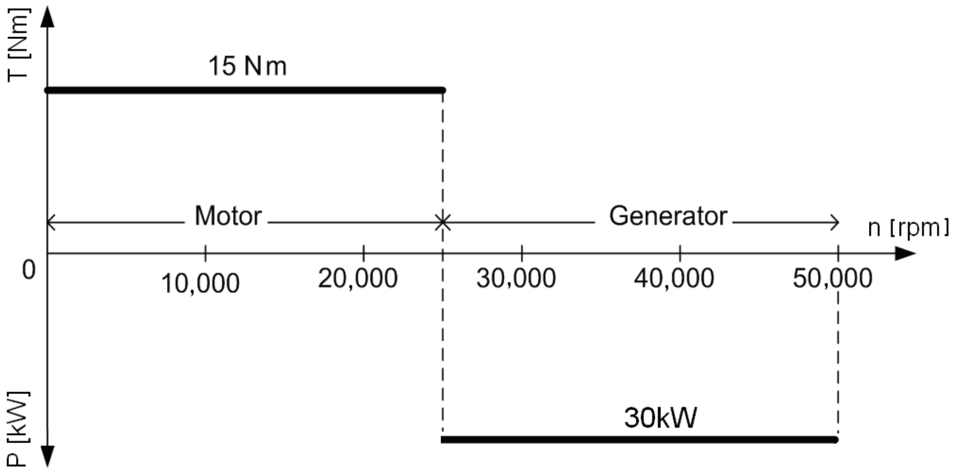

Figure 1.4: Performance requirements of SR S/G system [71]

1.2 Brief Overview of the Switched Reluctance Starter/Generator for the More Electric Aircraft Applications

Switched Reluctance Machines (SRMs) have been designed and built for an aircraft applications as reported in ([17]-[24]) due to many outstanding characteristics such as very high speed, acceleration, torque and electric power density. With its very simple structure, the SRM is ideal to operate as starter to spin the main turbine and as a generator to supply electric power for the airplanes.

The first SRM for an integral starter/generator (IS/G) on aircraft engines was designed by MacMinn in 1989 [17]. The performance of the 30kW-SR S/G system was investigated by Ferreira, Jones, and Heglund in [20].

In order to increase power, a first detailed design of a 250 kW SR S/G system with 12/8 pole topology was presented by Ferreira and Richter in [22]. A two channel power inverter was discussed in [21], [23], and [24]. Two independent channels of the power inverter for one SRM can supply a total rating power of 250 kW continuous and 330 kW for 5s. Each channel of this system has its own power electronics which operates independently. Thus, the rated current of the power converters is reduced.

However, the torque performance criteria are still big challenges for high-speed reluctance machines. The Ph.D. thesis [71] introduced the optimal torque control strategy which was investigated in an analytical model. It had not yet been validated experimentally.

1.3 Motivation

Many research topics on the switched reluctance starter/generator systems for electric aircraft applications have been reported for several decades in [15]-[19]. But, the optimal control strategies of the SR S/G drive have not been implemented perfectly. Due to the non linearity in the magnetic characteristic of the SRM, it is very complicated to analyze the relationship between the torque, current and excitation angles. Nowadays, advanced technologies like magnetic material of high saturation flux density and power semiconductors with high switching frequency can be applied. The optimal control strategies are easier to be integrated by electronic circuits. Especially for this high speed and power density reluctance machine, the current and angle controllers are implemented in FPGA ICs by a CPLD program to improve real time control abilities. With the advanced measurement techniques, a data acquisition device has also been developed to verify and record the analog and digital signals.

The performance of the SR S/G system designed in [71] had been verified by the simulation results with PC-SRD software and those results indicate that the designed system is capable of meeting the requirements basically. The dynamic performance of system is investigated by an experimental setup. To deal with the maximum torque control proposal, some tasks have been identified as follows:

- An accurate simulation and measurement of the SRM magnetic characteristics can be obtained by a FEA model and experimental test.
- Precise iron loss calculation and measurement methods for the high speed and flux density of the SR S/G will be determined by an improved measurement technique. Afterwards, a thermal model is simulated to investigate the temperature distribution.
- Finally, the maximization of the average torque control method with an off-line optimization of the turn-on and turn-off angle and current controllers can be investigated by an indirect torque measurement method based on an additional moment of inertia serves as dynamic load. In motor mode, the load torque is created by the acceleration and the additional moment of inertia. In generator operation, the power is measured based on the deceleration of the speed. The SR S/G torque and power performance should be verified the performance requirement of the SR S/G drive system.

1.4 Outline of the Thesis

Chapter 1 presents an overview of the switched reluctance machines for more electrical aircraft applications.
Chapter 2 describes the magnetization curves calculated in a FEA model and validated by measurement. A dynamic SRM model has been simulated to investigate the performance of the SRM.
In chapter 3, estimation and measurement methods for losses and temperature distribution in the machine are described.
Chapter 4 deals with optimal turn-on and turn-off angles to maximize the average torque. The maximum torque control is validated by an indirect torque measurement method. A high speed SR S/G with an inertia load drive system has been built to measure the torque and power in motor and generator modes.
Chapter 5 presents the magnitude and spectrum of the SRM acoustic noise measurement at speeds up to 47,000 rpm and the noise frequency spectrum up to 20 kHz.
Chapter 6 gives a summary of the work and introduces a proposal of a back to back experimental set-up of SR S/G.

2 SRM Magnetic Characteristics

The electromagnetic torque and flux linkage curves play an important role on investigating the SRM performance. Those characteristics depend on some factors such as magnetic circuit, material properties and lamination shapes. Some publications about the measurement methods of the SRM magnetic curves have been presented in [29], [31], [34], [36] and [37]. However, they suffer from drawbacks concerning computation time, inductance saturation curves, and the influence of iron losses. With those methods, the effect of iron losses on dynamic flux estimation was only minimized by decreasing the frequency or applying a DC voltage. To overcome this limitation, an innovative measurement proposed addresses a way to remove overall iron losses.

In order to prove this measurement method, the experimental results are compared with Finite Element Analysis (FEA) simulation results and validated by a dynamic test as well. The resulting static torque and flux linkage curves will be used to simulate a SRM model at the end of this chapter.

2.1 Basic Operation Principle of the SRMs

A reluctance machine is an electric machine in which the rotor tends to move to a position where the windings are excited and the reluctance (magnetic resistance) is minimized [25]. The reluctance varies as the rotor teeth rotate in and out of alignment. The switched reluctance motor has saliencies on both rotor and stator, and the phase windings are wound on the stator teeth as depicted in fig 2.1. As long as a current I is flowing through the concentrated winding, tangential forces F_T affect the rotor teeth as depicted for rotor angles $0^o < \theta < 90^o$.

There are two important positions of SRM, the position with maximum inductance L_a is called aligned position, the minimum inductance L_u consequently occurs at the unaligned position. The angle τ between both positions will later be referred to as dwell angle. Since the inductance is inversely proportional to reluctance, the inductance of a phase winding achieves a maximum when the rotor is in aligned position and a minimum when the rotor is in unaligned position. The inductance varies with rotor position as shown in fig 2.3.

The switched reluctance machines are often analyzed assuming linear operation without magnetic saturation in the iron lamination. This greatly simplifies the mathematical machine model, then the magnetic characteristic can be considered as an only function of rotor position.

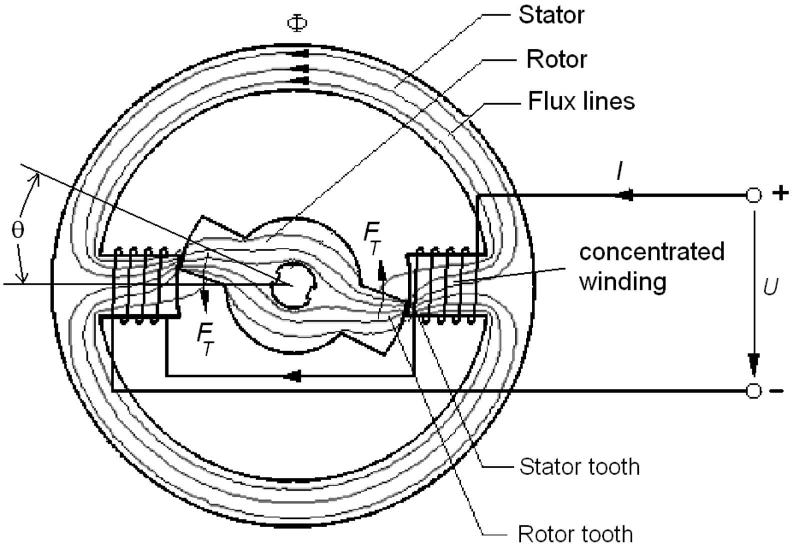

Figure 2.1: Simple principle of reluctance machine operation [46]

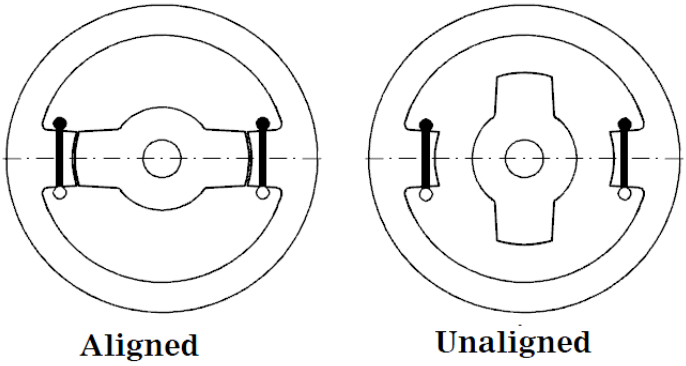

Figure 2.2: Aligned and unaligned positions of an SRM [25]

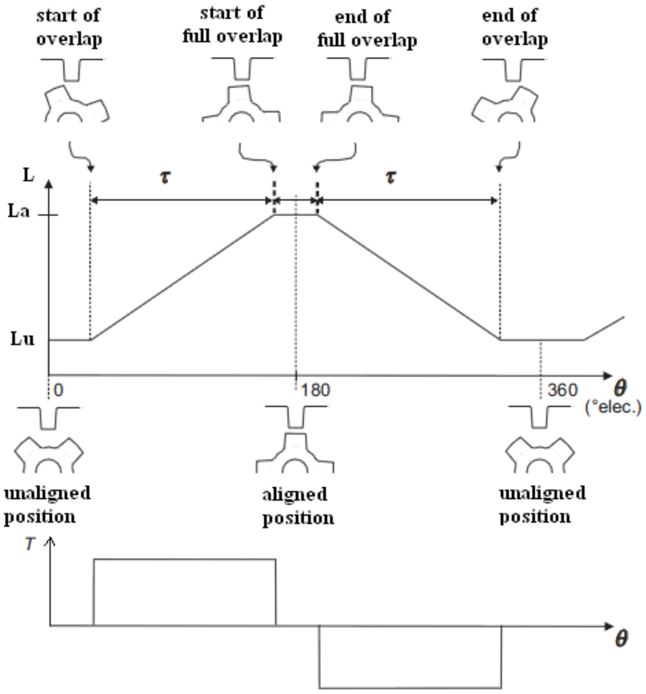

Figure 2.3: Variation of inductance and torque with rotor position

SRM Topologies

There are many possible combinations of numbers of stator and rotor teeth each having its advantages and disadvantages. Possible numbers may be fixed e. g. according to the theory of fractional slot windings or to [26]. Popular types are e.g. 6/4, 8/6 and 12/8 as shown in fig 2.4. E. g. a 6/4 SRM has 6 stator teeth and 4 rotor teeth with the number of phases N_{ph} = 3. SRMs with higher numbers of phases are able to generate almost constant torque and reduce the torque ripple, but the IGBT switching frequency is higher, because the electric frequency equals the number of rotor teeth multiplied by the mechanical frequency. For this application, a three phase 6/4 SRM was selected in [71].

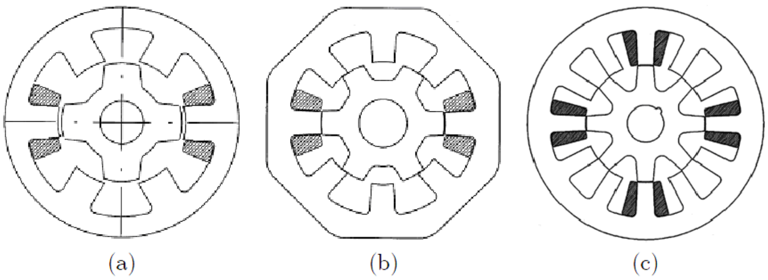
(a) (b) (c)

Figure 2.4: Popular topologies of SRM applications: 6/4 (a), 8/6 (b) and 12/8 (c) [25]

Power Inverter Topology of the SR S/G

There are various inverter topologies for the phase coils. However, the most common one is the asymmetric half bridge because it offers a great deal of flexibility, e.g. the possibility to apply positive and negative DC link voltage to the phase as well as zero voltage (freewheeling). The three phase-asymmetric half-bridge inverter is shown in fig 2.5.

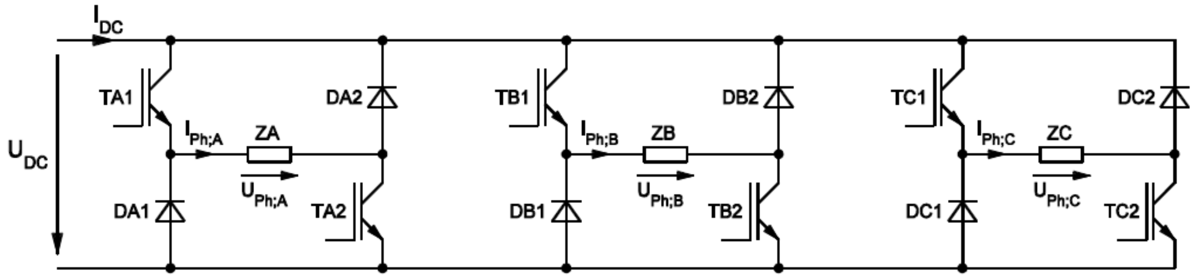

Figure 2.5: Three phase asymmetric half bridge inverter [46]

2.2 Analytical Method of the Magnetization Characteristics

2.2.1 Mathematical Equations

The mathematical model of the SRM operation principle obeys the laws of physics. The electromagnetic torque is produced by the change of the magnetic co-energy W_{Co} due to changes in current i(t), rotor position θ(t), and inductance L(θ) with W_{co}=f(i(t),θ(t),L(θ)) according to (2.1).

$$T = \frac{\partial}{\partial \theta} \cdot W_{co} \tag{2.1}$$

This torque draws the rotor to the aligned position. Based on this principle, a reluctance motor may be modeled differently from other types of electric machines.

Flux Linkage and Inductance

Mathematical equations of voltage, flux linkage and inductance have been introduced in [25]. When a single phase is exited, the voltage equation for one phase is as follow (2.2)

$$\begin{aligned} u &= R \cdot i + \frac{d\Psi}{dt} = R \cdot i + \frac{dL(\theta(t)) \cdot i(t)}{dt} \\ &= R \cdot i + L \cdot \frac{di}{dt} + i(t) \cdot \frac{\partial L}{\partial \theta} \cdot \frac{\partial \theta}{dt} \\ &= R \cdot i + L \cdot \frac{di}{dt} + \omega \cdot i \cdot \frac{\partial L}{\partial \theta} \end{aligned} \tag{2.2}$$

where u is the terminal voltage, i is the current, Ψ is the flux linkage, R is the phase resistance, L is the phase inductance, θ is the rotor position, and ω is the angular velocity. The last term is sometimes interpreted as a back emf.

Torque Production

From the voltage equation (2.2), the instantaneous electrical power p results in (2.3):

$$p_{electrical} = R \cdot i^2 + L \cdot i \cdot \frac{di}{dt} + \omega \cdot i^2 \cdot \frac{dL}{d\theta} \tag{2.3}$$

Respecting the power loss in the ohmic stator resistance

$$p_{loss} = R \cdot i^2 \tag{2.4}$$

and the rate of change of the magnetically stored energy

$$\begin{aligned} \frac{dW_{mag}}{dt} = \frac{d}{dt}\left(\frac{1}{2} \cdot L \cdot i^2\right) &= \frac{1}{2} \cdot i^2 \cdot \frac{dL}{dt} + L \cdot i \cdot \frac{di}{dt} \\ &= \frac{1}{2} \cdot \omega \cdot i^2 \cdot \frac{\partial L}{\partial \theta} + L \cdot i \cdot \frac{di}{dt} \end{aligned} \tag{2.5}$$

according to the law of conservation of energy, the instantaneous mechanical power is:

$$p_{mechanical} = p_{electrical} - p_{loss} - \frac{dW_{mag}}{dt} = \frac{1}{2} \cdot \omega \cdot i^2 \cdot \frac{\partial L}{\partial \theta} \tag{2.6}$$

The time integral of (2.6) delivers the magnetic co-energy W_{co} during a change of angle from $\theta(t_1)$ to $\theta(t_2)$:

$$W_{co} = \int\limits_{t_1}^{t_2} \frac{1}{2} \cdot \omega \cdot i^2 \cdot \frac{\partial L}{dt} = \int\limits_{L(\theta(t_1))}^{L(\theta(t_2))} \frac{1}{2} \cdot i^2 \cdot \ dL = \int\limits_{\Psi(\theta(t_1))}^{\Psi(\theta(t_2))} \frac{1}{2} \cdot i \cdot \ d\Psi \tag{2.7}$$

The torque in case of a constant current now follows as angular derivation of (2.7):

$$T = \frac{\underset{\cdot}{\mathrm{W}}_{co}}{d\theta} = \frac{1}{2} \cdot i^2 \cdot \frac{\partial L}{\partial \theta}|_{i=const} \tag{2.8}$$

In nonlinear model, the average torque is based on the enclosed area W_{co} in the energy conversion diagram in fig 2.6.

Fig 2.6 shows the measurable or calculable flux linkage vs. current curves. The flux linkage is plotted in unaligned (0-U) and aligned (0-A) position. The co-energy and thus the torque is proportional to the area between both curves.

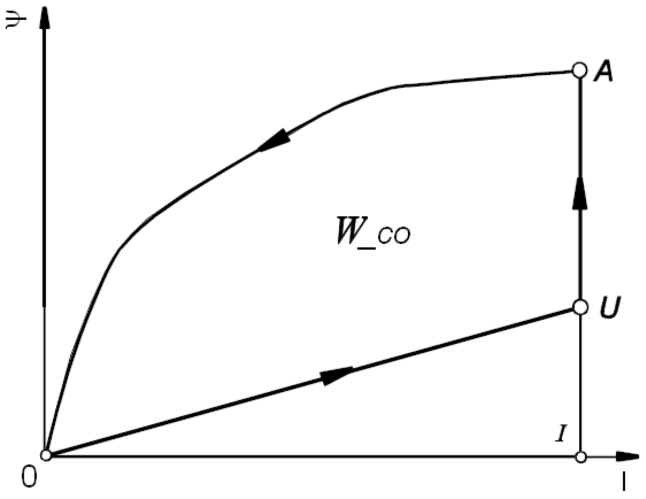

Figure 2.6: Flux linkage Ψ vs. current I curves [25]

2.2.2 Analytical Calculation

Fig 2.7 shows the cross section of both rotor and stator lamination shapes. Based on this CAD drawing, the non magnetic properties can be determined in the air gap, copper windings. The silicon steel parameters were accessed to the rotor and stator areas. The B/H magnetic curves and the SRM dimensions are basic inputs for an analytical calculation.

The material properties, i. e. the magnetization and iron loss density curves of the used silicon steel M270-35A, are given in figs 2.8 and 2.9. Those parameters will be used to calculate magnetic curves and simulate the SRM model.

However, the data sheets from manufacturers are not sufficient for the calculation of the magnetic circuit due to a high saturation level of flux densities both in stator and rotor teeth exceeding the maximum values of the manufacturers' datasheets [32], [33]. The core loss densities are only valid for sinusoidal voltage and current waveforms.

Flux Linkage and Inductance Calculation

For analytical calculation, homogeneous field lines are assumed in all different parts of the magnetic circuit. With respect to the length and the field strengths in the rotor, the stator and the air gap, Ampere's circuital law is written as:

$$N_t \cdot i = \Sigma_{i=1}^{N} H_i \cdot l_i = 2(H_{ST} \cdot l_{ST} + H_{RT} \cdot l_{RT} + H_g \cdot g) + H_{SY} \cdot l_{SY} + H_{RY} \cdot l_{RY} \tag{2.9}$$

Where,

H_{ST},H_{RT},H_{SY},H_{RY},H_g	magnetic field of stator, rotor teeth, stator, rotor yoke, air gap
l_{ST},l_{RT},l_{SY},l_{SY}, g	lengths of stator, rotor teeth, stator, rotor yoke, air gap

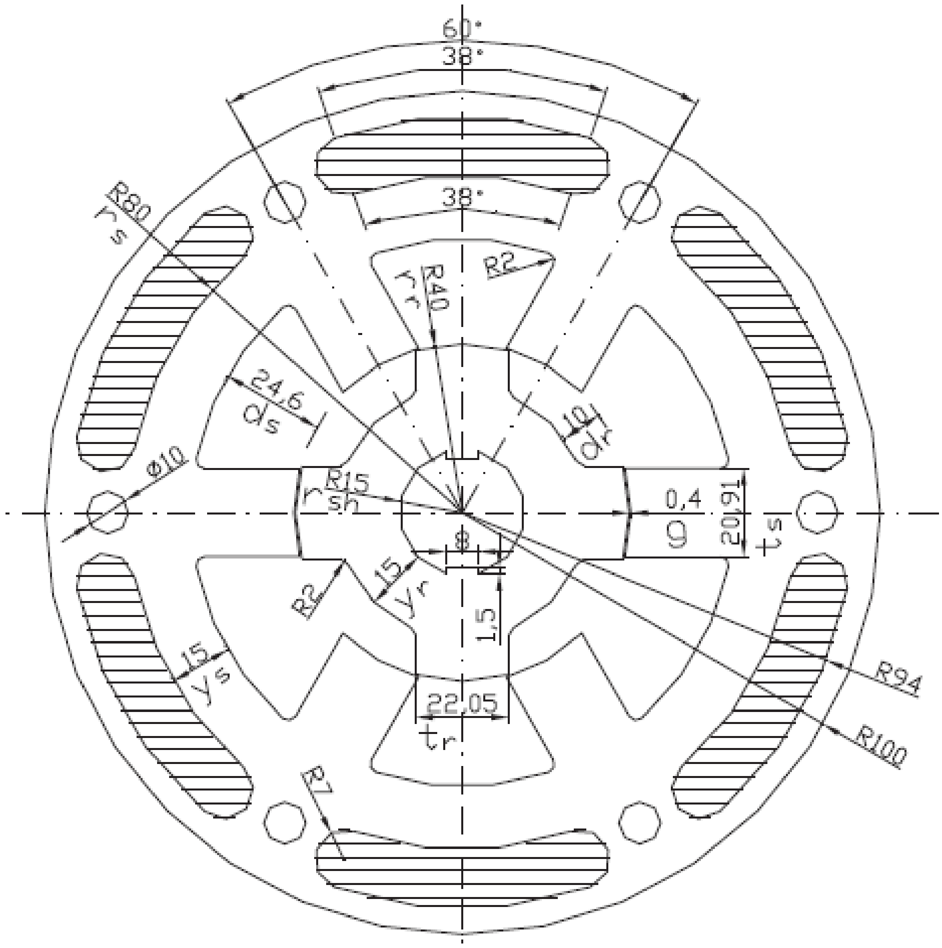

Figure 2.7: Cross section of machine electromagnetic topology [71]

The flux densities are determined by the cross sectional area of every part according to (2.10).

$$\Phi = B_{ST} \cdot A_{ST} = B_{RT} \cdot A_{RT} = B_{SY} \cdot A_{SY} = B_{RY} \cdot A_{RY} = B_g \cdot A_g \tag{2.10}$$

The magnetic flux can be determined from (2.9) and (2.10) by iteration or a graphical solution based on the magnetization curves of fig 2.8. In case of unaligned position, the leakage must be estimated by flux line approximation. With respect to the number of turns N_t, the inductance of the coil results as:

$$L = \frac{N_t \cdot \Phi}{i} \tag{2.11}$$

Electromagnetic Torque Prediction

The electromagnetic torque depends on the phase current and rotor position. It can be calculated from the co-energy W_{co} according to (2.8): From the energy loop in fig 2.10, the co-energy while passing from unaligned to aligned position at constant current I is proportional to the area enclosed by the arrow lines (0UA).

Since the curve in the aligned position is highly saturated, the integration needs a stepwise

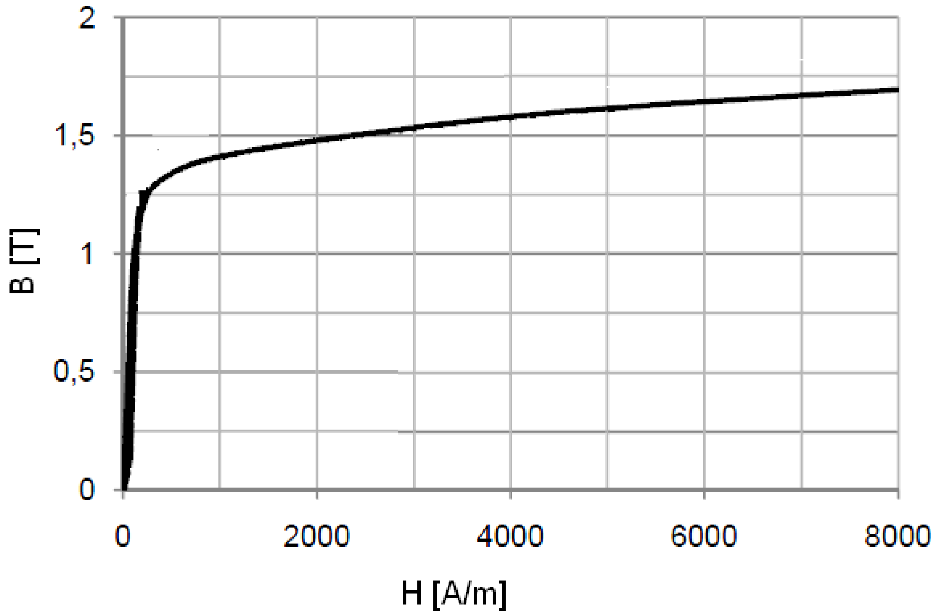

Figure 2.8: Magnetization curve of M270-35A material at 50 Hz[46]

numerical calculation. The unaligned curve being almost a straight line may be approximated by using only start and end values.

For the unsaturated case, the edge effects and for a rotor position between unaligned and aligned positions are neglected. This leads to:

$$T = \frac{1}{2} \cdot I^2 \cdot \frac{dL(\theta)}{d(\theta)} = \frac{1}{2} \cdot I^2 \cdot \frac{L_a - L_u}{\tau} \tag{2.12}$$

with τ being the dwell angle between aligned and unaligned position as depicted in fig 2.3. The electromagnetic torque strongly depends on the difference between the phase inductances L_a and L_u. The ratio L_a/L_u has to be maximized to achieve as much torque per ampere as possible. Therefore, switched reluctance machines are built with a doubly salient structure and the air gap must be kept rather small.

2.3 2D FEA Model

Many approaches have been described in order to investigate the magnetic curves of the SRM by finite element analysis (FEA) [31], [36], and [54]. This method calculates the magnetic field in small special units called meshes. This it is based on the shapes and material properties of stator and rotor laminations. E. g. flux linkage, inductance, and electromagnetic torque values are output results of the FEA model.

Here, these values were calculated for different phase currents and positions. The results were used to build up lookup tables which will be used for torque control afterwards. An example for the flux density distribution is shown in fig 2.11.

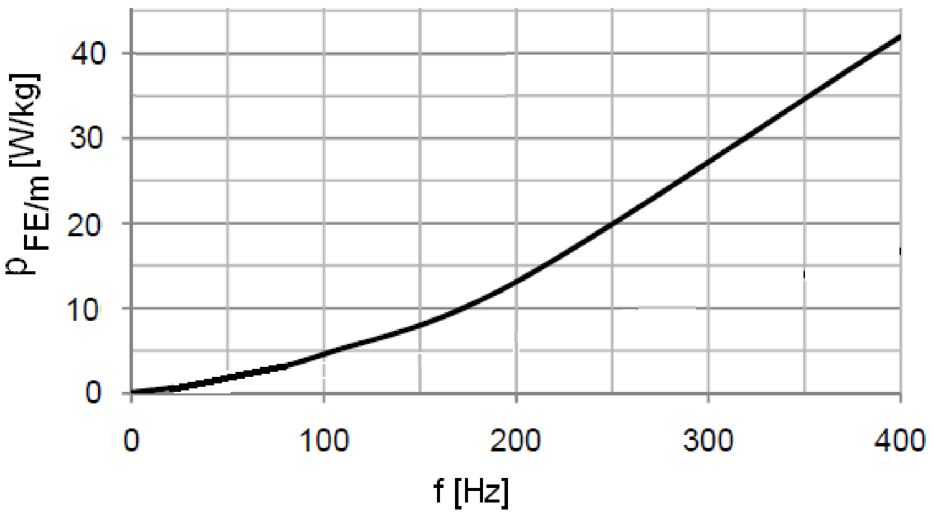

Figure 2.9: Iron loss density of M270-35A material at 1.5 T [46]

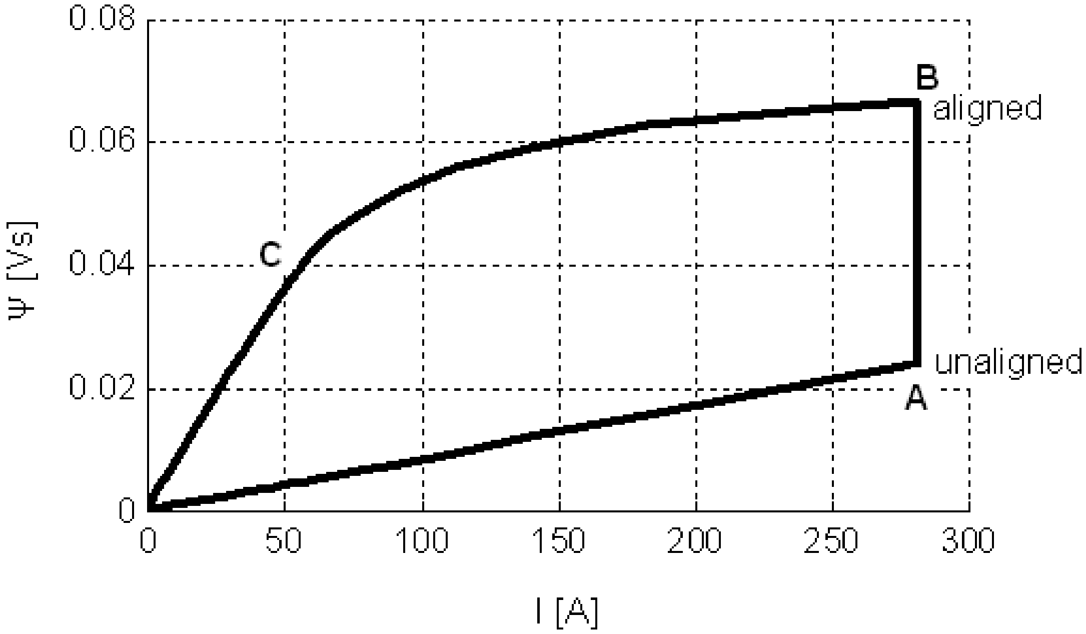

Figure 2.10: The co-energy loop W_{co} (OABCO) with OC is linear flux-linkage area and CB is non-linear flux-linkage area

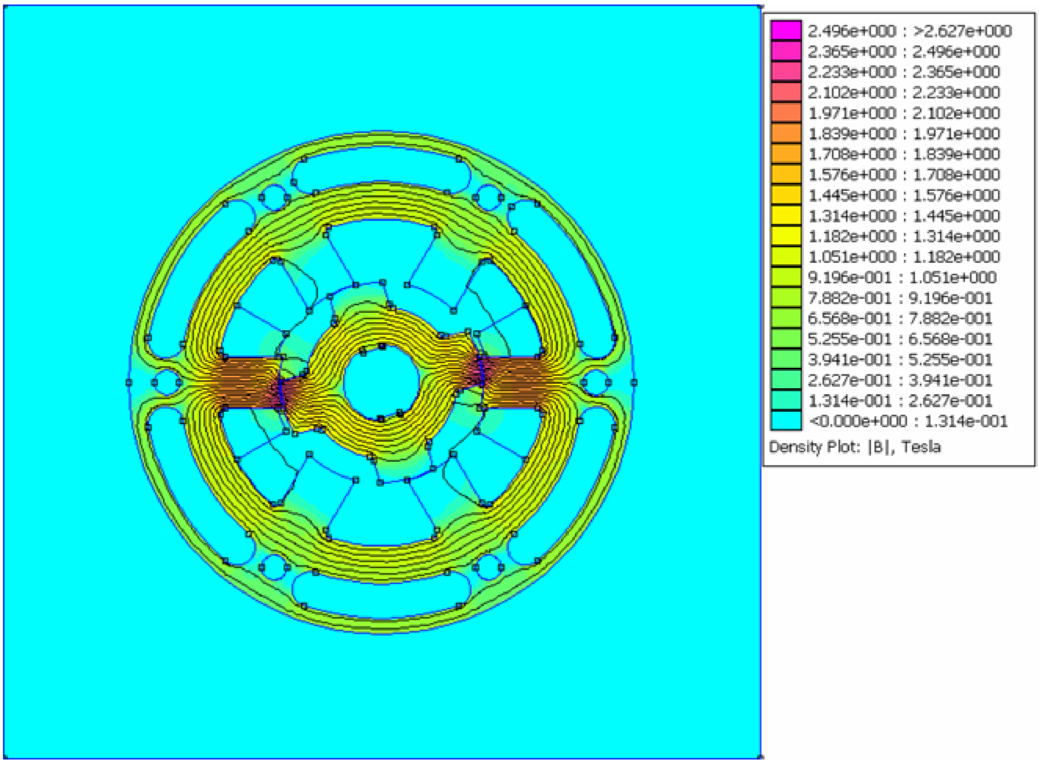

Figure 2.11: Flux density at 15^o rotor position

Basically, it is possible to use 2D or 3D simulation methods. Because of the cylindrical symmetry of both stator and rotor, a 2D FEA model was selected to analyze the magnetic field.

The magnetic field can be calculated by solving the following differential equation (2.13) numerically:

$$\nabla \cdot (\frac{1}{\mu(B)} \nabla \cdot A) = -\sigma \cdot \dot{A} + j \tag{2.13}$$

where j represents the current density sources. A is the magnetic vector potential.
The flux linkage and electromagnetic torque curves are shown in figs. 2.12 and 2.13 respectively. The magnetic force density follows from the local field magnitude as gradient of Maxwell's stress tensor and the gradient of the permeability:

$$\vec{f} = \nabla \cdot T_m - \frac{\vec{H}^2}{2} \cdot \nabla \cdot \mu \tag{2.14}$$

In order to set the second term zero and nevertheless calculate the total force, a volume integral of the stress tensor covering the complete rotor is used to determine the torque. The mesh element size can be specified by the air gap and mechanical dimensions. Since the air gap is only 0.4 m, the mesh size has been selected 0.1 mm. The load is given by the phase currents. The phase currents were varied from 20 to 300 A with steps of 20 A.

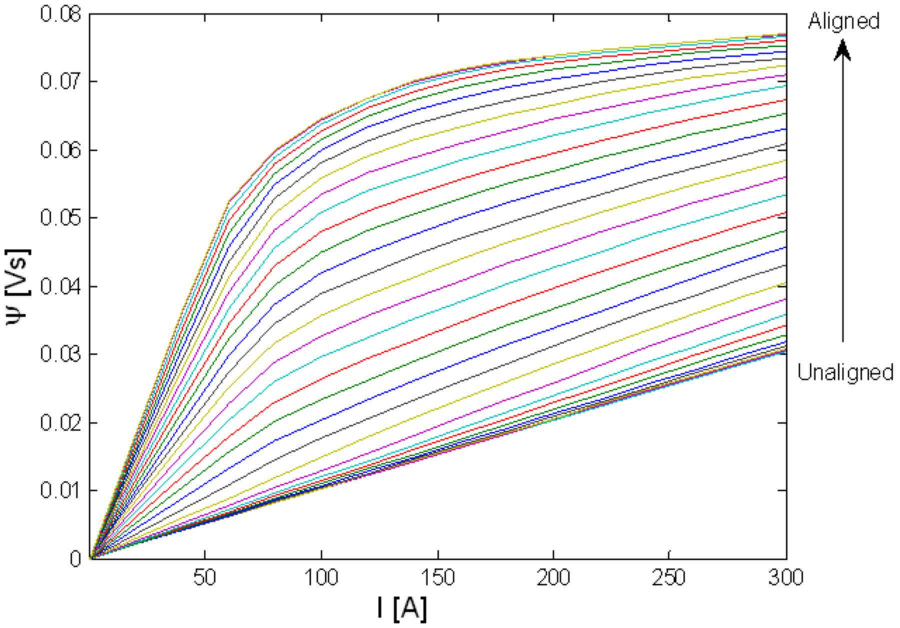

Figure 2.12: Flux linkage curves (1^o angular steps)

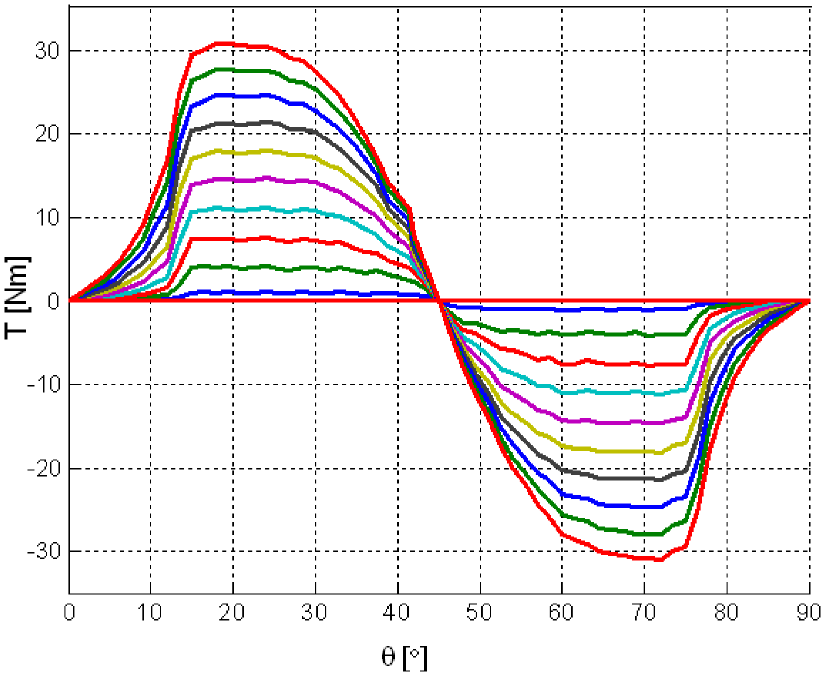

Figure 2.13: Static torque curves (aligned: 0^o, unaligned 45^o, 30 A current steps from 30 to 300 A), determined by FEA

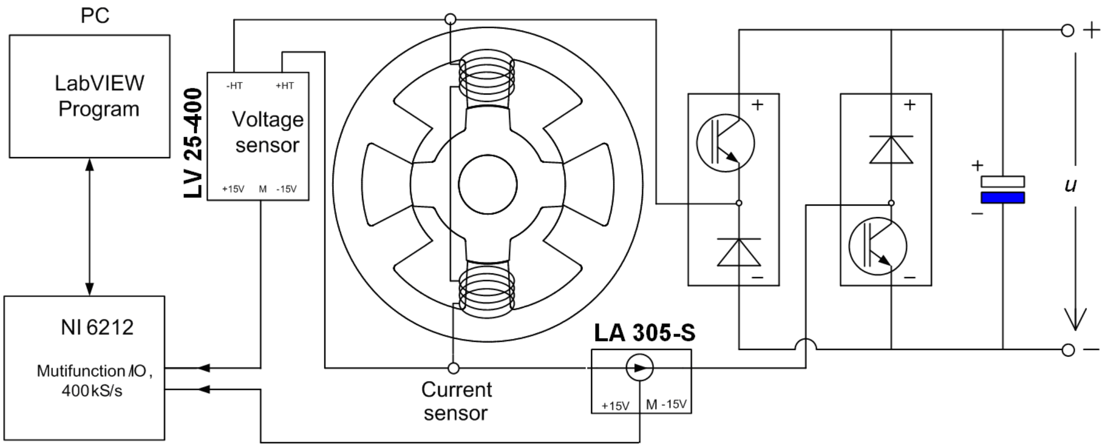

Figure 2.14: Experimental setup for flux curve determination

In large areas like yoke or teeth, the length of a mesh may achieve about a tenth of the total dimension. This calculation was done for rotor angles from 0^o to 90^o with steps of 1^o resulting in totally 15x90 = 1350 field distributions. At the end of each calculation, torque and flux linkage values were stored for the lookup tables. The execution of the calculation series was controlled by a program in Lua language.

2.4 Measurement Method For the Flux Linkage Curves

An accurate measurement method of the magnetic characteristics was carried out to investigate the SRM magnetic characteristics in [29]. Some authors described indirect and direct measurement methods with switched DC or AC voltage supplies [28], [34] and [37].
Based on voltage and current measurement, the magnetization characteristics can only be exactly determined when the iron losses are removed. The method proposed below has many advantages such as: no external resistor, no searching coil, and no offsets. The flux-linkage and inductance are directly calculated from measured magnitudes by a LabVIEW program[1]. Test objective of this measurement is a SRM from fig 2.7 which was designed for a maximum phase current 300 A. The copper resistance and the winding temperature were measured before testing. Voltage and current waveforms were recorded by a data acquisition system (DAQ) NI-USB6212 [97] using a LabVIEW program. The NI-USB 6212 is a bus-powered multifunction acquisition device for USB 16 bits, 400 kS/s, 16 analog inputs and 2 analog outputs. Two analog inputs were used for measuring the voltage and current waveforms of one phase. The voltage transducer LV 25-400 [99] (400 ± 3.2 V) and current transducer LA 305-S [98] (300 ± 2.4 A) were applied for this experimental setup as fig 2.14.

2.4.1 Experimental Setup

Since flux linkage and torque curves depend on the rotor position, this position was locked by using an indexing head allowing to define the angle within 1^o intervals. From the measured current and voltage values, the flux linkage follows as:

$$\Psi(t) = \int_{0}^{t} (u - R \cdot i)dt + \Psi(0) \tag{2.15}$$

with

u	terminal voltage across phase winding
R	resistance of the phase winding
i	phase current
$\Psi(0)$	remanent flux linkage at zero current
t	time to achieve steady state, i. e. i = u/R keeps constant

2.4.2 Analysis of Experimental Results

In order to eliminate the iron loss in this measurement method, the voltage and current waveforms have been recorded during rising, falling and saturation current periods. An induced voltage is positive when the IGBT is switched on, negative while the IGBT is switched off and zero in saturation state. The voltage, current and flux linkage curves were measured and calculated directly by LabVIEW software.

Before applying a DC voltage to one phase winding, the voltage, current and flux linkage values are zero. This ensures that the offsets were removed. From those waveforms in fig 2.15, it is very easy to notice three different regions. Energizing is the region in which the flux increases from zero to saturation and the induced voltage falls from terminal voltage to zero. During the saturation period, the current curve is almost flat, the induced voltage approaches zero. In the de-energizing region, the current and inductive voltage decrease simultaneously and then approach zero.

For the following experiments, a voltage source with a weak behavior was chosen in order to limit the current by hardware, which results in a source voltage dropping down at high current values. The voltage source was switched on for a sufficient period in order to achieve steady state and then switched off again (fig 2.15). 2,000 values were sampled with 50 kS/s for each measurement.

Fast changes in the voltage will cause eddy currents in the core, which will dominate the hysteresis losses for high frequencies. In order to eliminate these losses, the voltage and current waveforms have been divided up into energizing, saturation, and de-energizing periods (fig 2.15). The respective periods are characterized by:

di/dt $>$ 0 resp. $u_i > 0$: energizing (index e)
di/dt $=$ 0 resp. $u_i = 0$: saturation (index s)
di/dt $<$ 0 resp. $u_i < 0$: de-energizing (index d)

---

[1] is a program used to control and measure electrical parameters of the drive system

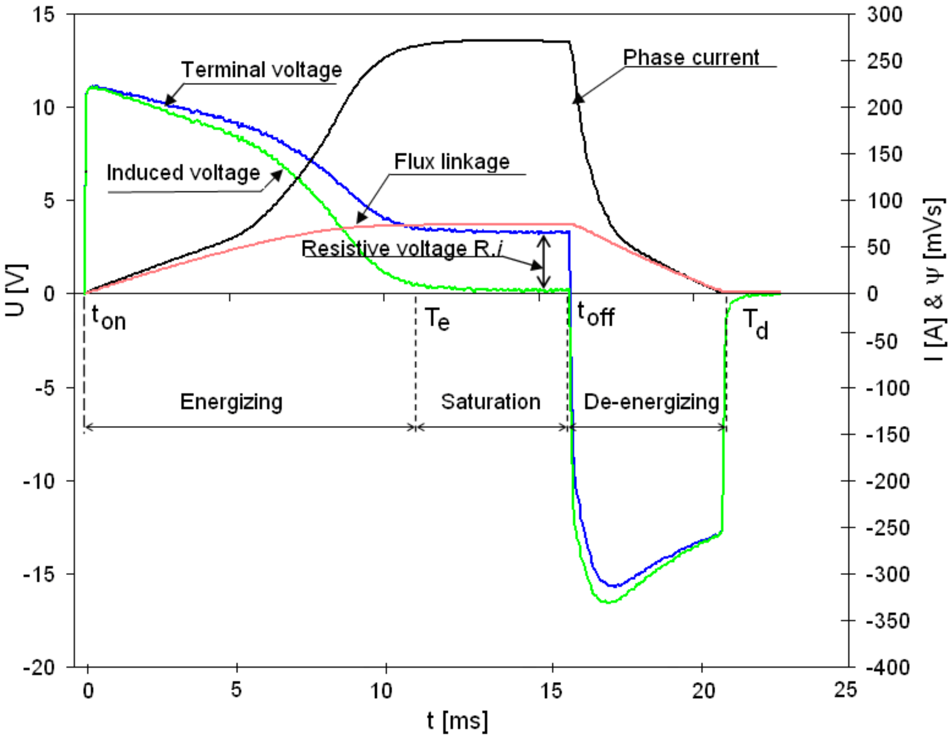

Figure 2.15: phase current i; terminal voltage u; induced voltage u_i

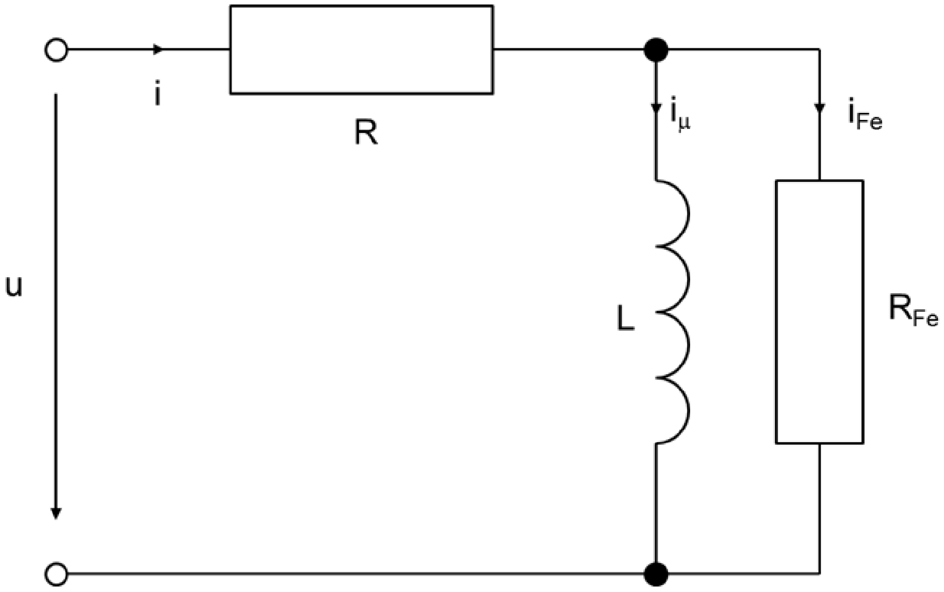

Figure 2.16: Model for eliminating the iron losses

The iron losses are modeled as an ohmic resistance parallel to the inductance (fig 2.16) according to the assumption that eddy current losses dominate.
The flux linkage achieved until settling may be calculated as:

$$\Psi_e = \Psi(t_{on}) + \int_{t_{on}}^{t_{on}+T_e} (u - R \cdot (i_\mu + i_{Fe}))dt = \Psi(i_\mu) - \Psi_{loss} \tag{2.16}$$

with $\Psi_{loss} = \int_{t_{on}}^{t_{on}+T_e} (R \cdot i_{Fe})dt$ and $\Psi(t_{on}) = 0$.
After switching off (u $<$ 0), the voltage across the inductance will change its sign causing a change of the sign of i_{Fe}, too:

$$\Psi_d = \int_{t_{off}}^{t_{off}+T_d} (u - R \cdot (i_\mu - i_{Fe}))\, dt = \Psi(i_\mu) + \Psi_{loss} \tag{2.17}$$

with T_e and T_d are the time for energizing and de-energizing.
From the equations above follows the flux linkage for a given magnetizing current $\Psi(i_\mu)$ as average of Ψ_e and Ψ_d (2.18):

$$\Psi(i_\mu) = \frac{\Psi_e + \Psi_d}{2} \tag{2.18}$$

Fig 2.17 depicts the total flux linkage values vs. energizing and de-energizing currents. Half of the current difference of both curves at constant flux linkage delivers the iron current i_{Fe}. Fig 2.18 summarizes the corrected flux linkage characteristics determined by measurement.

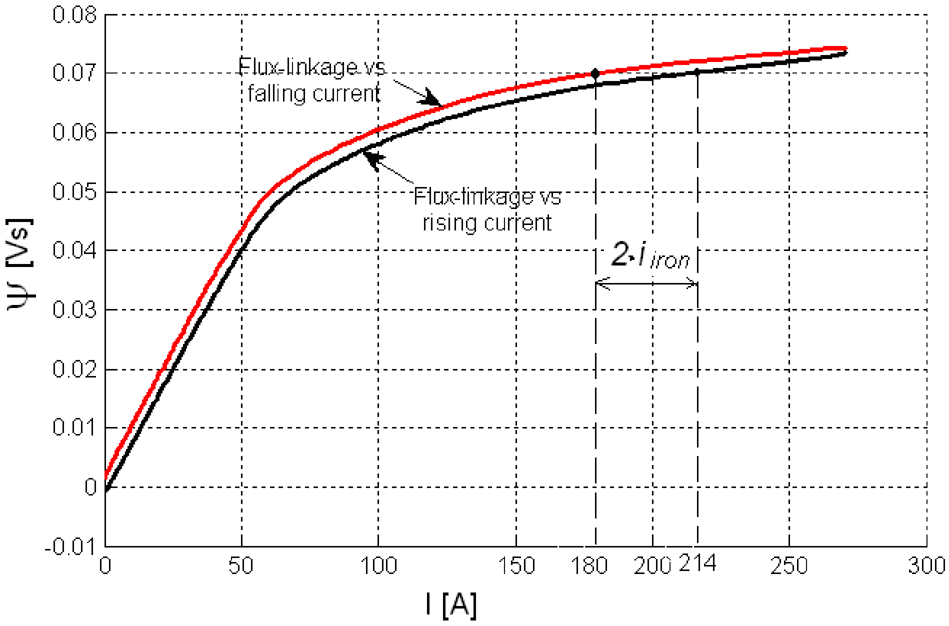

Figure 2.17: Flux linkage curves in rising and falling currents

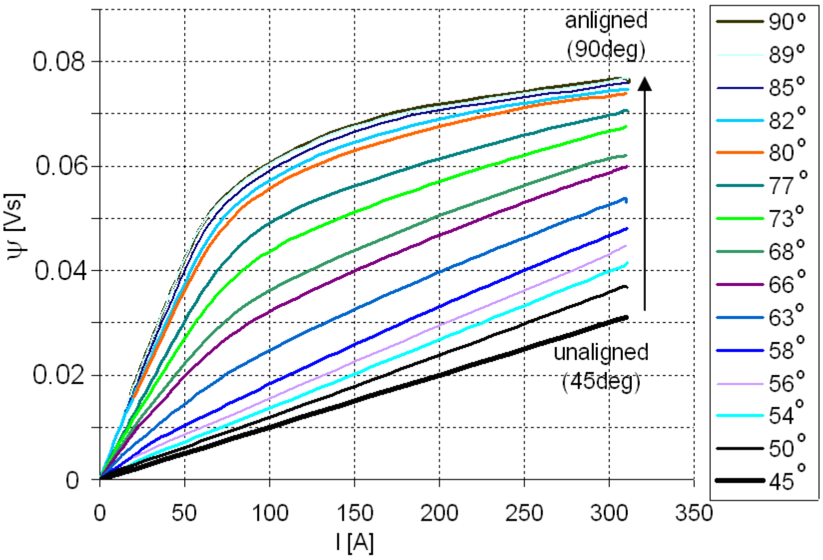

Figure 2.18: Experimental flux linkage results

Comparison of Simulation and Experiment Results

Fig 2.19 shows some examples for both FEA and experimentally determined flux linkage curves. In unaligned position, the experimental flux values are slightly higher than the simulated ones (up to +9 %), whereas in aligned position the opposite behavior is observed (up to 6 %). Reasons may be found in non-modeled mechanical tolerances as well as in inaccuracies in the magnetization curve. The main reasons for those differences are the manufacturing and mechanical tolerances mainly in the air gap. The air gap required is only 0.4 mm. The mechanical tolerances come from constructing the rotor and the bearing into the SRM housing.

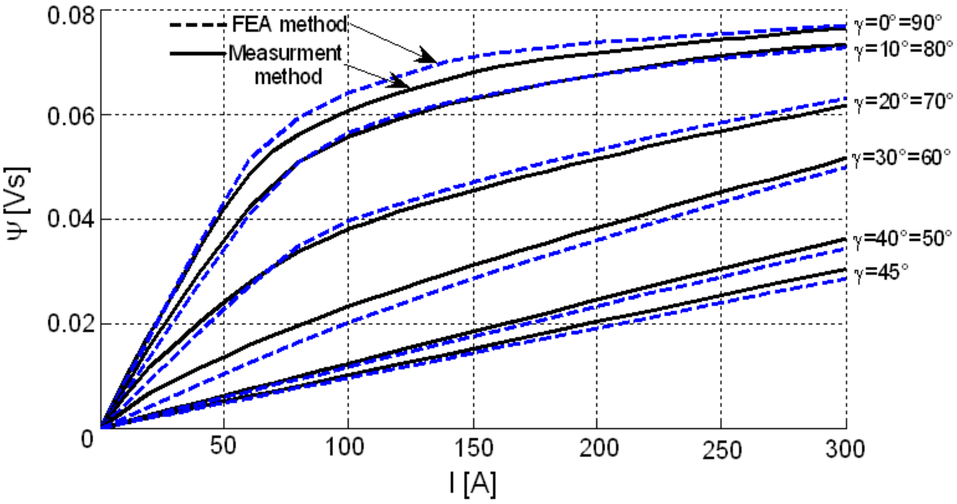

Figure 2.19: The experiment and FEA result comparison

Table 2.1: Comparison between measurement and FEA results

Position	I [A]	FEA [mVs]	Measurement [mVs]	Difference [%]
Aligned	100	64.3	60.5	5.9
	200	75.7	73.5	2.9
	300	77.4	75.9	1.9
Unaligned	100	9.8	10.7	8.3
	200	19.6	21.4	8.78
	300	29.4	32	8.46

2.5 Electromagnetic Torque Measurement

For this experiment, a torque transducer was mounted between rotor shaft and indexing head as shown in fig 2.20. The torque transducer is a torque sensor (DL2000-VA-TE-T, 100Nm [100]) which is reliable to measure static torque. The torque transducer was coupled to a torque analyser (MD 6000 [100]). The accuracy (0.2 % of full scale) is ± 0.2 Nm.

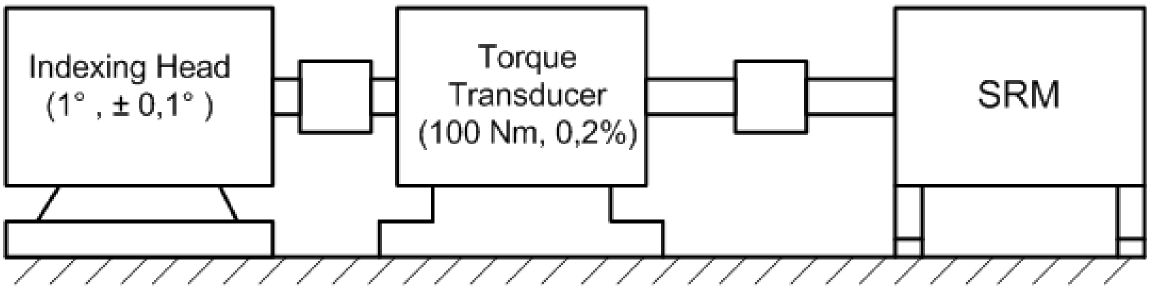

Figure 2.20: The mechanical locking system of the rotor

When a DC current was applied to the phase windings, a torque value was obtained from the torque sensor. The phase current was kept constant by chopping current control with a small hysteresis current. The static torque curves were determined from 0^o to 90^o of rotor angle with a step of 3^o. To reset the rotor at full aligned position, a DC current of 20A is excited to one phase and then the rotor is coupled with the indexing head. The step angle can be changed by the indexing head easily in fig 2.20.

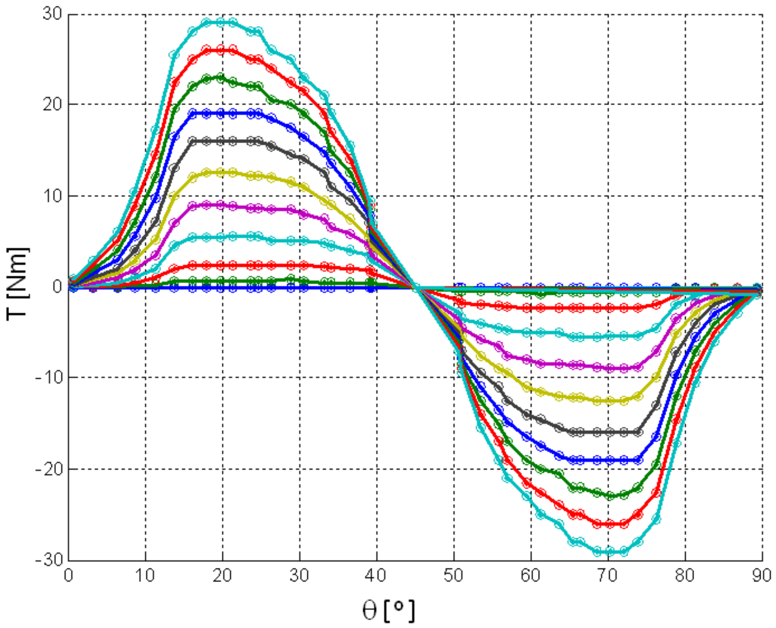

Figure 2.21: Static torque measurement

The measured result is compared to PC-SRD and FEA results in table 2.2. The FEA, PC-SRD, and measurement results agree well. Those results were investigated in three basic rotor positions of switch on (15^o), conduction (22.5^o) and switch off (30^o) angles for static operation. The differences between simulated and measured results may be explained by some small offsets of torque sensor signals and rotor position angles.

Table 2.2: Torque comparison between FEA, PC-SRD and Measurement results

Current	θ [^{o}]	FEA [Nm]	Mea [Nm]	PC-SRD [Nm]
300	15	29.5	28.5	28.9
	22.5	31.2	29.5	31.2
	30	28.2	27.3	28.1
150	15	10.2	10.5	10.4
	22.5	12.8	13.5	13.2
	30	11.3	11.8	11.5

2.6 The SR S/G Drive System Model

2.6.1 Operation Principle of the SR S/G Drive System

To operate this drive system, the SR S/G is connected to some functional boards to control and feedback the parameters. A physical model of the SR S/G drive system is depicted in fig 2.22. The operation principle is described below:

Firstly, a R/D board converts the rotor position from a resolver to 12 digital bits. Based on those bits, the rotor position angle and speed are digitalized. Secondly, the actual rotor angle is compared with the turn-on and turn-off angles in the current controller. The phase currents are compared with low and high current levels (I_{low},I_{high}). Both rotor angle and phase current comparisons will decide switching signals for IGBTs in the power inverter. The reference current, turn-on and turn-off angles can be transmitted by the NI-USB-6212 from a labVIEW program.

2.6.2 Modeling of the SR S/G Drive System

In order to investigate the prospective dynamic performance, the physical model of SR S/G drive system was simulated in MATLAB/Simulink and the functional boards are characterized exactly. The main blocks are LabVIEW, NI-USB-6212, Current controller, Inverter and SRM shown in fig 2.23. The block functions are described as follow:

R/D Board

A resolver was used to feed back speed and rotor position. In stator, there are two windings (sin/cos windings). From the amplitude and phase of the sin/cos voltages can be concluded to the position of the rotor of the resolver. In the R/D board, analog signals of the sin/cos voltages are converted to 8 digital bits (DB9-DB2) of the rotor position. The frequency of the DB9 was used to measure the speed.

LabVIEW

Based on the requirement of the torque and speed, the reference values of the current, turn-on and turn-off angle can be determined by algorithm program in LabVIEW software. Those values will be transmitted to the hardware.

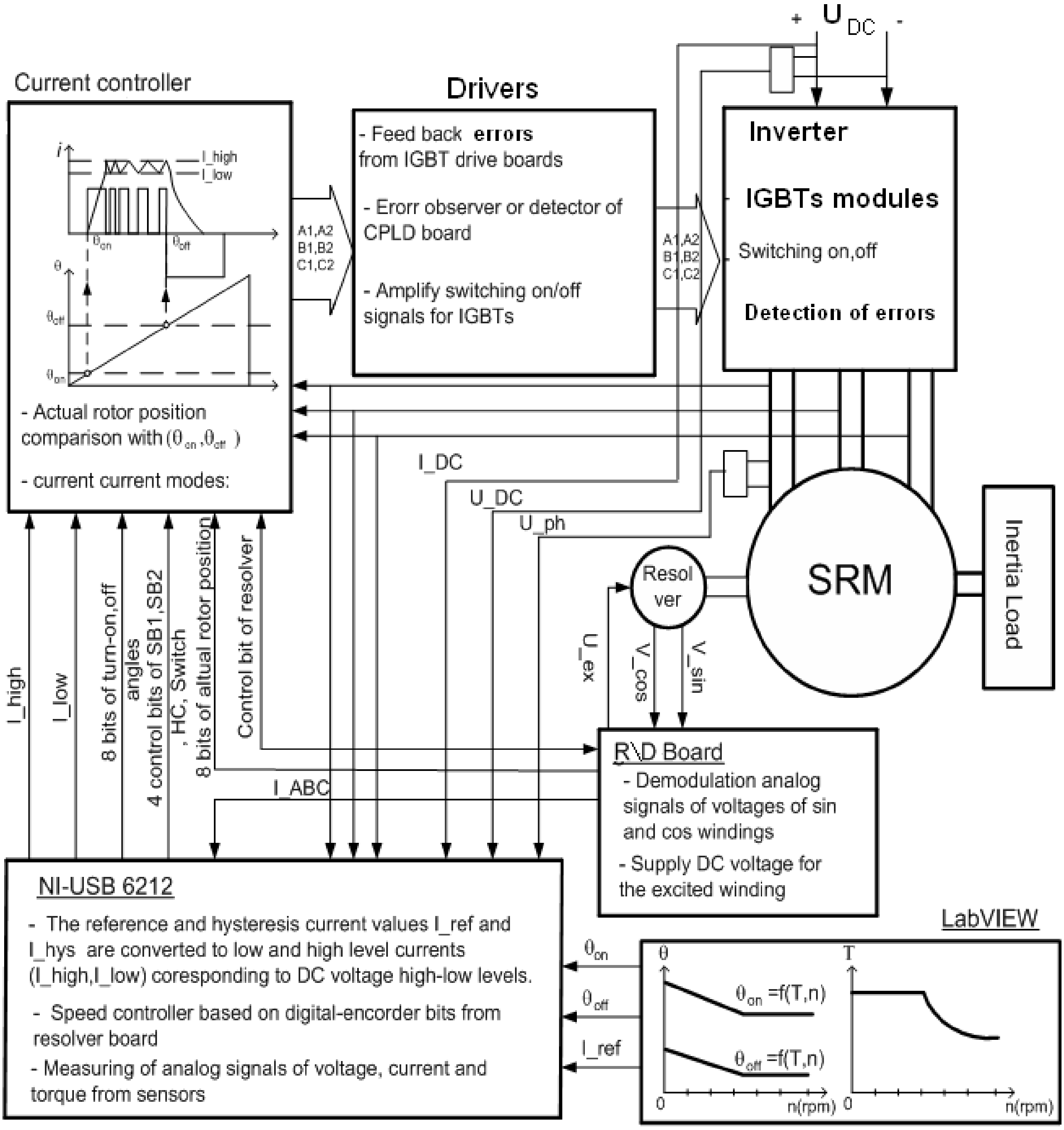

Figure 2.22: Operation diagram of the SR S/G drive system

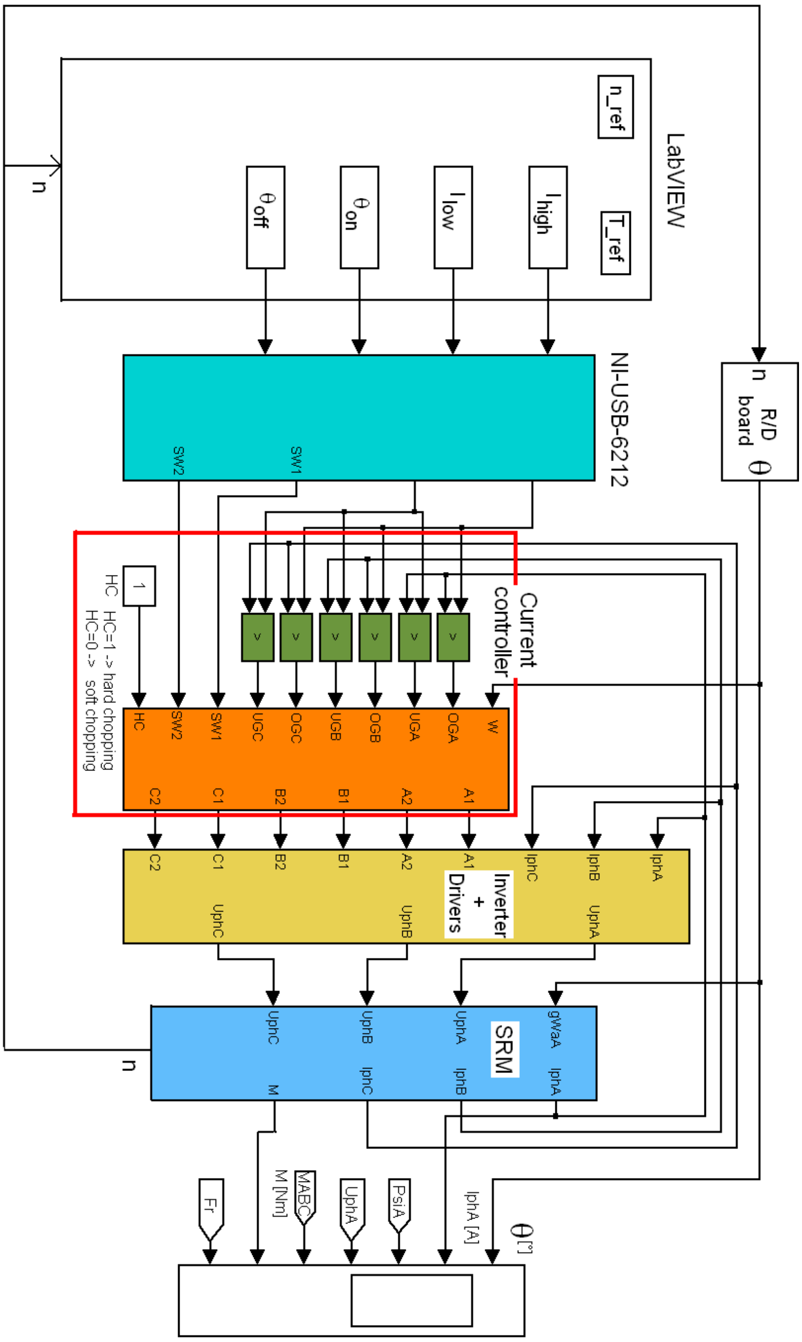

Figure 2.23: The SR S/G drive system model in Matlab/Simulink

NI-USB-6212

The data acquisition device (NI-USB-6212) and PC converter the reference current I_{ref} and hysteresis current I_{hys} values into two analog signals (I_{low} and I_{high}) and the turn-on and turn-off angles into 8 digital bits (SW1 and SW2).

Current controller

The phase currents are regulated in chopping mode by this current controller. The feedbacks of phase currents are compared to the (I_{low} and I_{high}) and the digitalized rotor angle W in 8 digital bits (DB2-DB9) is compared to (SW1 and SW2). Based on this comparison, six output signals (A1, A2, B1, B2, C1, C2) switch the IGBTs on or off

Inverter

There are six IGBT modules (SEMiX603GB066HDs) including the drivers for a three phase power inverter. The inverter supplies the switched voltage for the phase windings with a high frequency.

SRM

The non-linear SRM simulation was built based on the look-up tables of the current $i(\Psi,\theta)$ and the torque $T(\theta,\mathrm{i})$ by Simulink/Matlab. The current $i(\Psi,\theta)$ was inverted from the flux linkage curves $\Psi(\mathrm{i},\theta)$ which have been determined above. Fig 2.24 shows three phase of the SRM model. The outputs are the waveforms of phase current, voltage and torque. The rotor position from the resolver was simulated in this block.

2.6.3 Verification of the SRM Simulation

The SRM parameters for the dynamic time domain simulation, which have not yet been mentioned, are listed in table 2.3. Other parameters of the phase current, turn-on and turn-off angles depend on the torque and speed references.

The simulated waveforms of the SRM model have been evaluated by experimental tests at low speeds. Conversion energy loops with soft chopping current control were recorded at speeds of 2,000 and 2,300 rpm as fig 2.25.
In each cycle of operation, the energy conversion loops are the areas enclosed to the magnetization curves from unaligned to aligned positions with the vertical lines at the currents of 250 and 300 A in fig 2.25. It is clear that the flux linkage results in dynamic and static measurement agree well.

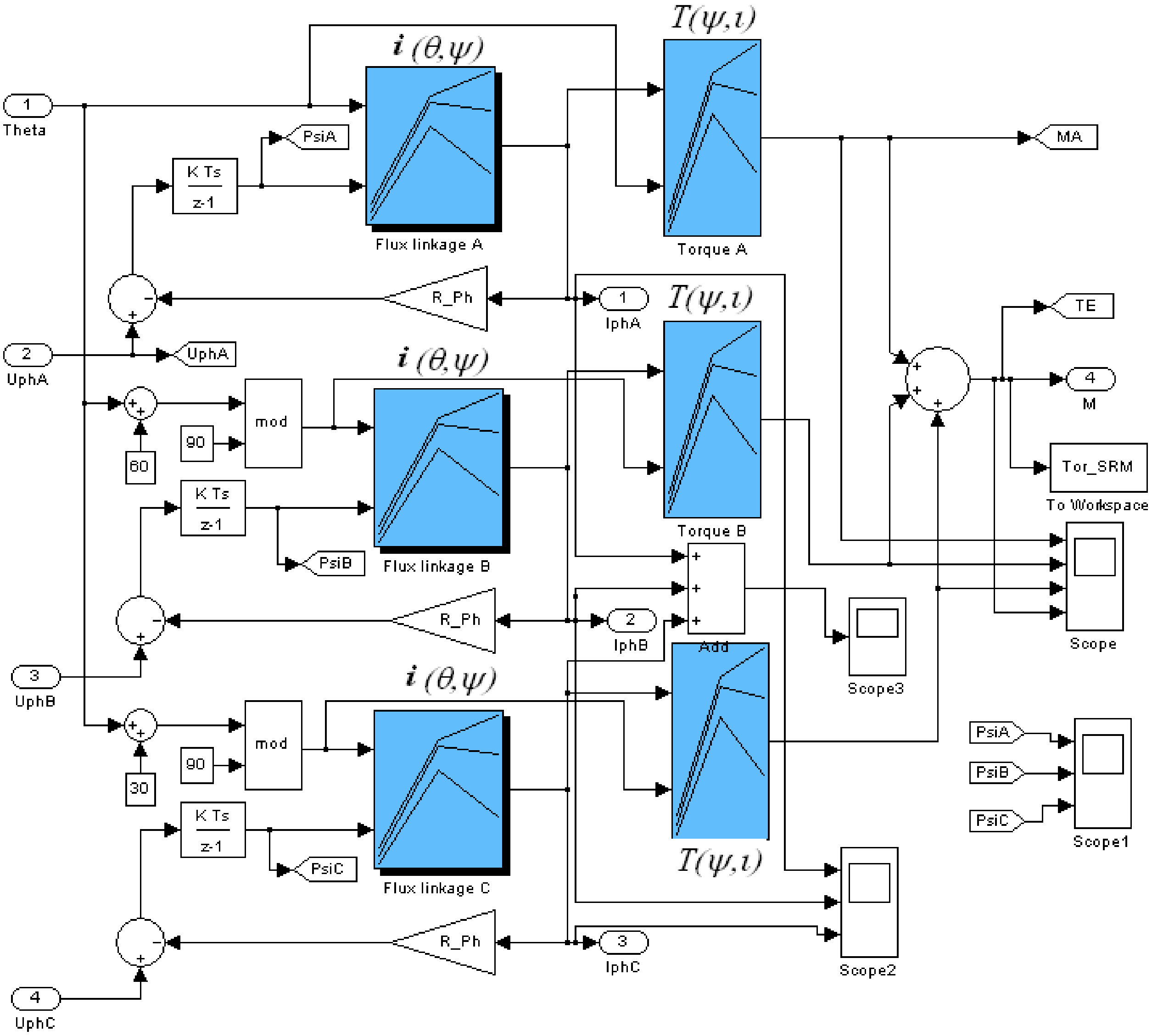

Figure 2.24: SRM simulation

Table 2.3: The SRM model parameters

Name	Parameters	Unit
Rotor inertia	J_R= $1.5{\cdot}10^{-3}$	kgm^2
Number tooth of Stator/Rotor	N_S/N_R =6/4	teeth
Stator tooth angle	$\beta_S = 30$	^{o}
Rotor tooth angle	$\beta_R = 32$	^{o}
Phase resistance	R =$9.7{\cdot}10^{-3}$	Ω

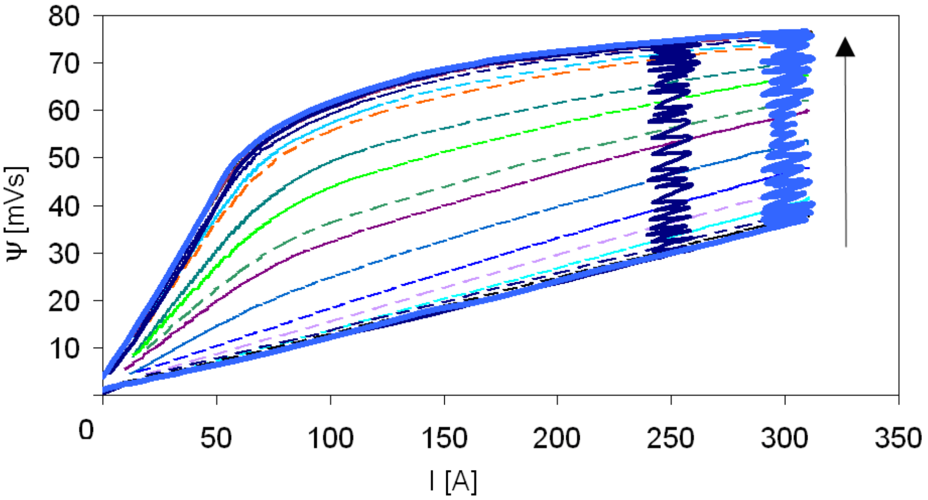

Figure 2.25: Energy conversion loops in chopping current control

2.7 Summary

After a brief introduction to operation of switched reluctance machines, several methods of determination of the static flux linkage curves $\Psi(\theta,\mathrm{I})$ have been explained and implemented in this chapter. Analytical reluctance and numerical FEA methods have been introduced. An accurate method was proposed the measurement of flux linkage characteristics of SRMs including the saturation properties. The method uses a measurement in three regions (energizing, de-energizing, and saturation) in order to remove the influence of iron loss effects during fast magnetization. The experimental results confirm the FEA static simulation.

3 Calculation of Losses and Thermal Analysis of High Speed Switched Reluctance Machines

The calculation of SRM losses is necessary in order to maximize efficiency. However, it is a big challenge due to the nonlinear magnetic characteristics, non-sinusoidal waveforms of the fluxes at high frequency. This chapter describes a different method for the iron loss calculation from the conventional methods. It figured out several sections of the SRM laminations with complex shapes which have the same iron loss density and flux waveforms. Rates of the iron loss densities were calculated at different frequencies and flux densities.
1. An iron loss model based on finite element analysis was used to determine the iron loss densities at high saturation and frequency. Secondly, the iron loss densities have been validated in static one-phase SR machine test with a frequency up to 3.5 kHz. For the dynamic experiment, a set of equipment setups has been built to be able to measure voltage, current and electric power over a wide frequency range.
The measurement results have been compared with iron loss data from steel manufacturers and the simulation results were compared with experimentally obtained measurements. Standard data sheets on material properties provided by steel manufacturers only contain magnetic test results with sinusoidal flux waveforms and homogeneous magnetic fields. However the flux waveforms in SRM are non-sinusoidal and include highly saturated flux density regions. Several static and dynamic tests have been carried out to determine the SRM iron losses and flux values for all operating points of the application. As far as comparable, the results agree with the data from steel manufacturers.
2. A temperature calculation due to iron and copper losses was investigated by a 3D finite element analysis. The temperature rises at stator yokes and windings were measured and validated. Some temperature sensors were located in the copper windings to measure the temperature. An infrared thermometer was installed in this motor to measure the rotor temperature as well.

3.1 SRM Losses Calculation and Measurement Methods

The losses can be separated into electrical P_{Cu}, magnetical P_{Fe}, and mechanical losses P_{mech}. The mechanical losses latter may be divided up further into bearing and air friction or windage losses, which are the most significant at high speed. In total, the loss components of the machine can be summarized as:

$$P_{loss} = P_{Cu} + P_{Fe} + P_{mech}, \tag{3.1}$$

3.1.1 Copper Losses

As for any other electric motor, the copper losses per phase are calculated based on the current square product with the winding resistance (3.2):

$$P_{Cu} = I_{RMS}^2 \cdot R \tag{3.2}$$

where R is the resistance of one phase winding. Normally, R is higher than the DC resistance of the conductors due to skin effects. I_{RMS} is the root mean square value of the phase current. According to [101], the penetration depth of eddy current varies with frequency:

$$\lambda = \sqrt{\frac{\rho}{\pi \cdot f \cdot \mu}} = \sqrt{\frac{1.678 \cdot 10^{-8}}{\pi \cdot 1100 \cdot 4 \cdot \pi \cdot 10^{-7}}} = 2 \tag{3.3}$$

Where,

$\rho = 1.678 \cdot 10^{-8}\ \Omega \cdot m$	conductor resistivity
$\mu = 4 \cdot \pi \cdot 10^{-7}\ H \cdot m^{-1}$	absolute magnetic permeability
$f = 1100\ Hz$	the frequency

The wire radius of 2 mm equals the penetration depth λ of the field at 1,100 Hz. Since the operating frequency of the machines exceeds this value(3,300 Hz at 50,000 rpm), the skin effect must be respected.

$$R = \frac{\rho \cdot l}{A_{eff}} = \frac{\rho \cdot l}{\pi \cdot r^2 - \pi \cdot (r - \lambda)^2} \tag{3.4}$$

Where,

A_{eff}	actual cross sectional area used due to skin effect
r	radius of the conductor

The actual resistance results was calculated as fig 3.1.

3.1.2 Iron Losses of the SRM

Many methods used to predict the SRM loss densities have been well known for some decades. Several methods for calculating iron losses with non-sinusoidal excitations have been published. They focus on estimating iron loss with the analysis of complex flux waveforms in [51], [55]. Fourier component and finite element methods have been applied in [49], [53] and [60].

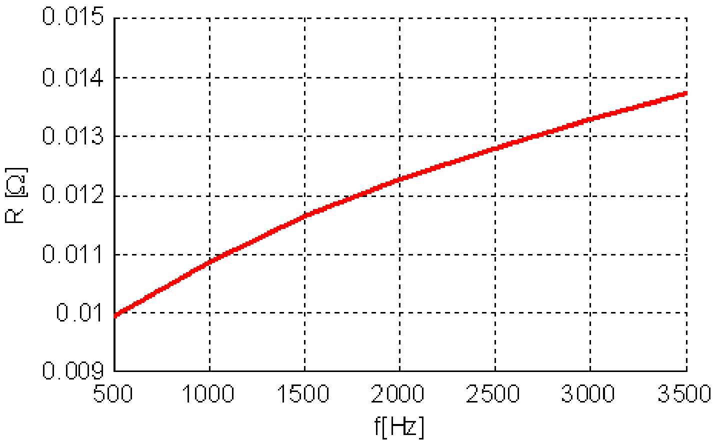

Figure 3.1: The phase resistance vs frequency due to skin effect

A 2D FEA Model

The flux densities B(θ,i) have been determined by a 2D FEA model. Fig 3.2 shows an example for aligned position at a constant current of 200 A. The flux waveforms of those sections are similar and the absolute values only depend on the cross section square. Flux densities of different lumped sections (yokes and teeth) have been investigated in a FEA model as depicted fig 3.2. The model has been simulated from the SRM lamination shapes, magnetic material properties and dimensional parameters.

Four lumped sections of the soft iron circuit with almost constant flux densities could be identified from fig 3.2: stator tooth (ST), stator yoke (SY), rotor tooth (RT), and rotor yoke (RY).

Iron Loss Densities

Iron loss density of each lumped sections can be obtained when a current is applied to one phase at each of rotor position and the SRM model was simulated at different frequencies by FEMM software [57]. The total iron losses are summarized from the iron loss densities and masses of the SRM components in (3.5):

$$p_{SRM} = \frac{\sum p_i \cdot m_i}{m_{SRM}} \tag{3.5}$$

where p_{SRM} is total iron density, m_{SRM} is the mass of the machine, p_i are iron loss densities of different parts, m_i are the masses of different parts (the teeth, yokes of SRM). The iron loss densities of the stator tooth p_{ST} (B_{ST}), stator yoke p_{SY} (B_{SY}), rotor tooth p_{RT} (B_{RT}) and rotor yoke p_{RY} (B_{RY}) are shown in fig 3.4. Based on the densities determined as above and the masses of the different parts, the relative iron loss density rates k_i are calculated as

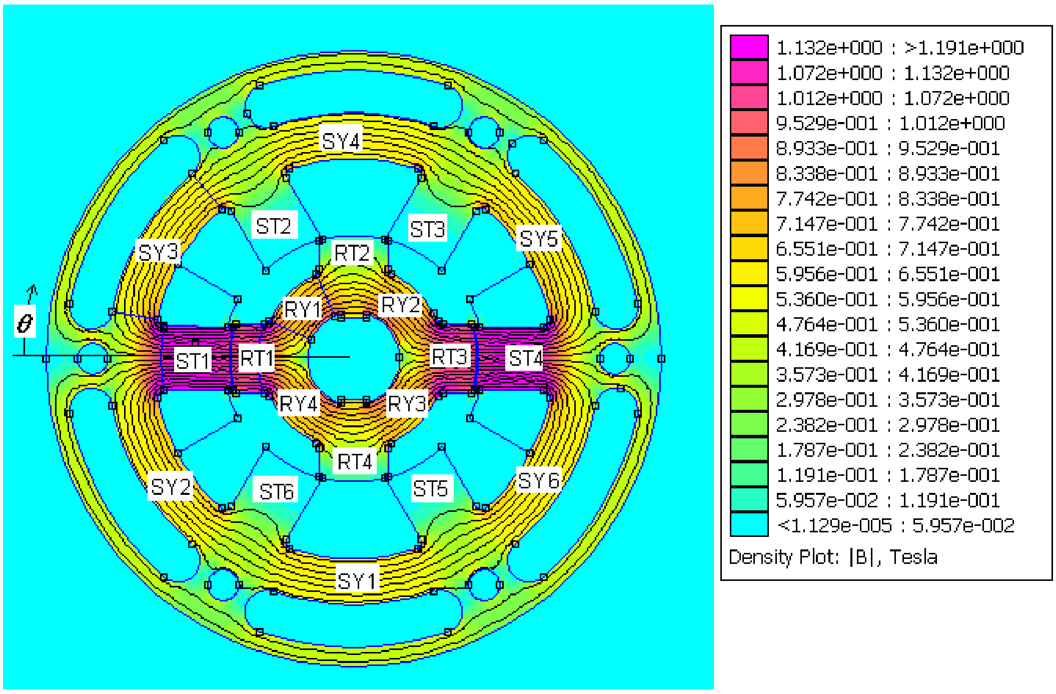

Figure 3.2: Flux densities of the SRM at aligned position

follows in (3.6).

$$k_i = \frac{m_i \cdot p_i}{\sum m_i \cdot p_i} = \frac{m_i \cdot p_i}{m_{SRM} \cdot p_{SRM}} \tag{3.6}$$

with Σk_i=1.
The iron loss density rates of the different parts are functions of the flux densities and frequencies. Fig 3.5 depicts an example calculated for equation 3.6. In one operating point, flux densities however are not equal in all parts.

It becomes clear that the iron loss factors k_i of stator and rotor teeth in fig 3.5 decrease with increasing flux densities because the flux densities in different parts are not proportional in magnetic saturation or the differences between fluxes in stator pole and other parts are not significant.

Analytical Model

An analytical model uses a formulation to calculate iron losses for lumped sections based on an analysis of the flux waveforms. The flux waveforms can be obtained when three windings are excited simultaneously by the currents with a shift angle between two phases of 60^o. Fig 3.6 shows the averaged flux densities in the four sections for constant current at variable rotor position.

Depending on the rotor angle θ, three phase currents will cause fluxes through any stator tooth. The flux densities in the stator teeth are unipolar. They have the same shape in the tooth carrying the exciting stator phases $B_{ST1}(\theta)$ and the teeth shifted by 60 ^{o} to either side

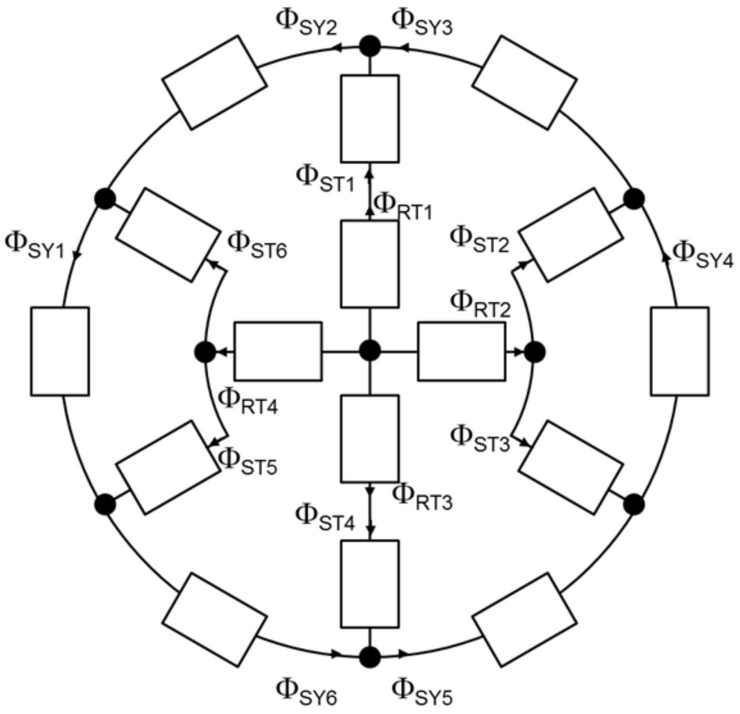

Figure 3.3: Magnetic circuit of four lumped sections

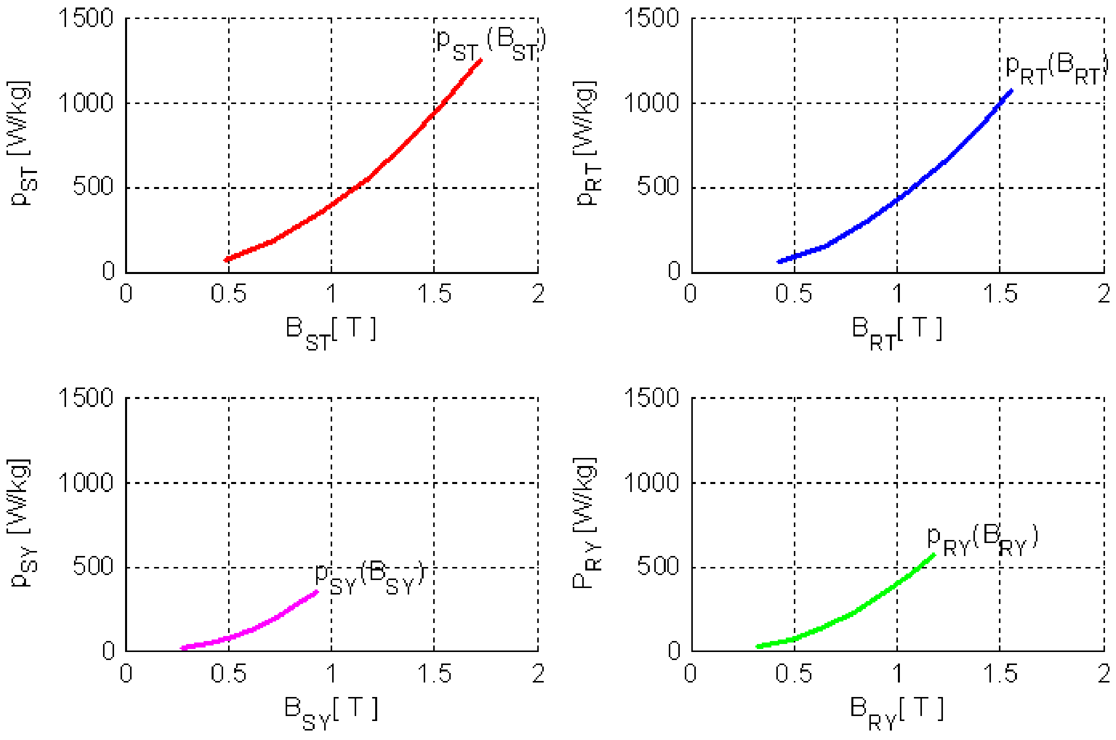

Figure 3.4: Iron loss densities of different parts

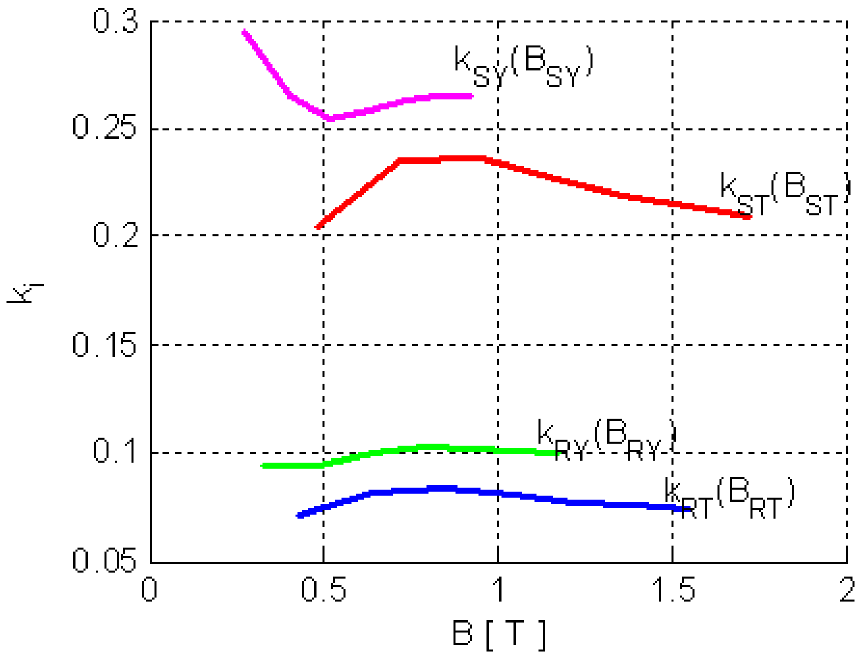

Figure 3.5: Core loss density rates of different parts at 2,500Hz

B_{ST3}, and B_{ST5}, while the others B_{ST4}, B_{ST6}, and B_{ST2} have the respective negative flux densities.

Iron loss calculation

The total iron losses can be separated into two major parts: hysteresis and eddy-current losses. A general formulation for the prediction of iron losses under non-sinusoidal fluxes uses the Miller equation according to [51].

$$p_{Fe} = C_e \cdot B_m^2 \cdot f^2 + C_h \cdot f \cdot B_m^{a+b \cdot B_m} \tag{3.7}$$

where C_e and C_h are the coefficients of eddy current and eddy current losses, and a and b are constants, and B_m is absolute value of flux density. The iron loss density is calculated in (W/kg).
Considering that the average of $(dB/dt)^2$ is equal to $B_m^2 \cdot f^2$ for the sinusoidal flux variation, the eddy-current loss term can be rewritten.

$$P_{Fe} = C_{e1} \cdot \left(\frac{dB}{dt} \right)^2 + C_h \cdot f \cdot B_m^{a+b \cdot B_m} \tag{3.8}$$

where $C_{e1} = C_e/(2 \cdot \pi)^2$.

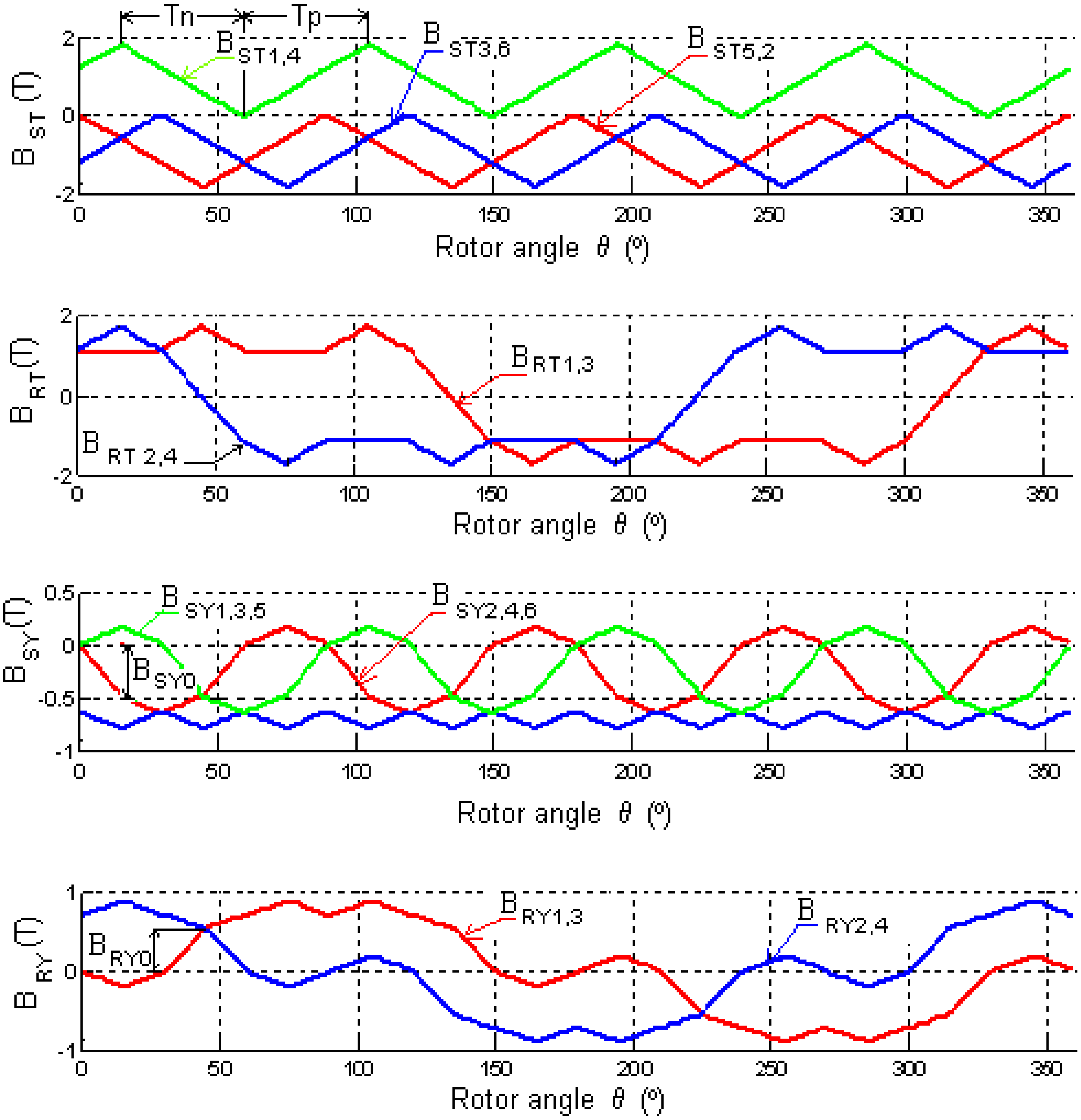

Figure 3.6: Flux densities of stator and rotor teeth and stator and rotor yokes over a single revolution of the rotor

Eddy-Current Losses

The eddy-current losses for the stator and rotor teeth P_{STe}, P_{RTe} are given by:

$$P_{STe} = \frac{\omega}{2 \cdot \pi} \cdot N_S \cdot N_R \cdot m_{ST} \cdot C_{e1} \cdot B_{STm}^2 \cdot \left(\frac{1}{T_p} + \frac{1}{T_n}\right) \tag{3.9}$$

$$P_{RTe} = \frac{\omega}{2 \cdot \pi} \cdot N_S \cdot N_R \cdot m_{RT} \cdot C_{e1} \cdot B_{RTm}^2 \cdot \left(\frac{1}{T_p} + \frac{1}{T_n}\right) \tag{3.10}$$

Where,

m_{ST}	the mass of one stator tooth
m_{RT}	the mass of one rotor tooth
B_{STm}	the maximum of flux density in the stator tooth
B_{RTm}	the maximum of flux density in the rotor tooth
T_p	the rise time of the flux
T_n	the fall time of the flux

The eddy-current losses for the stator and rotor yokes P_{SYe}, P_{RYe} are given by:

$$P_{SYe} = \frac{\omega}{2 \cdot \pi} \cdot N_R \cdot N_S \cdot m_{SY} \cdot C_{e1} \cdot \left(\frac{2 \cdot B_{SYm}^2}{T_n} - h_{SYe} \cdot \frac{B_{SYm} \cdot B_{SY0}}{T_n}\right) \tag{3.11}$$

$$P_{RYe} = \frac{\omega}{2 \cdot \pi} \cdot N_R^2 \cdot m_{RY} \cdot C_{e1} \cdot \left(\frac{2 \cdot B_{RYm}^2}{T_n} - h_{RYe} \cdot \frac{B_{RYm} \cdot B_{RY0}}{T_n}\right) \tag{3.12}$$

Where, the h_{SYe} and h_{RYe} are the coefficient factors normalized count of the flux polarity changes.

Hysteresis Losses

The hysteresis losses can be calculated by a process described in [51]. The classical equation describing the hysteresis losses was given by as,

$$P_h = C_h \cdot f \cdot B_m^{a+b \cdot B_m} \tag{3.13}$$

The hysteresis loss for stator teeth are:

$$P_{STh} = \frac{\omega}{2 \cdot \pi} \cdot N_S \cdot N_R \cdot m_{ST} \cdot e_h(0,B_{STm}) = \frac{\omega}{2 \cdot \pi} \cdot N_S \cdot N_R \cdot m_{ST} \cdot C_h \cdot 0.4 \cdot \left(B_{STm}^{a+b \cdot B_{STm}}\right) \tag{3.14}$$

where $e_h(0,B_{STm})$ is the hysteresis loss energy per unit weight for a minor loop where flux density changes between 0 and B_{SPm} and $e_h(-B_{STm},B_{STm})$ is the hysteresis loss energy per unit weight for a full loop where flux density changes between -B_{SPm} and B_{SPm}. Because the hysteresis loss of a minor loop is about 40% of the full loop it was calculated as in (3.15):

$$e_h(0{,}B_{STm}) = 0.4 \cdot e_h(-B_{STm}{,}B_{STm}) = 0.4 \cdot C_h \cdot \left(B_{STm}^{a+b\cdot B_{STm}}\right) \tag{3.15}$$

The hysteresis losses for rotor teeth are:

$$\begin{aligned} P_{RTh} &= \frac{\omega}{2\cdot\pi} \cdot N_S \cdot N_R \cdot m_{RT} \cdot \left(\frac{h_{RTh}}{2} \cdot e_h(-B_{RTm}{,}B_{RTm}) + (1-h_{RTh}) \cdot e_h(0{,}B_{RTm})\right) \\ &= \frac{\omega}{2\cdot\pi} \cdot N_S \cdot N_R \cdot m_{RT} \cdot C_h \cdot \left(\frac{h_{RTh}}{2} \cdot B_{RTm}^{a+b\cdot B_{RTm}} + (1-h_{RTh}) \cdot 0.4 \cdot B_{RTm}^{a+b\cdot B_{RTm}}\right) \end{aligned} \tag{3.16}$$

where $e_h(0{,}B_{RTm})$ and $e_h(\text{-}B_{RTm}{,}B_{RTm})$ are the hysteresis loss energy for minor and full hysteresis loops.
The hysteresis losses for stator yoke is:

$$\begin{aligned} P_{SYh} &= \frac{\omega}{2\cdot\pi} \cdot N_S \cdot N_R \cdot m_{SY} \cdot \left(\frac{h_{SYh}}{2} \cdot e_h(-B_{SYm}{,}B_{SYm}) + (1-h_{SYh}) \cdot e_h(B_{SY0}{,}B_{SYm})\right) \\ &= \frac{\omega}{2\cdot\pi} \cdot N_S \cdot N_R \cdot m_{SY} \cdot C_h \cdot \left(\frac{h_{SYh}}{2} \cdot B_{SYm}^{a+b\cdot B_{SYm}} + (1-h_{SYh}) \cdot \frac{B_{SYm}-B_{SY0}}{B_{SYm}} \cdot B_{SYm}^{a+b\cdot B_{SYm}}\right) \end{aligned} \tag{3.17}$$

where $e_h(B_{SY0}{,}B_{SYm})$ is the hysteresis loss energy for a minor hysteresis loop where flux density changes between B_{SY0} and B_{SYm}.
The hysteresis losses for rotor yoke is:

$$\begin{aligned} P_{RYh} &= \frac{\omega}{2\cdot\pi} \cdot N_R^2 \cdot m_{RY} \cdot C_h \cdot \left(\frac{h_{RYh}}{2} \cdot e_h(-B_{RYm}{,}B_{RYm}) + (1-h_{RYh}) \cdot e_h(B_{RY0}{,}B_{RYm})\right) \\ &= \frac{\omega}{2\cdot\pi} \cdot N_R^2 \cdot m_{RY} \cdot C_h \left(\frac{h_{RYh}}{2} \cdot B_{RYm}^{a+b\cdot B_{RYm}} + (1-h_{RYh})\frac{B_{RYm}-B_{RY0}}{B_{RYm}} \cdot B_{RYm}^{a+b\cdot B_{RYm}}\right) \end{aligned} \tag{3.18}$$

where $e_h(B_{RY0}{,}B_{RYm})$ is the hysteresis loss for a minor hysteresis loop where flux density changes between B_{RY0} and B_{RYm}.

$a = 1.615; b = 0.158T^{-1}$	the constant factors of eddy current losses
$C_e = 1.8 \cdot 10^{-6} W \cdot \mathrm{s}^2 \cdot T^{-2} \cdot kg^{-1}$	the coefficient factor of eddy current losses
$C_h = 8.2 \cdot 10^{-3} W \cdot \mathrm{s} \cdot T^{-(a+b\cdot B_m)} \cdot kg^{-1}$	the coefficient factor of hysteresis losses
$h_{SYe} = 1/3; h_{RYe} = 1/2$	the effect of the winding polarities on eddy current losses
$h_{SYh} = 1/3; h_{RYh} = 1/2; h_{RTh} = 1/2$	the effect of the winding polarities on hysteresis losses

Those factors have been obtained from the iron loss data sheet of the manufacturer [32].

3.1.3 Iron Loss Validation

The test bench for the iron loss measurement is the experiment setup of the flux linkage measurement in chapter two as fig 2.14. However, the phase windings were excited by a high frequency. In order to obtain a full of voltage and current waveform, the DAQ (NI-USB-6212) was initialized with 100kS/s and 2000 samples. Both flux densities and the iron losses in different parts of the iron will be calculated from recorded data.

Experiment Method for Measuring Iron Losses

A non-sinusoidal flux density waveform is obtained by applying an almost square-wave voltage with high switching frequency as shown in fig 3.7 upper left side. However, the measured voltage has a roughly triangular shape due to a low feedback frequency of the voltage sensor. Especially, the voltage changed from -U_{DC} to $+U_{DC}$.

In this experiment, the flux linkage $\Psi(t)$ has been calculated from the voltage and current waveforms firstly. The flux density of the stator tooth is inferred based on the flux linkage, number of turns and cross sectional area in (3.19).

$$B_{ST}(t) = \frac{\Psi(t)}{N_t \cdot A_{ST}} = \frac{1}{N_t \cdot A_{ST}} \cdot \int_0^t (u(\tau) - i(\tau) \cdot R) d\tau \tag{3.19}$$

where $u(\tau)$ is the terminal voltage across phase winding, R is the resistance of the phase winding, $i(\tau)$ is the phase current, N_t is the number of turns per phase, and A_{ST} is the cross sectional area of the stator tooth.

From the average input power during both magnetizing and demagnetizing phases, the total input losses P_{in} can be determined. The iron losses P_{FE} are computed as the difference between total input power P_{in} and copper losses P_{Cu} according to (3.20):

$$P_{FE} = P_{in} - P_{Cu} \tag{3.20}$$

The power values were averaged during one period of fig 3.7. The loss densities p_i are calculated according to (3.21):

$$p_i = \frac{k_i \cdot \sum m_i \cdot p_i}{m_i} = \frac{k_i \cdot P_{Fe}}{m_i} \tag{3.21}$$

Comparison Between Simulated and Experimental Iron Losses

The results on iron loss densities in both FEA model and measurement are shown in fig 3.8. In comparison with the simulation method, the experimental results of the iron loss densities are slightly higher. The mismatch can be explained by the residual magnetic flux.

The simulated and measured iron losses at different frequencies are compared in fig 3.9. The differences are supposed to be due to the 2D FEA model, which does not take into account the field of the end windings, the lacking accuracy of the non-linear B-H curves, and the remnant fluxes. Moreover, the measured waveforms were not as perfect as in the simulation, as they depend on the recording of the frequency of the voltage and current sensors and the delay time of the electronic devices.

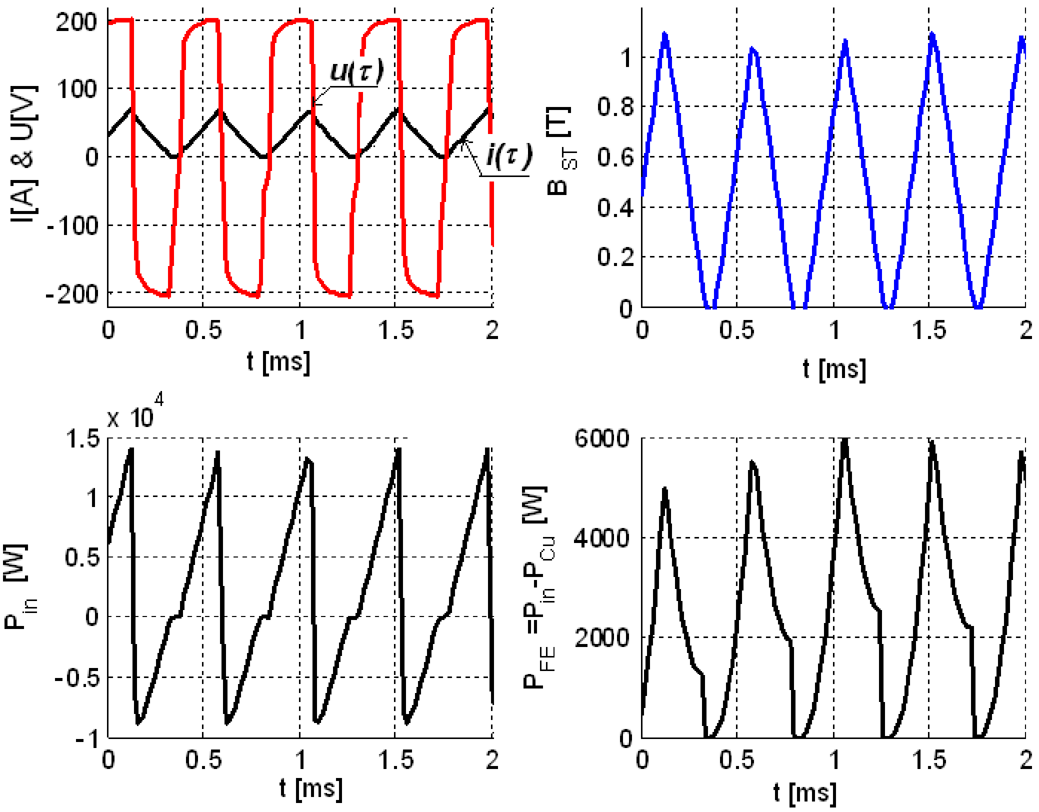

Figure 3.7: Voltage, current and flux density waveforms at 2500 Hz

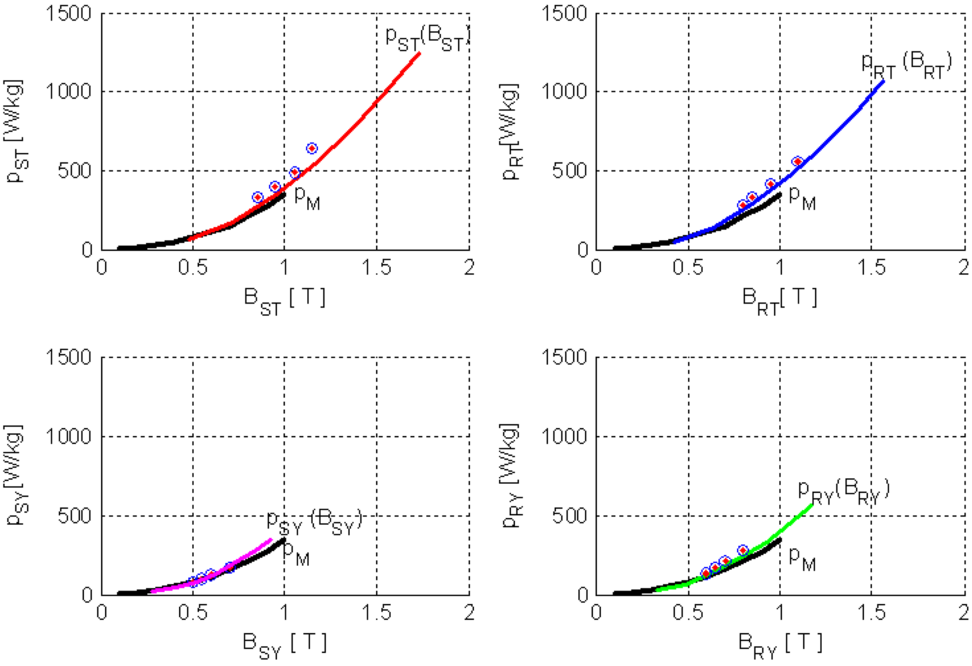

Figure 3.8: Core loss densities comparison at 2,500 Hz (color lines: simulation, black line: manufacturer, dot: measurement)

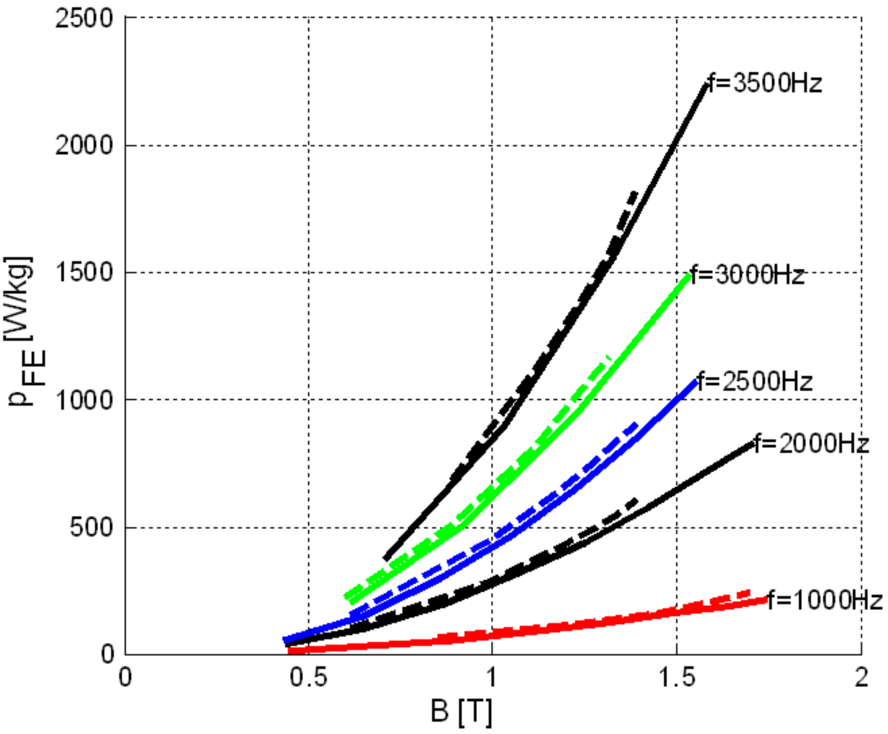

Figure 3.9: Core loss density comparison between simulation (lines) and measurement (dashed)

3.1.4 Mechanical Losses

The mechanical losses in the SRM consist mainly of air friction losses and bearing losses. They are assumed not to depend on load. Rotor speed, air gap and the stack length influence the air friction losses P_{fr}. An analytical calculation is quite difficult due to the complex air flow conditions including laminar and turbulent regions. According to [58], an empirical formula is given in (3.22)

$$P_{fr} = 2 \cdot k_{fric} \cdot r_r (L_{stk} + 0.6 \cdot \tau_r) \cdot v_r^3 \tag{3.22}$$

where v_r is the circumferential speed of the rotor, r_r is the outer rotor radius, L_{stk} is the rotor length, τ_r is the stator tooth pitch and k_{fric} is friction coefficient for electrical machines. The bearing loss P_{br} depends on a frictional torque factor T_{ft} and can be calculated as follows (3.23).

$$P_{br} = T_{ft} \cdot \omega \tag{3.23}$$

In order to validate those mechanical losses, the machine has been accelerated up to several speeds without load. After switching off the current, the run out speed is recorded vs. time. The deceleration speed is continuously measured until the rotor comes to standstill. The mechanical power loss P_{mech} at the measured speed n_m is determined based on the deceleration speed curve in fig 3.10 (3.24):

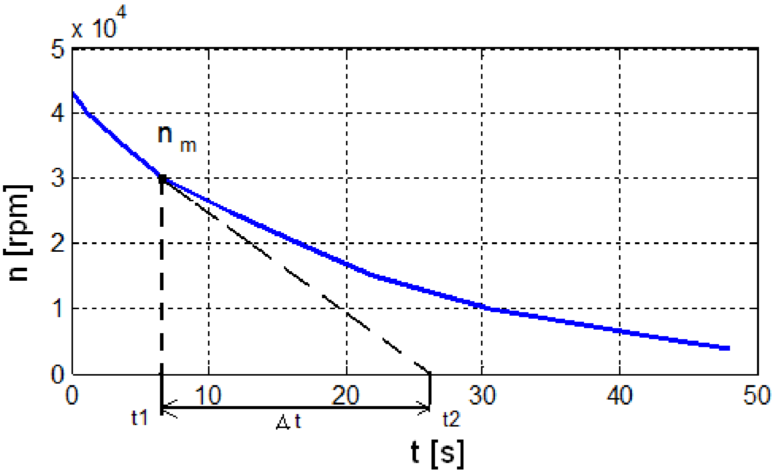

Figure 3.10: The deceleration curve

$$-P_{mech} = -T_{mech} \cdot \omega = J_R \cdot 4 \cdot \pi^2 \cdot n \cdot (\frac{dn}{dt})_{n=n_m} = J_R \cdot 4 \cdot \pi^2 \cdot n \cdot (\frac{n_m}{\Delta t}) \tag{3.24}$$

where T_{mech} is the torque corresponding to the mechanical power loss P_{mech}, J_R is moment of rotor inertia and ω is the angular velocity.
The determination of the speed derivative by graphical construction of the tangent to the speed curve implies some inaccuracies. However, in case of numerical acquisition of data, the calculation can be done numerically with more precise results [61]. The calculated (blue line) and measured (black line) mechanical losses in fig 3.11 are quite good agreement.

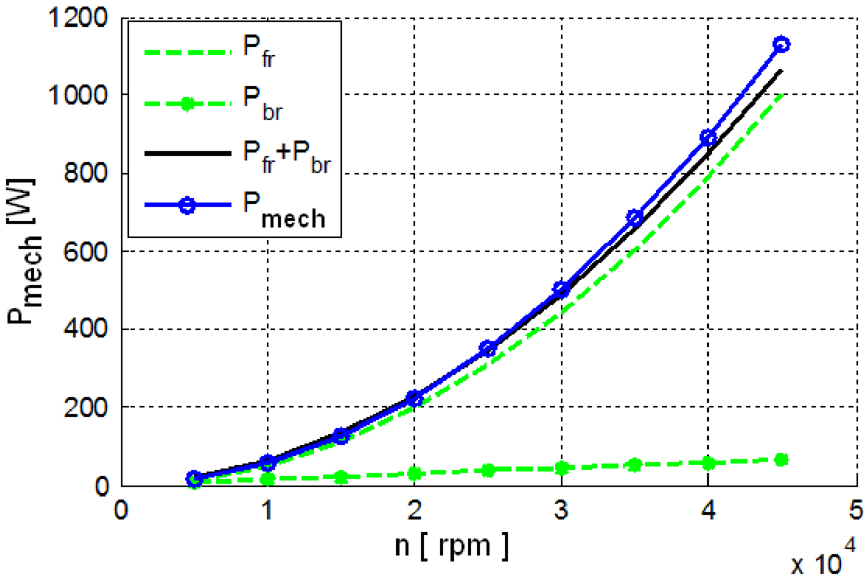

Figure 3.11: The calculated (blue line) and measured (black line) mechanical losses

Loss Separation in High Speed Steady State Operation Without Load

The copper, iron and mechanical losses were determined experimentally at high speed operation, where air friction already applies sufficient torque to render accurate results. The total losses P_t are computed from the measured input currents and voltages. The copper losses P_{Cu} can be calculated from the currents and the stator resistance. Fig 3.11 already depicted the mechanical loss P_{mech}. The difference is regarded as iron losses P_{Fe} according to (3.25):

$$P_{Fe} = P_t - P_{Cu} - P_{mech} \tag{3.25}$$

Table 3.1 shows some results with different turn-on and turn-off angles at various speeds. All results show a good agreement between the model and measurement.

Table 3.1: Losses measured in no-load test

speed [rpm]	40,000	43,000	45,000
P_t [W]	2,230	2,526	3,200
P_{Cu} [W]	24	25	27
P_{mech} [W]	888	980	1,150
$P_{Fe}(mea)$ [W]	1,380	1,521	2,023
P_{Fe}(cal) [W]	1,290	1,440	1,930
Difference[%]	6.5	5.9	4.6

3.2 Thermal Analysis

After loss determination, a thermal analysis shall investigate the power capability of the machine. The water cooling jacket is included in the stack: using sheets covered with thermal varnish, the mounted stack was baked in an oven at 200 °C thus providing watertight pockets. The flanges of the housing were machined in order to lead the water to external tubes for connecting the pockets which can later be easily replaced by a machined flange for production facilitation.

The 2D and 3D finite element analyses were used to calculate the temperature distribution considering also the water cooling system. From this model, an optimal water flow rate can be determined. The convection coefficients between different parts were estimated analytically and applied to the FEA thermal model. In oder to validate the influence of the water flow rate, the temperature distribution was studied and the results have finally been compared in a no load test. Computational fluid dynamics (CFD) was used to simulate the fluid velocity distribution in the cooling pockets.

3.2.1 Determination of Heat Transfer Coefficients

An accurate estimation of surface convective heat transfer coefficients is necessary for the FEA thermal analysis model. There are many applications and papers on the subject of airflow or water cooling convection in rotating electrical machines through housings e. g. in [65], [77] and [78]. However, the stator lamination in fig 3.12 cooled directly by fluid has not yet been mentioned.

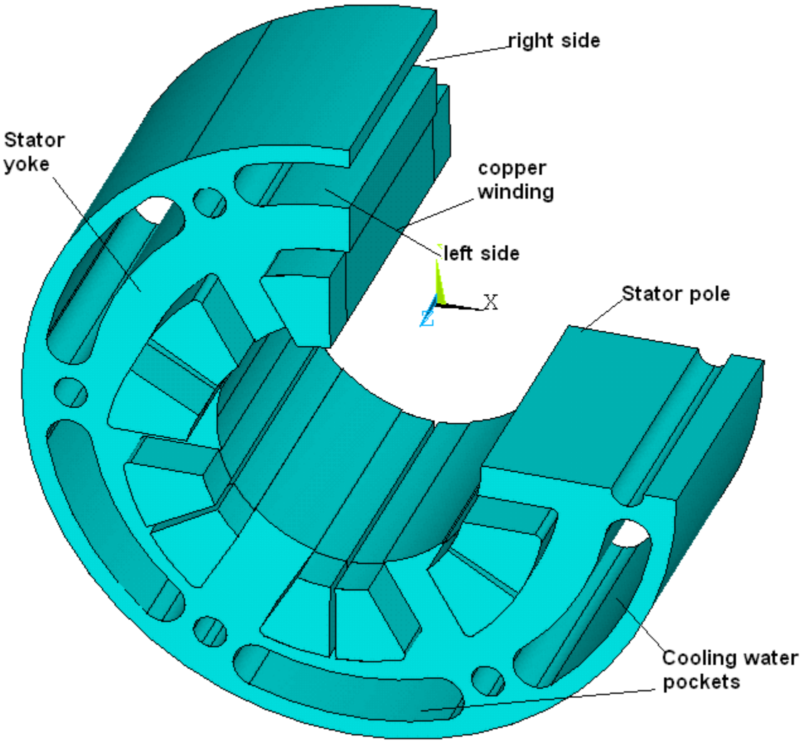

Figure 3.12: Stator and rotor of the investigated SRM

CFD Model

Fig 3.12 depicts the geometry of the 6 water pocket tubes in the stator yoke. The cold fluid enters the pipe through the right side connection and the hot fluid leaves the pipe through the left side. The heat transfer takes place in the surfaces between stator yoke and fluid.

The purpose of CFD is to investigate the fluid velocities and pressure drop as depicted in fig 3.13. Those results were used to calculate the average fluid velocity as well as for dimensioning the pump of the cooling system. The simulation was carried out with the student version of ANSYS 11 turbulent flow of fluid dynamics (CFD) software.

Forced Convection of Water Jacket

In a forced convection system, the value of the Reynolds number Re in equation (3.26) judges if the flow is laminar or turbulent. In this case, ($3000 < \mathrm{Re} < 10^6$) resulting in turbulent modeling as [66]. The heat transfer coefficient of the turbulent flow in the water jacket can be

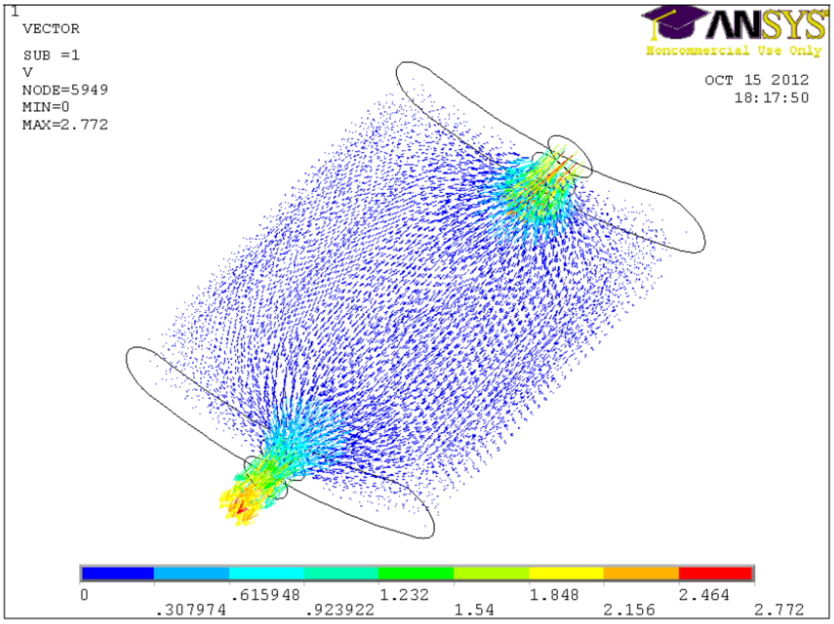

Figure 3.13: Fluid velocity distribution in water jacket v_{av} (m/s)

analytically calculated according to [63]. The heat transfer coefficients depend on the fluid velocity, dynamic viscosity and hydraulic diameter. An accurate prediction of the forced water coefficient is a big challenge. In this dynamic simulation, the fluid velocity distribution was determined by a CFD model for different flow rates. The average velocity was then used to calculate the Reynolds number as in equation 3.26. Based on the channel shapes and geometry parameters, the hydraulic diameter results from (3.27). Those equations render the heat transfer coefficient as depicted in fig 3.14.

$$Re = \frac{v_{av} \cdot D_h}{\mu_{fluid}} \tag{3.26}$$

where Re is the Reynolds number, which decides the flow status, v_{av} is the average fluid velocity, μ_{fluid} is the fluid dynamic viscosity, and D_h is the hydraulic diameter as in (3.27):

$$D_h = \frac{4 \cdot A_c}{P_c} \tag{3.27}$$

where A_c and P_c are the cross section area and the contour length of the water channel, respectively.

For this application the Nusselt number can be calculated according to V.Gnielinski [66] as follows:

$$Nu = \frac{(f_{Nu}/8) \cdot (Re - 1000) \cdot Pr}{1 + 12.7(f_{Nu}/8)^{1/2} \cdot (Pr^{2/3} - 1)} \tag{3.28}$$

with f_{Nu} is the friction factor in (3.29) and Pr is the Prandtl number in (3.30) according to [66] :

$$f_{Nu} = [0.79 \cdot ln(Re) - 1]^{-2} \tag{3.29}$$

$$Pr = \frac{\mu_{fluid}}{\alpha_f} \tag{3.30}$$

where α_f is the fluid thermal diffusivity. Finally, the heat transfer coefficient $h_{fluid-core}$ according to [63] follows as (3.31):

$$h_{fluid-core} = \frac{k_{fluid} \cdot Nu}{D_h} \tag{3.31}$$

with k_{fluid} is the thermal conductivity of fluid.
Fig 3.14 depicts the results of these equations (refers to 3.26 -3.31) for different flow rates. Boundary conditions were then applied to the water jacket, and the temperature field distribution was obtained as shown in fig 3.16.

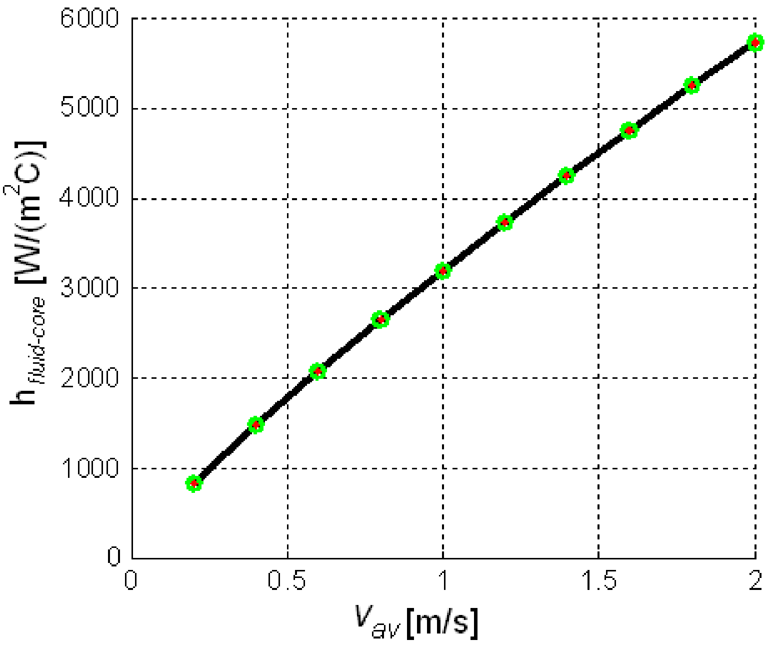

Figure 3.14: The heat transfer coefficient core between fluid and surface

Heat Transfer Coefficient of the Air Gap

The convective heat transfer coefficient of the surfaces in the air gap is very difficult to compute due to the influence of the complicated shape of the air gap. Based on the empirical formulas in [70], the heat transfer coefficient for the air gap was calculated as follows (3.32-3.34):

$$Re_{gap} = \frac{v_{gap} \cdot g}{\mu_{air}} \tag{3.32}$$

with $v_{gap} = r_r \cdot \omega$ equivalently to (3.26)

$$Nu_{gap} = 0.03 \cdot Re_{gap}^{0.8} \tag{3.33}$$

$$h_{gap} = \frac{k_{air} \cdot Nu_{gap}}{g} \tag{3.34}$$

Where ω is the angular velocity of the rotor, r_r is the radius of the rotor, g is the length of air gap, μ_{air} is the dynamic viscosity of the air, k_{air} (m^2/s) is the thermal conductivity of air. Fig 3.15 shows convective heat transfer coefficient of the surfaces in the air gap between rotor and stator. It is clear that this factor increases with speed.

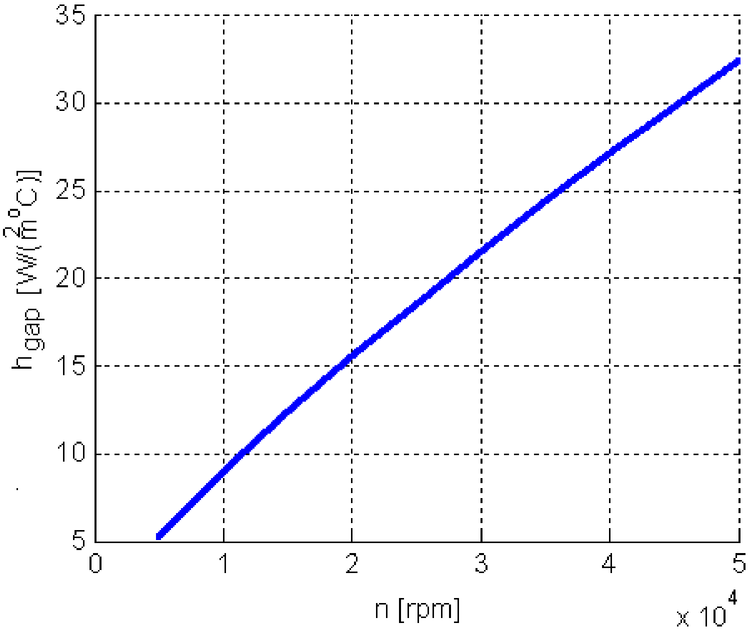

Figure 3.15: The heat transfer coefficient surface between air and laminations

Flow Rate Calculation

In the application of an aircraft, the active part of the SRM is closed. Therefore, an efficient cooling system is necessary in order to reduce mechanical stress and wear. In electric vehicle applications, forced liquid cooling is frequently used as analyzed e. g. in [73]. The required minimum flow rate to remove the heat produced by the losses can be obtained by (3.35):

$$Q_{min} = \frac{\sum P_{loss}}{\rho_{fluid} \cdot c_{p,fluid} \cdot (T_{out} - T_{in})} \tag{3.35}$$

where $\sum P_{loss}$ is the total loss heated by iron and mechanical losses, Q_{min} is the mass flow in kg/s, $c_{p,fluid}$ is the specific heat of the cooling water J/(kg·K), ρ_{fluid} is fluid mass density in kg/m^3, and (T_{out}-T_{in}) is the difference between inlet and outlet temperature.
In order to remove internal heat losses generated in the SRM, the cooling fluid has to circulate through the jacket at turbulent flow.

3.2.2 FEA Thermal Analysis Model

3D FEA models have been used to investigate the temperature distribution for many types of electrical machines e.g. in [25] and [26]. However, the thermal analysis of SRM with significant friction and electrical loss contributions are still a big challenge, because the iron loss densities of rotor and stator parts are totally different. Moreover, with the complex rotor tooth shapes, the heat transfer coefficients of the air gap as well as the core ends of stator and rotor tooth surfaces have to be estimated in different conditions. In order to observe an actual temperature distribution in the parts of the machine, a three dimensional steady state thermal analysis of stator core, air gap and windings was done.

Numerical Formulation

The formulation of temperature rise analysis is based on the heat conduction equation shown in 3.36.

$$\frac{\partial}{\partial x}(k_x \cdot \frac{\partial T_{rise}}{\partial x}) + \frac{\partial}{\partial y}(k_y \cdot \frac{\partial T_{rise}}{\partial y}) + \frac{\partial}{\partial z}(k_z \cdot \frac{\partial T_{rise}}{\partial z}) + \dot{Q} = \rho \cdot c \cdot \frac{\partial T_{rise}}{\partial t} \tag{3.36}$$

Boundary conditions at the surfaces S1 (symmetry of teeth) and S2 (axial surface of core) in fig 3.16 are as follows (3.37) and (3.38):

$$-k \cdot \frac{\partial T_S}{\partial n}|_{S1} = 0 \tag{3.37}$$

$$-k \cdot \frac{\partial T_S}{\partial n}|_{S2} = h_i \cdot (T_\propto - T_S) \tag{3.38}$$

where k_x, k_y, k_z are the thermal conductivities in the spatial directions x,y,z of an anisotropic material, ρ is the density, c is heat capacity, and $\dot{Q}$ is internal heat generation rate. Taking into consideration the convective heat exchange on the surface of the SRM, the convection boundary conditions are applied to $S1$ and $S2$ surface conditions. $T_\propto$ and T_S are the surface and air temperature, respectively, and h_i denote the heat transfer coefficients.

Stator Temperature

With the geometrical parameters and the material properties of each part, a three dimensional steady-state temperature field simulation model for the liquid cooled SRM was established. The boundary conditions of the surface in the stator yokes and teeth were determined by (3.37) and (3.38). For the water pockets, the heat transfer coefficients have been calculated in the analytical model and can now be applied for the FEA model. The temperature distribution was calculated based on copper and iron losses at different speeds and reference currents. Fig 3.16 shows an example operation point at speed of 15,000 rpm and current of 40A.

The temperature field of the stator is generated by iron and copper losses. The temperature of the stator tooth achieves the highest value due to the distance to the liquid cooling pocket. Moreover, the heating by friction loss in the air gap increases the temperature in the tooth heads. The outer stator yoke contacts directly the fluid leading to a low temperature there.

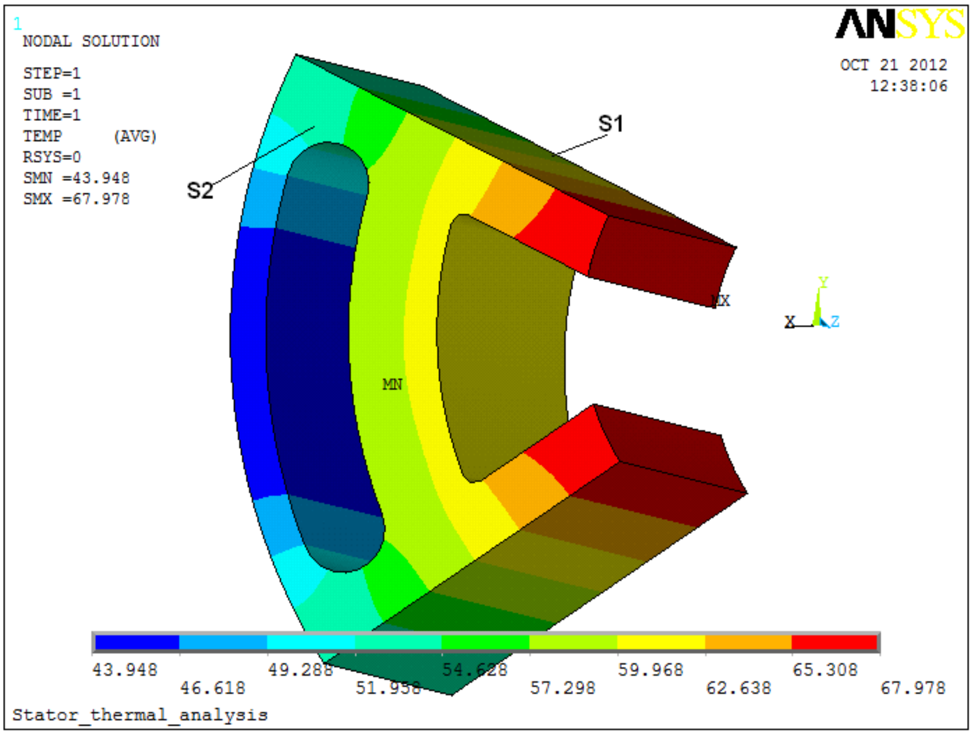

Figure 3.16: Stator temperature distribution

Temperature of Windings

The winding of the machine consists of insulation, air and copper wires. These materials have totally different thermal behaviors. It is common practice to consider an equivalent thermal conductivity coefficient for the winding. The equivalent conductivity of the winding depends on the filling factor [81]. In this SRM, the winding consists of 220 conductors in serial connection and each conductor consists of 20 copper strands connected in parallel. With the filling factor of 0.6, the equivalent conductivity of the winding is 0.7 W/(m.K) in [80].

Therefore the coils were modeled as massive conductors placed between the stator teeth. The temperature of these copper bars has its maximum in the axial center of the stator slots, while they are lowest close to the surface between winding bars and stator yokes, which is nearest to the cooling system.

Temperature Distribution in Air Gaps

In a high speed motor, the temperature in the air gap is significant due to the friction losses and the friction loss causes additional heating. Moreover, the internal heat sources of SRM cores, yokes and windings have a strong influence on the whole motor temperature distribution. In order to investigate the mutual effects, a 2D FEA thermal analysis model was simulated with the air gap heat transfer coefficient which has been calculated in fig 3.15. Fig 3.18 depicts the temperature distribution of the air gap. The hot spot temperature inside of the SRM is 90 ^{o}K in the head points of the stator windings shown in fig 3.18.

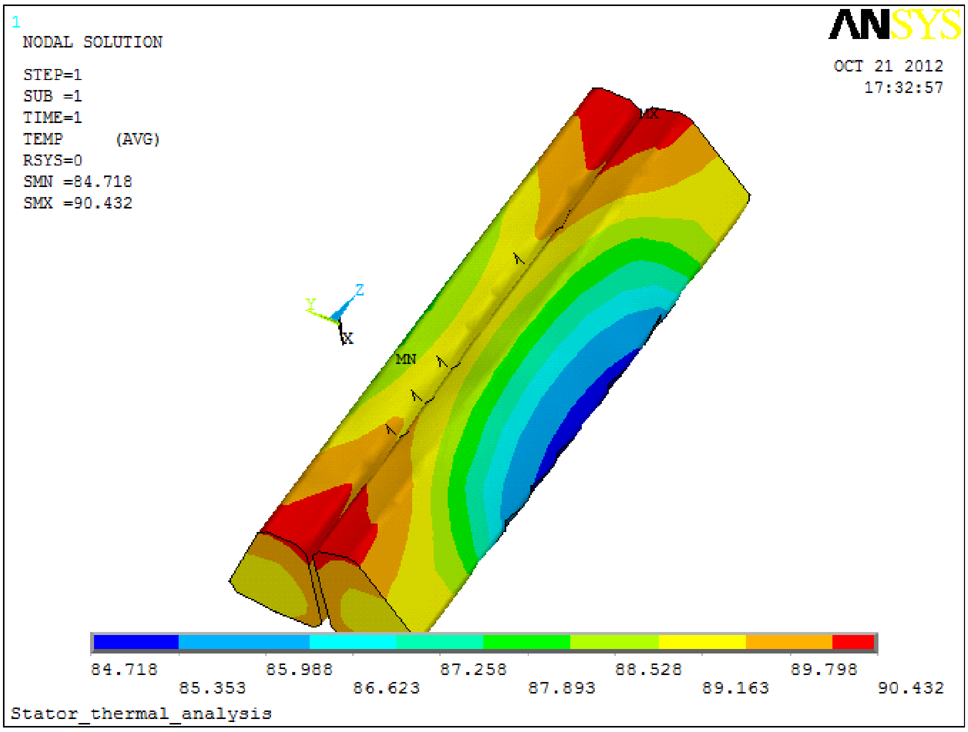

Figure 3.17: Copper winding temperature

Temperature Rise Curves in Transient Thermal Analysis

In this transient thermal analysis, the time needed to reach end temperatures is 150 seconds starting from ambient temperature. Fig 3.19 shows the simulation results of the SRM temperature. The end temperature of end windings, cores and yokes is reached shortly after 60 seconds. The temperature rise according to the simulation is 90 ^{o}K at the end windings, 68 ^{o}K at the stator tooth, 63 ^{o}K at the yoke, and 58 ^{o}K at the air gap.

Measurement of Temperature Rise Curves

In the experimental setup several PT100 temperature sensors and a data acquisition device NI-USB 6212 monitored by LabVIEW were used. The sensors were placed in the end windings, close to the resolver and close to the bearing. As expected, the end windings achieve the highest temperature.

Fig 3.20 shows the temperature rise at 15,000 rpm and an excitation current of 40A. The temperature increased from a room temperature of 28^{o}K. Because the temperature measurement was carried out without load, the end temperature is not so high.

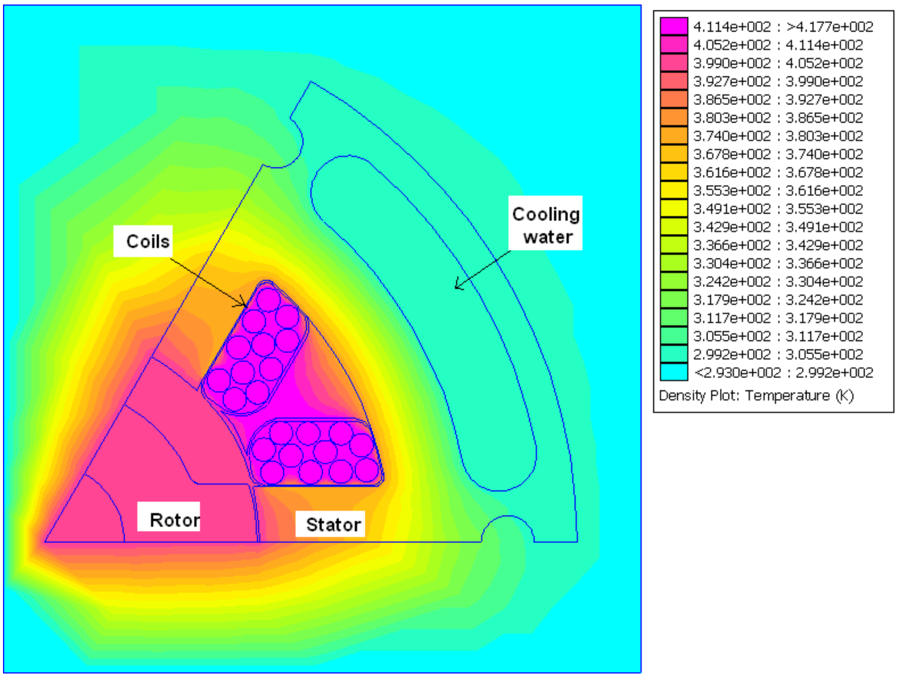

Figure 3.18: 2D FEA temperature distribution

3.3 Summary

The iron losses and temperature distribution for a high speed SRM have been investigated both by simulation and experimental methods. An improved measurement technique was used to predict the iron losses at high frequency and flux density. This method allows a detailed analysis of the iron loss rates in predefined rotor and stator parts characterized by constant flux density. It was applied in different rotor positions at standstill. Due to a lack of load, measurements were carried out both in dynamic operation during acceleration and no load steady state at various speeds. The mechanical losses have been separated by run down tests. Since the copper loss can be predetermined, the total iron losses result from total losses by loss separation. The temperature distribution of different parts in SRM has been investigated by 3D and 2D FEA modeling and the fluid velocity distribution in the stator jackets was simulated by a CFD model. The influence of the flow rate of the liquid stator cooling on the temperature distribution was calculated and discussed.

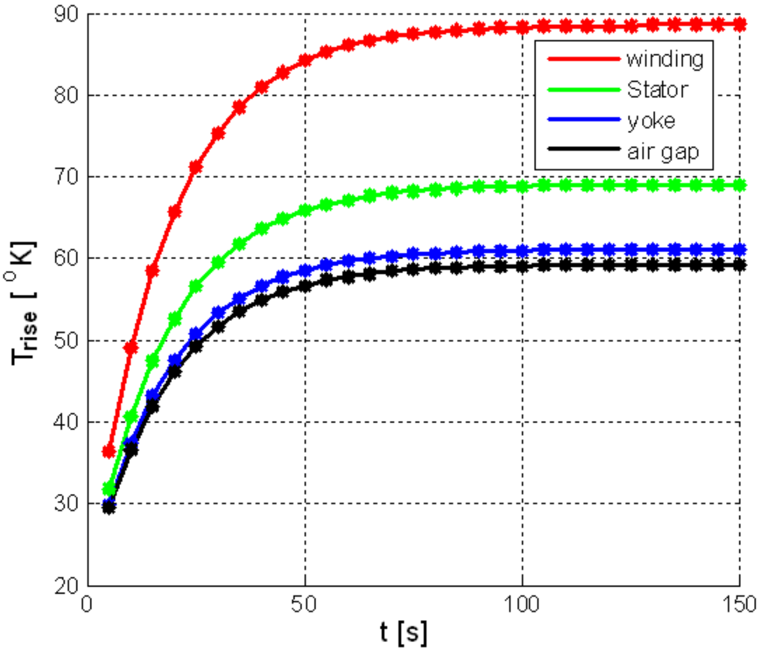

Figure 3.19: Transient temperature time curve

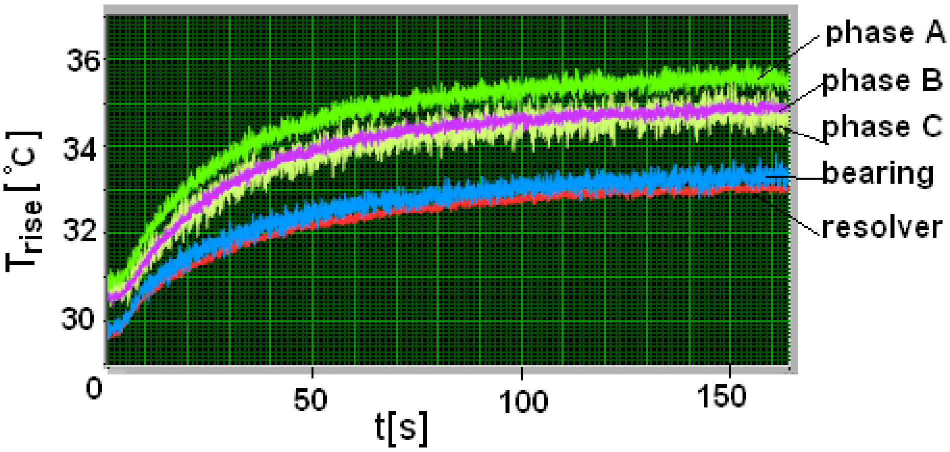

Figure 3.20: Measured temperature rise curve

4 Maximum Torque Control of a High Speed SRMs based on the Acceleration Method

In this chapter, a maximum torque control strategy is implemented by optimizing the turn-on and turn-off angle vs. speed and reference currents. An acceleration test bench of the SR S/G and an additional inertia will be built to investigate the SR S/R torque and speed performance.

Based on this test bench, an indirect torque measurement method is applied to validate the maximized torque values in starting mode and output power in generator mode. In comparison with other articles about indirect torque measurement methods in [82], [83] and [84], there are some advantages in this approach. Firstly, the control strategy could be investigated in wide ranges of speed up to 35,000 rpm and torque to 25 Nm. Secondly, a full range of the average torque and speed can obtained based on extending the whole moment of inertia. Thirdly, a constant acceleration and control speed strategy is applied to constant the SRM torque in starting mode and constant speed at steady state operation.

4.1 Maximum Torque Control Strategies of the Switched Reluctance Starter

In most of the switched reluctance motor applications, maximization of average torque, efficiency, and minimization of torque ripple[1] are three criteria which every optimal control strategy tends to achieve. However, the most important demand on the SR S/G drive system is a maximum average torque in starting mode and a maximum output power in generator mode. Thus, an optimal controller of turn-on and turn-off angles must be applied to achieve the performance.

The average torque depends on the phase torque waveforms which are controlled by the phase currents, turn-on, and turn-off angles as in fig 4.1. The average torque of SRM drives is given by (4.1):

$$T_{avg} = \frac{1}{\tau_{ph}} \cdot \int_{0}^{\tau_{ph}} \sum_{k=1}^{N_{ph}} T_{phk} \cdot dt \tag{4.1}$$

where τ_{ph} denotes the period of the phase current, N_{ph} denotes the number of phases, and T_{phk} denotes the phase torque.

There are some publications about optimal control torque strategies as e. g. [85], [86] and [87].

In those methods, the turn-on angles were fixed independent of speed and the turn-off angles were calculated by an explicit equation with some assumptions such as neglection of phase resistance, iron loss, and linear flux linkage with rotor position. In this thesis, both the turn-on and turn-off angles are variable and pre-determine off-line by numerical means because these angles depend on the speed and current control method[2]. Especially, the torque tends to decrease at high speeds due to non linear magnetic characteristics. Fig 4.2 shows a procedure to get the maximum torque curves and the optimal turn-on and turn-off angles by using the simulation from chapter 2.

Many operation points have been predetermined for a speed range from 0 to 50,000 rpm with steps of 2,500 rpm and for a reference current range from 0 to 300 A with steps of 15 A. With each pair of the speed and current, many combinations of the turn-on angle range θ_{on}[3] and turn-off angle range θ_{off}[4] have been investigated by the SRM simulation[5]. However, only one combination of the turn-on and turn-off angles for which the average torque achieves its maximum can be obtained as shown in fig 4.3.

After investigating the full range of the speeds and currents, the 3D plot of optimal turn-on and turn-off angles vs. reference currents and speeds were determined (fig 4.4). The optimal firing angles [6] have been selected and stored in lookup tables. Those tables will be used in a LabVIEW controller program to maximize the SRM torque later.

---

[1] is defined as the difference between the maximum torque T_{max} and the minimum torque T_{min}

[2] chopping current control or voltage control

[3] [$\theta_{on_{min}}$ -> $\theta_{on_{max}}$], $\theta_{on_{min}}$=-18^o and $\theta_{on_{max}}$=-2^o

[4] [$\theta_{off_{min}}$ -> $\theta_{off_{max}}$], $\theta_{off_{min}}$=25^o and $\theta_{off_{max}}$=45^o

[5] has been simulated in chapter 2

[6] are turn-on and turn-off angles

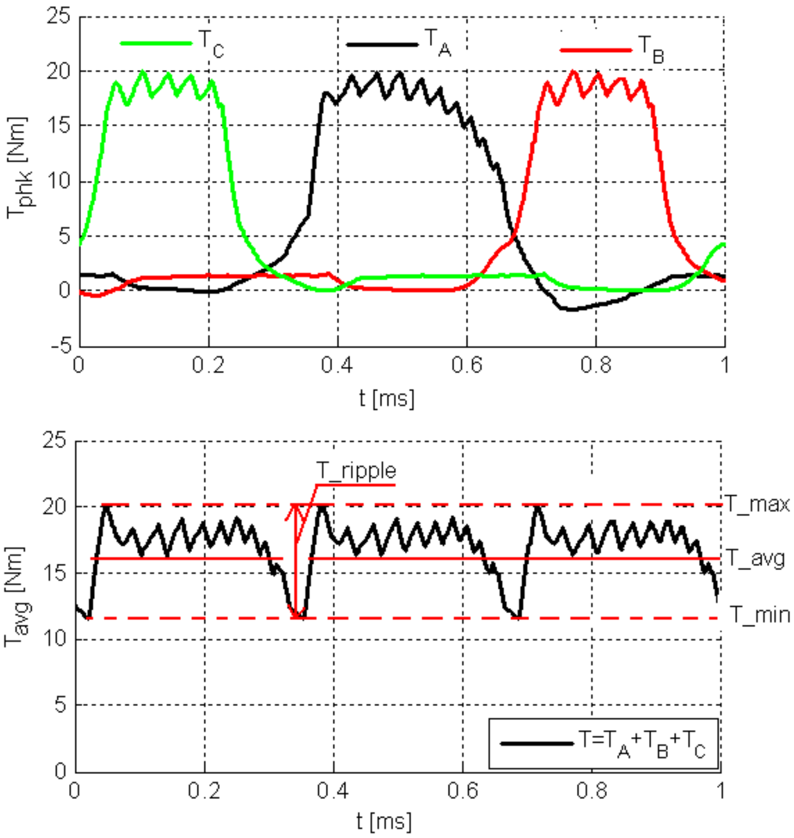

Figure 4.1: Torque waveforms at 15,000 rpm and 200A

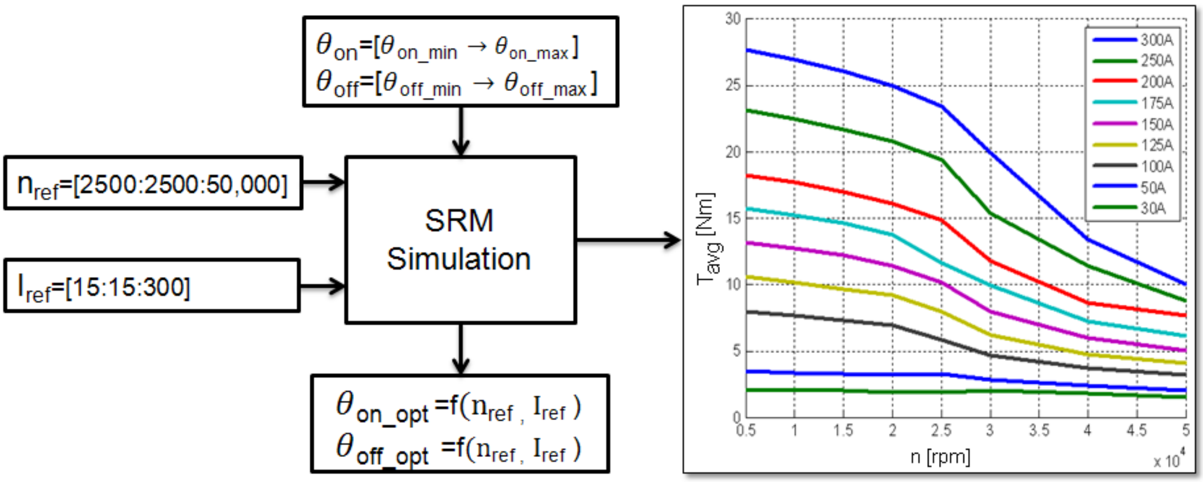

Figure 4.2: Optimal excitation angle control strategy to maximize torque

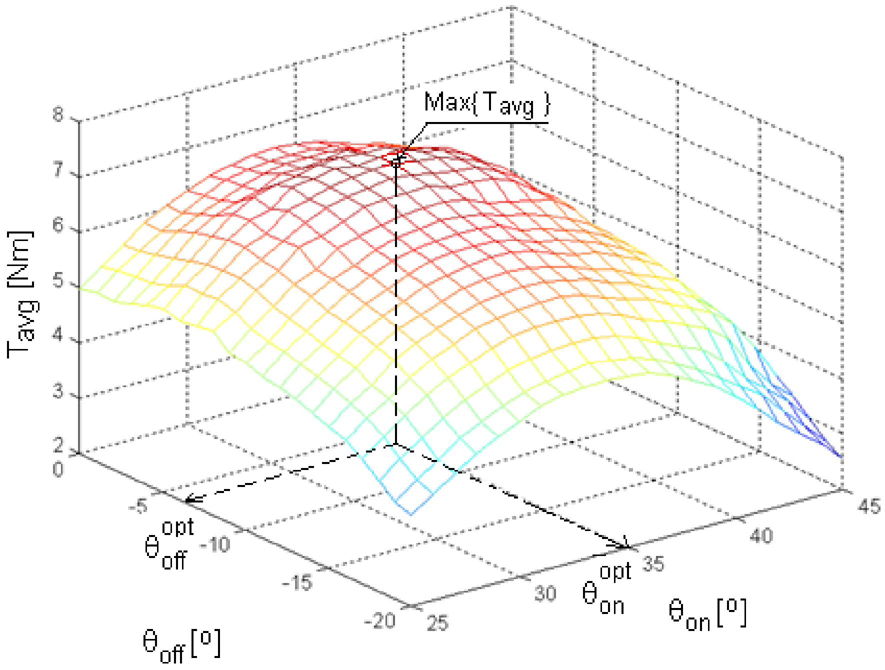

Figure 4.3: Maximum average torque vs. turn-on and turn-off angles

4.2 A High Speed SR S/G with an Additional Inertia Load Drive System

4.2.1 Experimental Setup of the SR S/G Drive System

To realize the maximum torque control strategy, an experimental setup of the SR S/G drive system was established. In order to extend torque and speed measurement ranges during dynamic operation, the SRM shaft has been coupled directly with an additional rotating mass which increases the total inertia of the whole system. The test bench furthermore consists of SR machine, power electronic inverter, NI-USB-6212 ADC card, R/D board, and current controller (fig 4.5) as described in chapter 2.

4.2.2 Safety Protection Calculation for the Test Bench

In a high speed drive system, the large kinetic energy of the rotating parts may cause damage to the test bench in error conditions. Therefore, a mechanical frame was designed to protect people and material in case of mechanical failures leading to explosion by the centrifugal force.
The dynamic balancing of the whole test bench must be respected because the bearings can only operate with very high balancing level.
The whole experimental setup was covered with a hollow steel frame filled with sand bags.

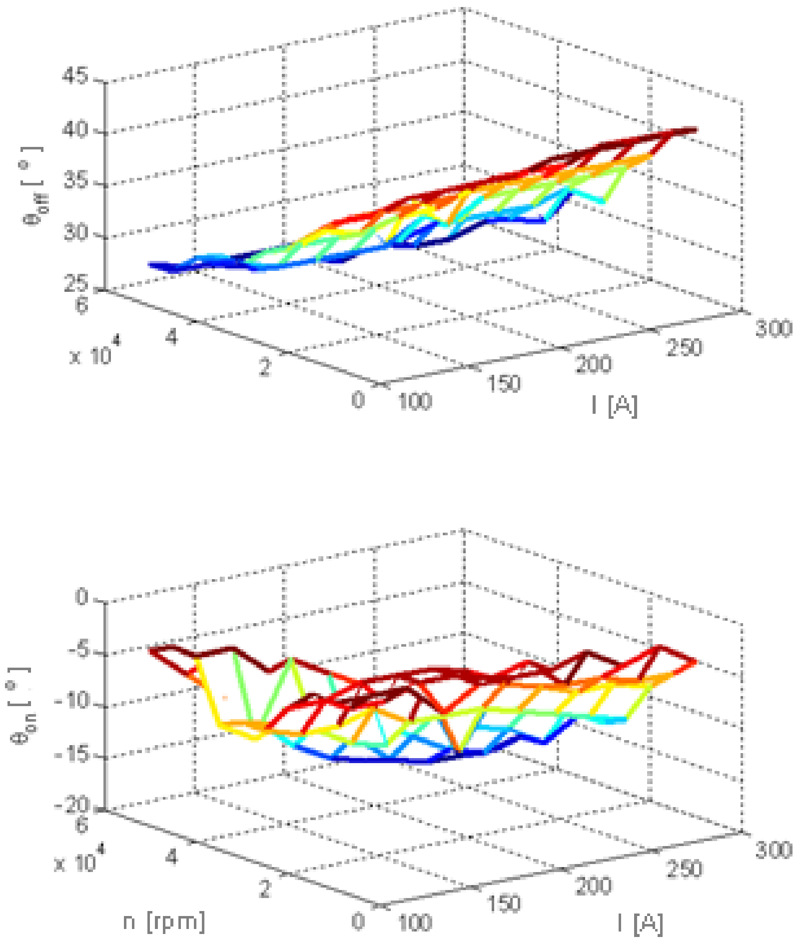

Figure 4.4: Optimal turn-on and turn-off angles vs. speed and current

To guarantee the safety protection, the thickness of the sand bags has been designed so that no rotating parts can get out of the protection cover as shown in fig 4.6.

The mechanical stress of the cylinder caused by the centrifugal force was calculated and compared with the data of the steel S275JR. Fig 4.7 shows a photo of the cylinder as the additional inertia load of the SRM. The dimensions are shown in Table 4.1.

Kinetic Energy Calculation:

An exact knowledge on the kinetic energy of the moving parts is important to design the protection enclosure. The amount of kinetic energy E stored in the cylinder varies linearly with moment of inertia J and with the square of the angular velocity ω. It is calculated as follows:

$$E = J_L \cdot \frac{\omega^2}{2} \tag{4.2}$$

The maximum kinetic energy expected at 50,000 rpm is $E_m = 105$ kJ.

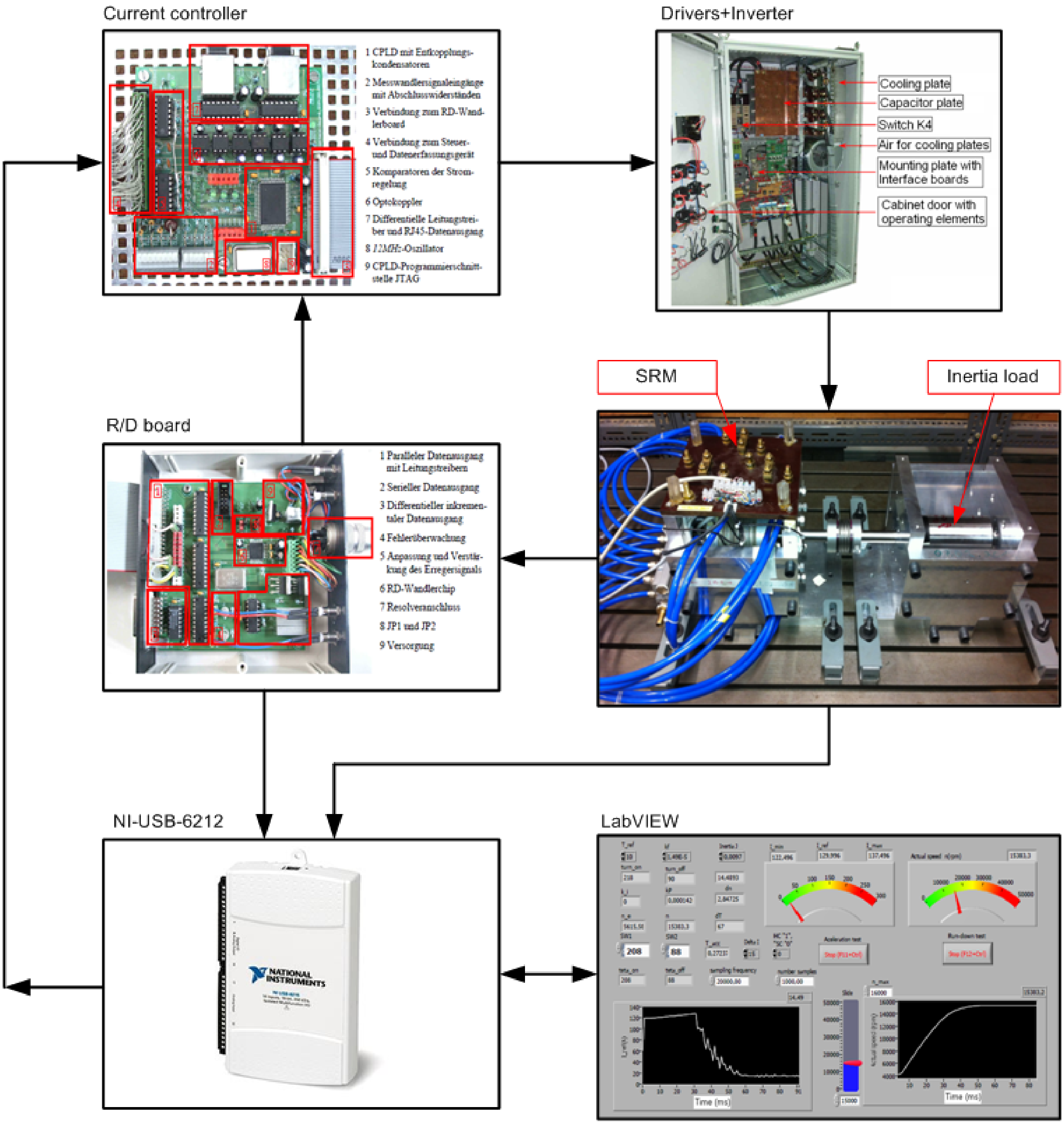

Figure 4.5: Experimental setup of the SR S/G drive system

Table 4.1: Geometry parameters of the steel cylinder (S275JR)

Name	Dimensions	Unit
Length of cylinder	150	mm
Diameter of cylinder	85	mm
Length of shaft	140	mm
Diameter of shaft	24	mm
Mass	7.27	kg
Additional inertia load	$7.7 \cdot 10^{-3}$	kgm^2

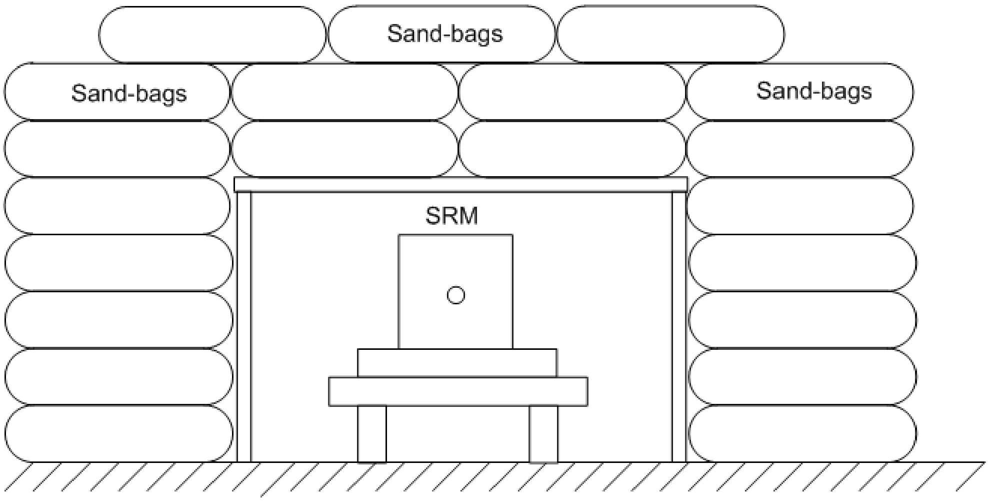

Figure 4.6: Moving protective covers

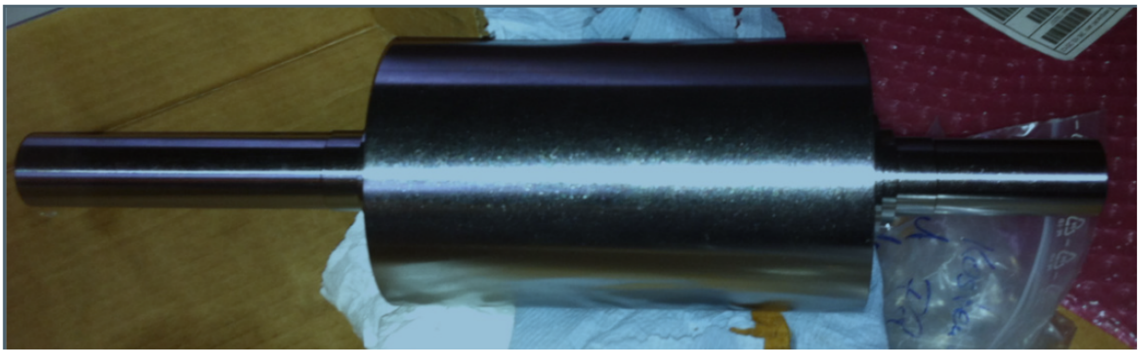

Figure 4.7: Photo of the cylinder

Maximum Velocities of the Rotating Parts:

The dynamic velocity is defined as potential speed of a mechanical part when it separates from the test bench. For the worst case, we assume that the kinetic energy is equal to the dynamic energy of mechanical parts when they are would move away from the test bench. The potential velocity is calculated assuming equality of rotational and translational energy.

$$J_L \cdot \frac{\omega^2}{2} = m \cdot \frac{v_m^2}{2} \tag{4.3}$$

$$v_m = \omega \cdot \sqrt{\frac{J_L}{m}} \tag{4.4}$$

The maximum speed expected is v_m= 170 m/s.

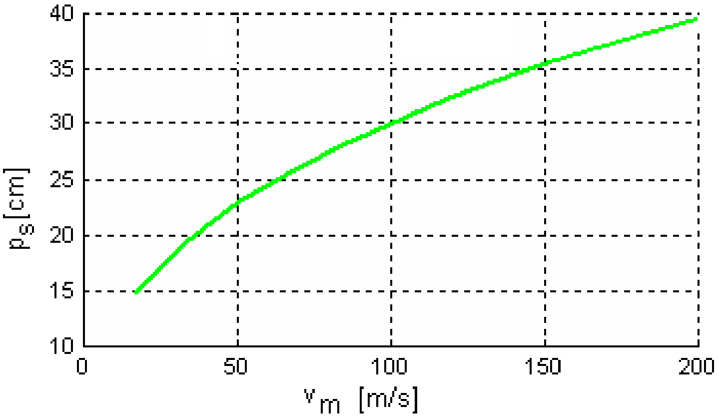

Figure 4.8: Velocity and penetration depth of the inertial load

4.2.3 Protective Construction of Sandbags:

An empirical dependence equation (4.5) to predict the steel penetration depth in to dry sand was introduced in [96] as:

$$p_s = 0.1 \cdot \rho_s \cdot (26.2 \cdot d - \frac{1}{\lambda_s} + 1.75 \cdot l - 5.3) \cdot (v_m/v_{max})^{0.4} \tag{4.5}$$

Where ρ_s is mass density, d is diameter, λ_s=l/d is shape factor, v_m is velocity of the cylinder and v_{max}=1.7 km/s is a maximum velocity.
(4.5) leads to a penetration depth of 37 cm in sand at v_m. The whole test bench therefore was completely covered with a 50 cm sandbag layer.

4.3 Indirect Torque Measurement Method for the High Speed SR S/G Acceleration Test

The most common method for measuring torque-speed characteristics is a direct torque transducer. The direct torque sensor is simple to use and measures the actual torque with time delay of some 10 until 200 ms. For the high speed and acceleration of the SR S/G drive system, the torque and speed differences have to be measured in a short time interval. For example, the time delay of the torque sensor (DL2000-VA-TE-T) in fig 4.9 is 0.18s. With this time delay, it is impossible to get the initial points of torque and speed with the time from zero to 0.18 s. Therefore, the direct method can not be used to measure a dynamic torque at high acceleration rates.

Indirect torque measurement methods have been reported in [82], [83] and [84]. However, there are some drawbacks or limitation in computation precision of torque. A high speed permanent magnet motor has been used for the acceleration method to measure torque with speeds up to 200,000 rpm was reported in [82]. Nevertheless the desired torque values could not be adjusted duly without an additional load.

4.3.1 Torque Measurement of the SR S/G without Additional Load

In a first experiment, the SRM shaft was not connected to any load. Therefore, the total moment of inertia is equal to the one of rotor. The acceleration results from the time derivative of angular speed $d\omega/dt$. With this constant moment of the rotor inertia J_R, a change in average torque will also change the acceleration time. For the high speed drive, the friction and mechanical loss torques are significant and can not be neglected. The total electromagnetic torque T_{sum} can be obtained according to as (4.6):

$$T_{\sum} = J_R \cdot \frac{d\omega}{dt} + T_{mech} = T_R + T_{mech} \tag{4.6}$$

Where J_R=1.5·10^{-3} kgm^2 is the moment of inertia of the rotor, T_R is the accelerating torque by the rotor inertia, and T_{mech} is the torque by friction and mechanical losses. Fig 4.10 shows the calculated torque based on the measured speed curve. The measured and simulated torque curves agree quite well. With a constant value of the rotor inertia, torque and speed ranges can be extended by increasing the reference current. Table 4.2 summarizes some results of the final speeds achieved and the shaft torque values vs. current references. At constant durations of the experiments, the end speed increases with higher current references leading to larger torque values. By supplying higher current values, the noise of speed measurement becomes unbearable for precise measurements. Therefore, the torque and speed extension by applying an additional inertia load is important to improve the precision of the measurement method.

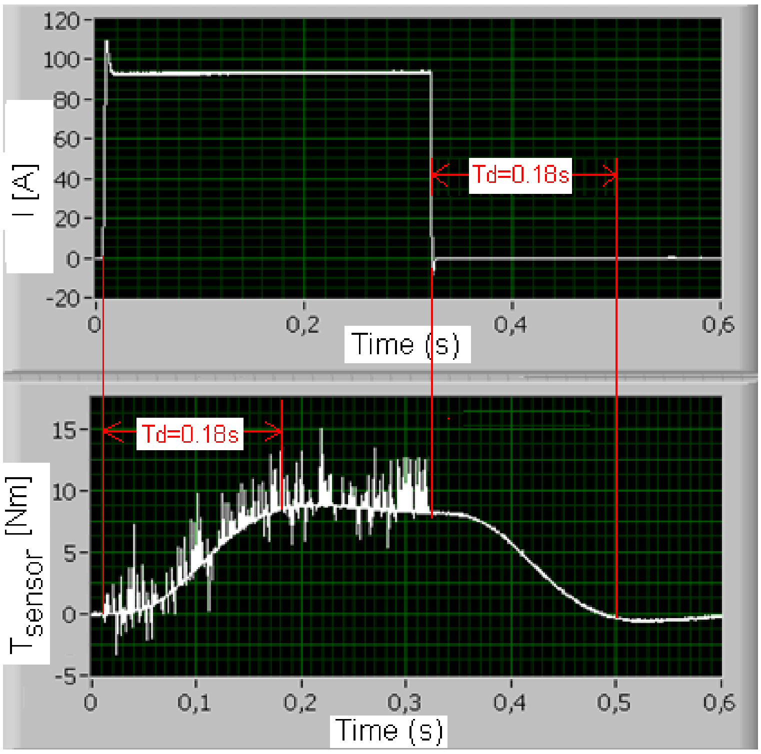

Figure 4.9: The time delay of the torque sensor (DL2000-VA-TE-T, 100 Nm)

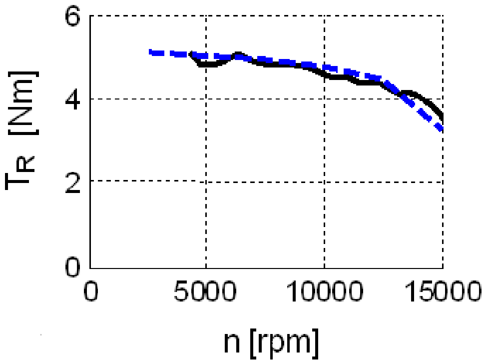

Figure 4.10: Torque measured (line) and simulated (dashed) vs. speeds curves based on the SRM rotor inertia

Table 4.2: The calculated torque of the moment of rotor inertia in acceleration tests

Δ t[s]	n [rpm]	I_{ref} [A]	U[V]	P [W]	T_R [Nm]
0.5	8,500	70	180	3,955	2.8
0.5	10,500	80	180	5,579	3.3
0.5	13,500	90	179	8,354	4.2
0.5	15,000	100	178	8,916	4.6

4.3.2 Polynomial Curve Fitting Method for the Speed and Torque calculation

Due to the speed measured in a short time interval, some noise of the speed derivative of time $d\omega/\mathrm{dt}$ calculation can not be neglected. Therefore, the recorded data are not suitable to calculate and analyze immediately. Hence, they must be converted or smoothed by a polynomial curve fitting method. A polynomial curve fitting method has been used to obtain the speed and torque curves. Curve fitting method is the process of constructing a curve, or mathematical function fit to a series of data points. The MatLab function polyfit was used to construct the speed and torque curves as follows:

$$p = polyfit(t,n,h) \tag{4.7}$$

with p being a row vector of the length n+1 containing the polynomial coefficients of degree h, t being the measured time, and n being the measured speed...

$$n_{fit} = p_1 \cdot n^h + p_2 \cdot n^{h-1} + .. + p_h \cdot n + p_{h+1}; \tag{4.8}$$

Fig 4.11 shows the smoothed torque vs. speed curves. The polynomial order was determined after comparing the error with different orders.

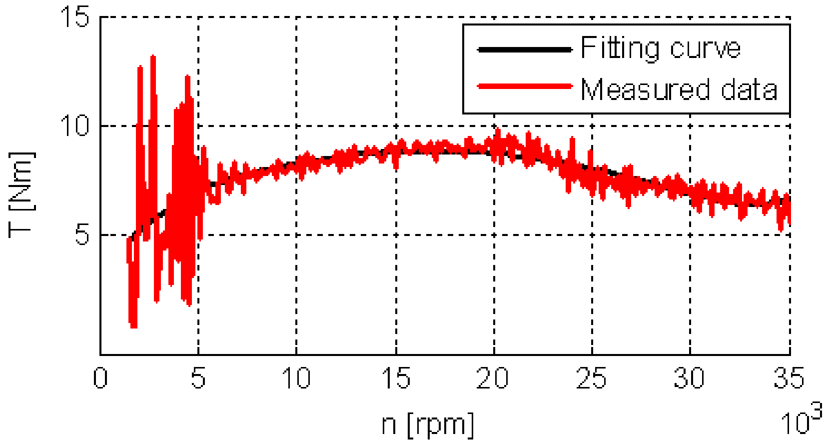

Figure 4.11: Speed and torque calculation by a polynomial curve fitting

4.3.3 Rotor Speed Measurement

In steady state operation, the rotor speed can be measured by counting the number of a digital pulse in a period of time. For the acceleration test, the speed increases rapidly. Therefore, the rotor speed is calculated based on the frequency of the least significant bit of the R/D converter (DB9) in fig 4.12. The number of the DB9 pulse for one rotor cycle is equal the rotor teeth (N_R). The SRM speed is calculated as:

$$n(rpm) = \frac{60}{N_R} \cdot \frac{1}{T_{DB9}(s)} = \frac{60}{N_R} \cdot f_{BD9} = \frac{60}{4} \cdot \frac{1}{0.017(s)} = 882(rpm) \tag{4.9}$$

with $f_{DB9}=\frac{1}{T_{DB9}}$ being the frequency of the digital bit to measure the speed.

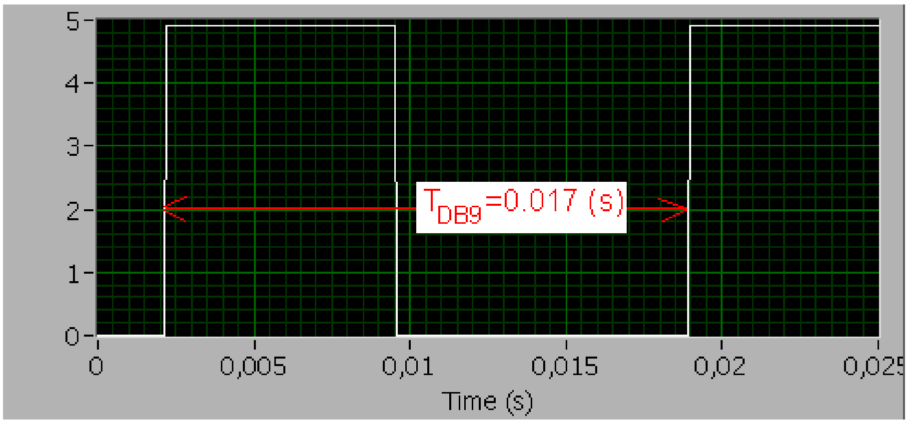

Figure 4.12: Output waveform of the the digital bit from the R/D board

4.4 Torque Maximization of the SR S/G with an Additional Inertia Load

To investigate the full range of torque and speed, an additional moment of inertia load is required to extend duration time of acceleration. An inertia load with a cylinder shape has been coupled to the rotor shaft. The whole moment of inertia of all rotating parts equals the sum of moment of inertia of the rotor and identical flywheel according to (4.10).

$$J_{\sum} = J_R + J_L + J_C \tag{4.10}$$

Where J_L is the moment of the additional inertia load and J_C is the moment of the coupling inertia. The shaft torque is calculated according to (4.11):

$$T = J_{\sum} \cdot \frac{d\omega}{dt} \tag{4.11}$$

To get the full range of torque and speed, the DC link voltage was set to the rated voltage of 270V. The current and firing angle parameters were initialized to achieve the desired torque and speed values.

The speeds vs. time were recorded during the acceleration test. The average torque values were calculated from the measured or fitted speed curves. Fig 4.13 shows the torque results from the fitted speed curve and from measured speed. The fitted torque curve is close to the torque curve calculated from measured speed data.

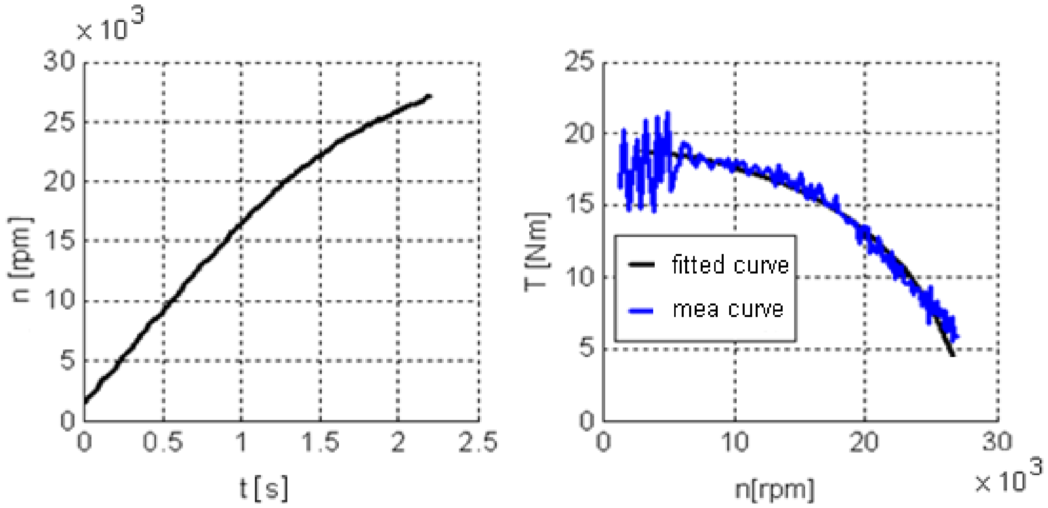

Figure 4.13: Torque calculation based on fitted curve and measured data with an additional moment of inertia load

4.4.1 PI Speed Controller

To maximize the average torque at starting state and keep the speed constant value at steady state, PI speed control loop has been implemented to meet the desired torque and speed performance. The speed control system can be characterized by the following mathematical equations (4.12-4.13)

$$\frac{d\omega}{dt} = \frac{1}{J_{\sum}} \cdot \left(T_{\sum} - \Delta T - k_{fr} \cdot \omega^2 - T_{loss}(\omega)\right) \tag{4.12}$$

$$\frac{d\theta}{dt} = \omega \tag{4.13}$$

where $T_{\sum}$ is the electromagnetic torque, ΔT is the reference torque output from PI speed controller, $k_{fr} \cdot \omega^2$ is the air friction loss torque of both rotor and additional load inertia which has been determined by the rundown test, and $T_{loss}(\omega)$ is the torque by additional losses such as the bearing loss and unpredictable losses. This loss is a function of rotor speed.
The mechanical torque equation of a SRM drive is considered as follows:

$$T_{\sum} = J_{\sum} \cdot \frac{d\omega}{dt} + \Delta T + k_{fr} \cdot \omega^2 + T_{loss}(\omega) \tag{4.14}$$

When the SRM operates in steady state mode at constant speed ω without load, $\Delta\omega$ is zero and the acceleration torque $J_{\sum} \cdot \frac{d\omega}{dt}$ and the error torque ΔT can be removed from (4.14)

$$T_{\sum} = k_{fr} \cdot \omega^2 + T_{loss}(\omega) \tag{4.15}$$

The PI controller is a good choice for the speed performance being suitable for the acceleration test. The torque reference value is calculated by (4.16)

$$\Delta T = (K_p + \frac{K_i}{s}) \cdot \Delta\omega \tag{4.16}$$

where K_p and K_i are the proportional and integral parameters. Those parameters have been calculated based on the rising time and settling time of the speed curves. Practically, the SRM has been tested with different currents to achieve the torque and speed curves. The speed error $\Delta\omega$ and torque reference ΔT inferred from those curves were used to calculate the K_p and K_i factors.

Finally, the desired electromagnetic torque output from the speed controller $T_{\sum}$ including pilot control values for friction, loss, and additional inertia torque calculates as follows $T_{\sum}$ (4.17):

$$T_{\sum} = \left(K_p \cdot \Delta\omega + K_i \int_0^t \Delta\omega \cdot dt \right) + k_{fr} \cdot \omega^2 + T_{loss}(\omega) + J_{\sum} \cdot \frac{d\omega}{dt} \tag{4.17}$$

Fig 4.14 shows the PI speed controller for the SR S/G drive system. Firstly, the speed error $\Delta\omega$ is produced from the comparison between the reference and the actual speeds. The reference current is interpolated from the desired electromagnetic torque based on a 2D lookup table depending on the actual speed and the torque limitation T_{max}.

The T_{max} limit ensures that the reference currents do not exceed the maximum IGBT current. The current values are controlled by the hysteresis current controllers. The switching on and off signals of the IGBTs are determined by comparing the actual rotor position with the turn-on and turn-off angles.

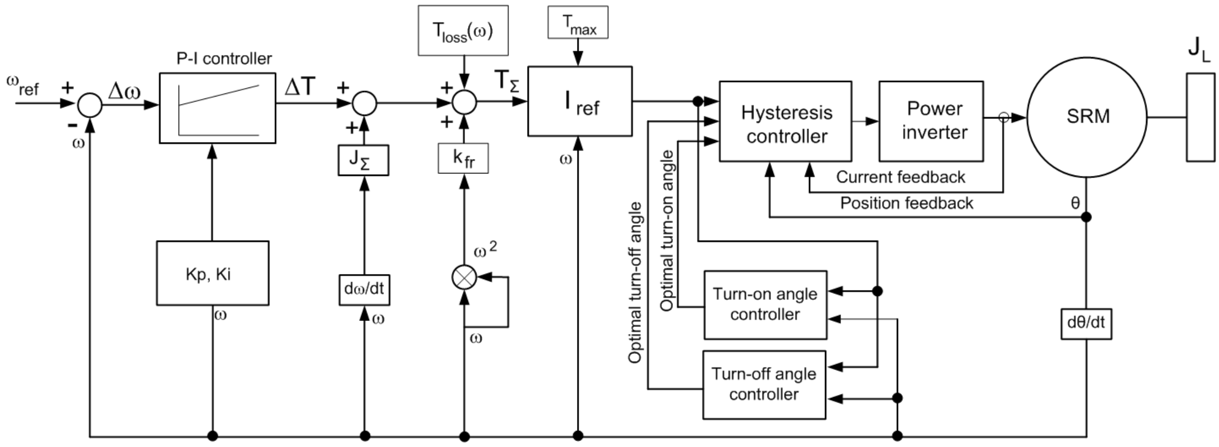

Figure 4.14: Torque and speed control block diagram

4.4.2 Constant Acceleration and Speed Control Strategies for the Torque Measurement

To get high torque values in the full speed range, the acceleration is kept constant. This may lead to an overspeed error. Thus, an optimal strategy for constant acceleration and speed control is necessary for the acceleration test. Three possible strategies are also discussed and analyzed below:

Speed Control Method

When the SRM is regulated by a speed controller, the speed curve is a roughly parabolic function. The speed rises to the desired value until the changing rate of the speed is reduced to zero at top speed. Fig 4.15 (a) illustrates the calculated torque results. The torque tends to reduce with increasing speed. A big drawback is that the SRM can not keep a high torque in a full range of speed.

Constant Acceleration Method

The purpose of the this method is to increase the speed with a constant acceleration until the rotor speed exceeds a limited value by separating the SRM from the power inverter, see fig 4.15(b). The torque is kept a high and constant value in a wide speed range. Due to the delay time in switching off the inverter, the speed may however exceed its limit thus bearing the danger of damage by centrifugal forces.

Combined Constant Acceleration and Control Speed Method

To solve the drawbacks mentioned above, the test consists of both constant acceleration and speed control stages. For speeds below the reference value, the acceleration reference is used: the speed derivative is fed back to the controller input. The speed controller will be applied when the rotor speed exceeds the reference value.
Fig 4.15(c) shows the torque-speed curve measured by the combined constant acceleration and control speed method. The torque curve is flat or quite constant within a speed range from zero to the reference speed. From the reference speed to the speed limit, the torque is reduced in order to control the speed. Based on this novel method for constant acceleration and speed control strategy, the desired torque value can be kept constant in a wide speed range.

Determination of the Torque and Losses in Rundown Testes

From the run down speed curve, the torque caused by friction losses was calculated based on the total moment of inertia of the moving parts and deceleration. They include the friction and additional losses of the SRM rotor and the additional inertia load in fig 4.16.

$$T_{fr} = k_{fr} \cdot \omega^2 \tag{4.18}$$

where k_{fr} =2.17·10^{-8} Nm·s^2·rad^{-2} is the friction loss torque, which can be determined from the torque speed curve in fig 4.16.

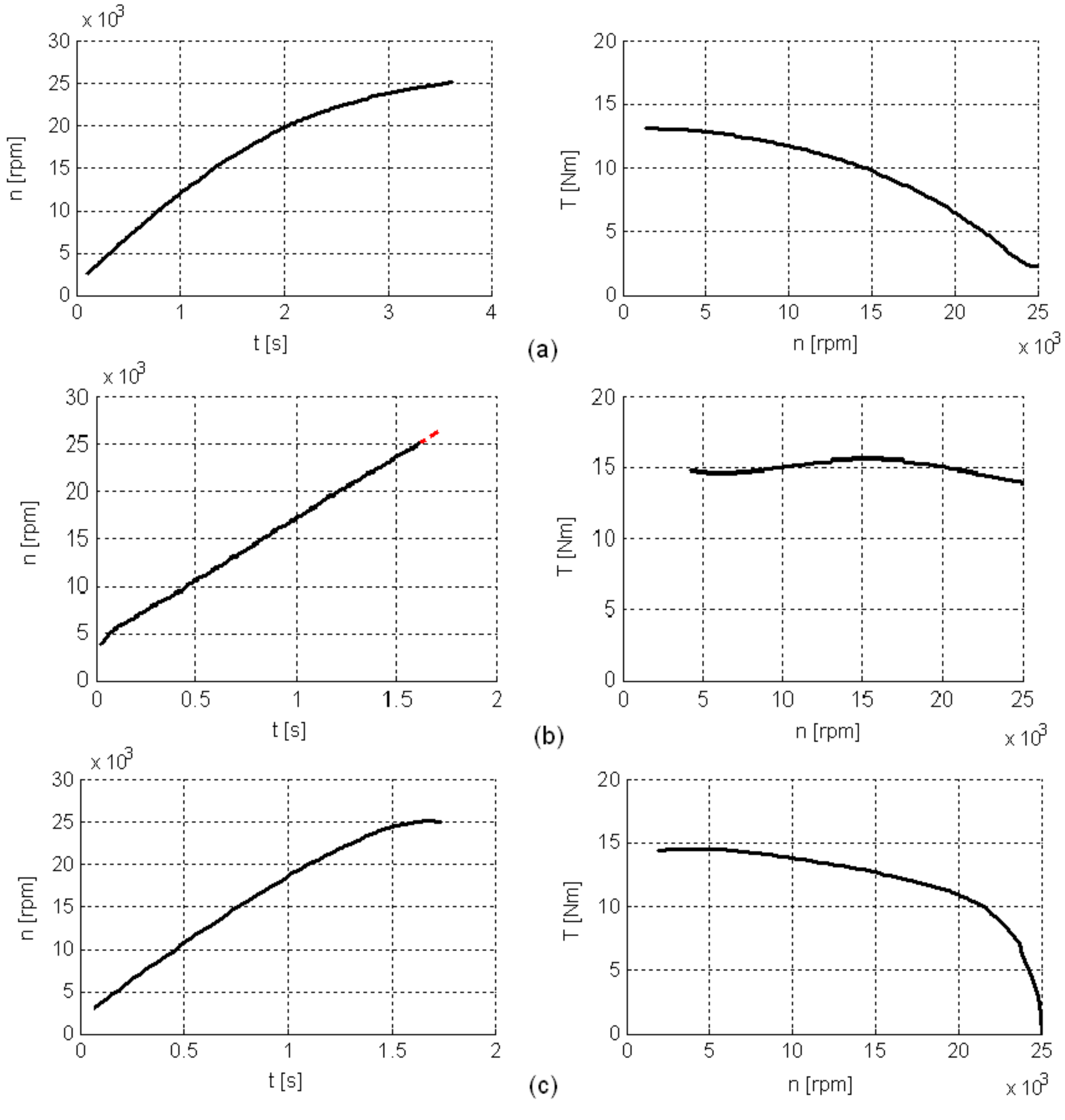

Figure 4.15: Torque and speed curves with the methods of speed control (a), constant acceleration (b), and combined acceleration and speed control (c)

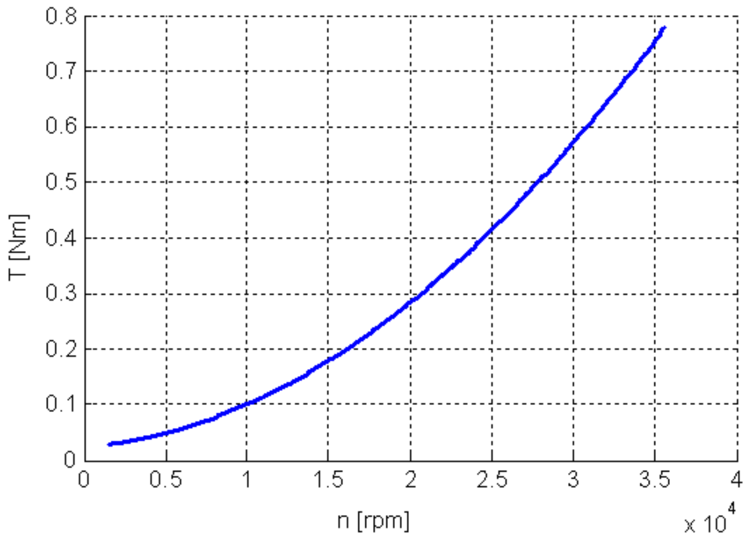

Figure 4.16: Torque of the friction and mechanical losses with additional moment of inertia

4.5 Maximum Torque Verification of the SR S/G in motor operation

The maximum torque and PI speed controllers were implemented in the LabVIEW software. The torque curves were measured in a wide range of speed up to 35,000 rpm. The speed can be also determined by the phase current frequency by an digital oscilloscope.

4.5.1 Torque-Speed Measurement by the R/D board based on LabVIEW

A LabVIEW software was used to measure the rotor speed via the LSB (DB9) of the R/D board. The DB9 output is connected to an analog input channel of the NI-USB-6212. The frequency of the analog channel is calculated in time intervals of 20 ms. The currents and voltages of the phases are also updated by the LabVIEW interface in order to protect the SRM and power inverter from over current or voltage.

Speed range of 27,000 rpm

The speed in starting mode of the SR S/G ranges from 0 to 27,000 rpm. The torques have measured with different reference currents, turn-on, and turn-off angles in this speed range. Fig 4.17 depicts the torque curves with different turn-on and turn-off angles. Each torque-speed curve has a maximum torque point corresponding to a speed. From those points, the maximum torque can be defined. The current is limited to 200A ensuring that the phase currents are still regulated by the chopping mode.

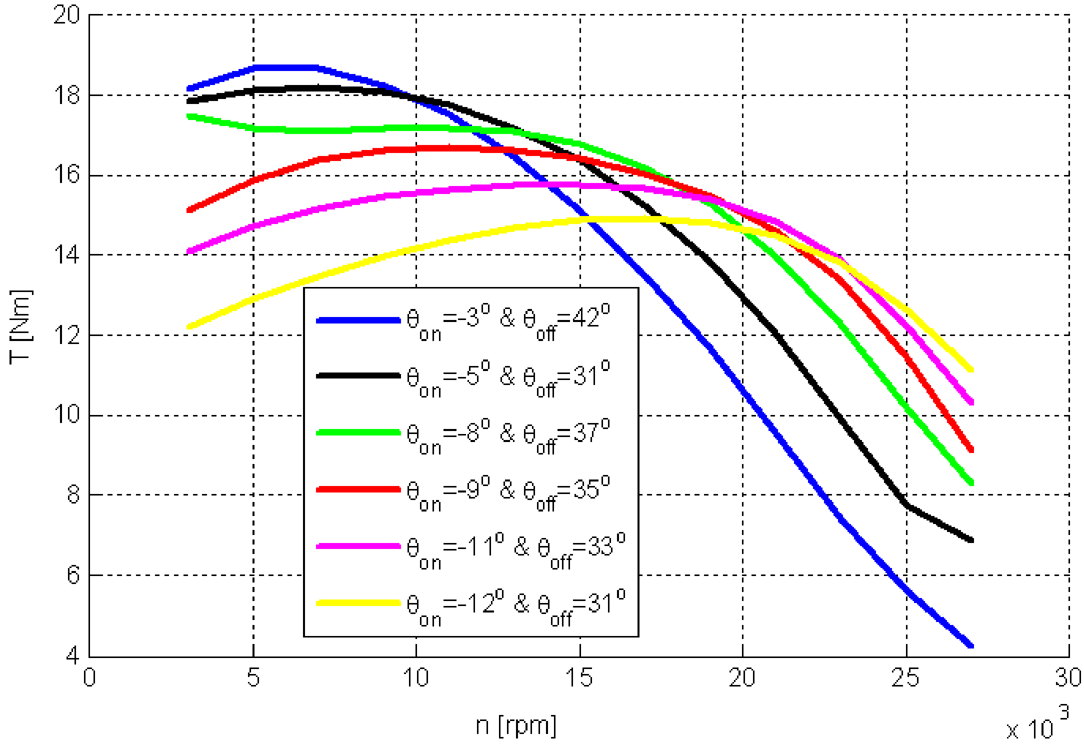

Figure 4.17: Torque speed curves with different turn-on and turn-off angles and I= 200A

Speed range of 35,000 rpm

In order to investigate the current control method in higher speed, the speed during acceleration was also recorded up to 35,000 rpm at a reduced current of 150A.
An increase in current reference will not lead to higher torque at elevated speed, since the current limit will not be reached then. Therefore, in this region the turn-on and turn-off angles become more important.

4.5.2 Torque-Speed Measurement by the Digital Oscilloscope

A digital Oscilloscope DL716 (Module 701855, DC accuracy of 3%) was used to record the phase current waveforms. Since the memory size is limited, the duration time of recorded data depend on the sampling frequency. The torque curves based on the oscilloscope and LabVIEW are in good agreement.

4.5.3 Verification of the Torque Measurement Results

The optimal turn-on and-off angles with the objective of maximum average torque according to chapter 2 were applied. Fig 4.19 depicts the resulting torque speed curve for several reference currents of 150A, 200A, and 250A.
The same optimal turn-on and turn off angles were applied to the both simulation model

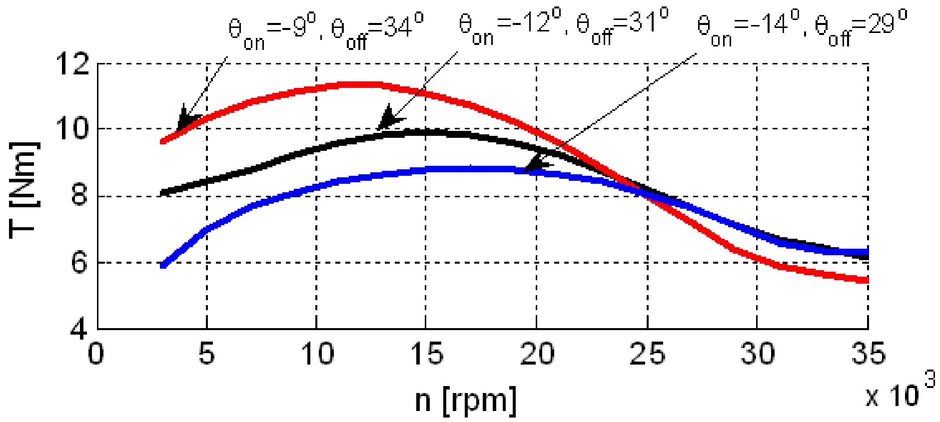

Figure 4.18: Torque vs. speed with 150A

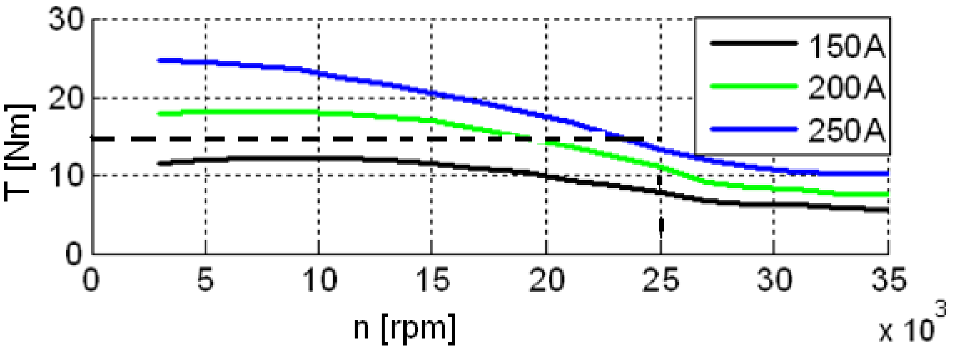

Figure 4.19: Maximum torque values with I=150, 200 and 250A

and experimental test. The results obtained are compared to the dynamic SRM model in table 4.3. The measured and simulated results are in quite good agreement thus validating the simulation. Some minor differences partly come from the curve fitting described before. Other differences are due to the mutual inductance of the connection cables between motor and inverter. The total inductance and the magnetic characteristics change significantly because of the cables of about 15 m length. To solve this problem, a compensation factor can be used to correct the magnetic characteristics. This compensation factor is calculated based on the mutual inductance of the extended cable as given in table 4.4. The additional flux linkage is determined by the product of mutual inductance and phase current.

Table 4.3: Torque results comparison with I=200A

n [rpm]	T_{mea}[Nm]	T_{sim}[Nm]	Difference[%]
5,000	18.62	19.32	3.76
10,000	17.54	18.42	5.10
15,000	16.12	17.18	6.62
20,000	14.80	15.62	5.52
25,000	14.20	15.10	5.96
27,000	10.82	11.61	6.88
35,000	7.72	8.40	7.85

Table 4.4: Mutual Inductance of Extended Cables NSHXAFÖ (1x50 mm^2)

position	L_{SRM} [mH]	L_{Cable} [mH]	L_{Σ} [mH]	Difference [%]
unaligned	0.085	0.002	0.089	2.54
aligned	0.52	0.002	0.524	0.35

4.5.4 Accuracy Determination of the Indirect Torque Measurement

The accuracy of the torque measured is calculated from the measurement of speed and moment of inertia. The speed measurement accuracy depends on the time delay in the R/D board, NI-USB-6212. The whole moment of inertia is based on the moment of the rotor, coupling and additional inertia load. The accuracy can be determined by the precision of speed measurement devices and inertia value calculation:

R/D board

A high speed resolver was used as position sensor. The R/D board converts the secondary voltage of the sin/cos coils to 12 digital bits. One digital bit (DB9) was used to measure the speed. Thus, the time delay of the DB9 has an influence on the precision of speed measurement. According to [46], the delay time was determined 1.33 μs for one rotor tooth revolution. At the maximum speed of 50,000 rpm, the rotor tooth frequency is 3,33 kHz, the rotor speed error can be calculated as:

$$\Delta n = \frac{1.33\mu s}{0.3ms} \cdot 50{,}000rpm = 222rpm \tag{4.19}$$

$$\Delta n(\%) = 100 \cdot \frac{222}{50{,}000} = 0.44(\%) \tag{4.20}$$

NI-USB-6212

According to NI-data-sheet [97], the timing accuracy is ± 50 ppm of the sampling rate of 400kS/s, so the frequency accuracy for this sampling rate is:

$$\Delta f = \pm\frac{50}{10^6} \cdot\ 400{,}000 = \pm 20\text{Hz} \tag{4.21}$$

At the maximum speed 50,000 rpm (f=3.333kHz), the accuracy is:

$$\Delta n(rpm) = \pm\frac{20Hz}{3{,}333Hz} \cdot 50{,}000 = \pm 300(rpm) \tag{4.22}$$

$$\Delta n(\%) = 100 \cdot \frac{300}{50{,}000} = \pm 0.6(\%) \tag{4.23}$$

The SR S/G Test Bench Moment of Inertia

The SR S/G test bench moment of inertia is determined by the moment of inertia of the rotor, coupling and additional load. Practically, the moment of inertia value can be validated by the weight measurement method. The mass and moment of inertia of the rotor, coupling and additional load have been calculated by FEMM software. The measured and simulated weight results were compared to define the accuracy of the inertia value. For example, fig 4.20 shows. The difference was determined as 1.34 %. Since the mass is proportional to r^2, the inertia precision may be assumed better than 2·1.34 %= 2.68 %.
Since the coincidence was satisfactory, an additional pendulum test was not carried out.

Precision of the Torque Measurement

The accuracy of the torque measurement results from the precision of the measurement devices and the inertia value. The precisions of the different items are listed in table 4.5. There are some minor additional factors which are not predict such as moment of inertia of the bearings and unbalanced mechanical parts.

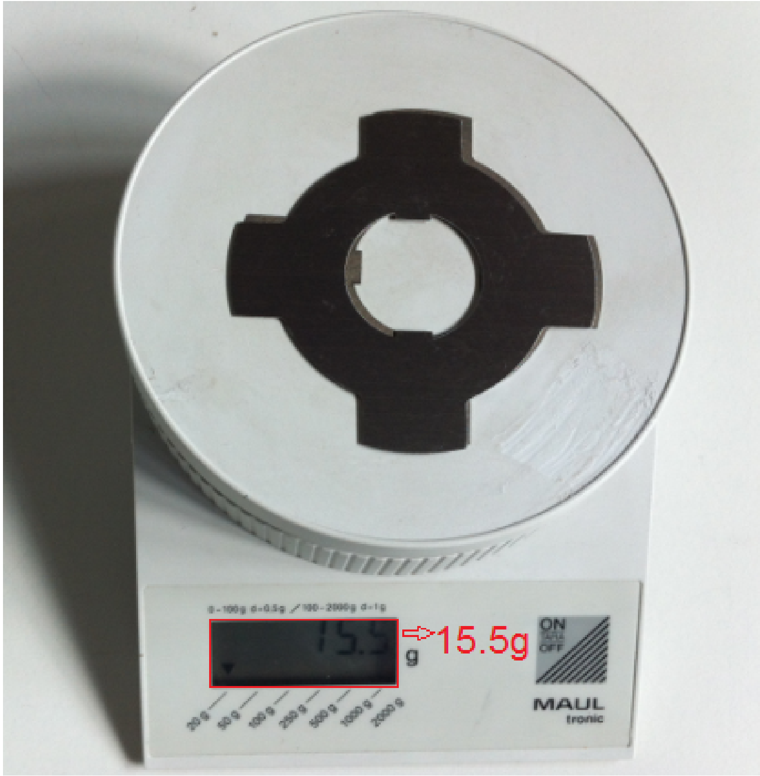

Figure 4.20: Lamination weight measurement

Table 4.5: Accuracy of the SR S/G torque measurement system

Accuracy in	[%]
R/D board	0.44
NI-USB-6212	1.2
Rotor	2.68
Coupling	2·0.2
Cylinder	2·0.8
Total	6.32

4.6 Output Power Validation of the SR Generator Performance

The SR S/G drive system can operate as motor or generator. In order to investigate the SR Generator performance, the output power has been measured in a deceleration test, in which the kinetic energy of the inertia load is converted to electric power. The SR S/G power has been measured by the DC link voltage and current sensors.

4.6.1 Output Power based on the Deceleration Test

The SRM speed was accelerated to 35,000 rpm. Torque and speed were measured and stored. Then, the SRM speed was reduced from 35,000 rpm to 25,000 rpm still recording to the data files. Afterwards, torque and power vs. speed curves were plotted as shown e.g. in fig 4.21.

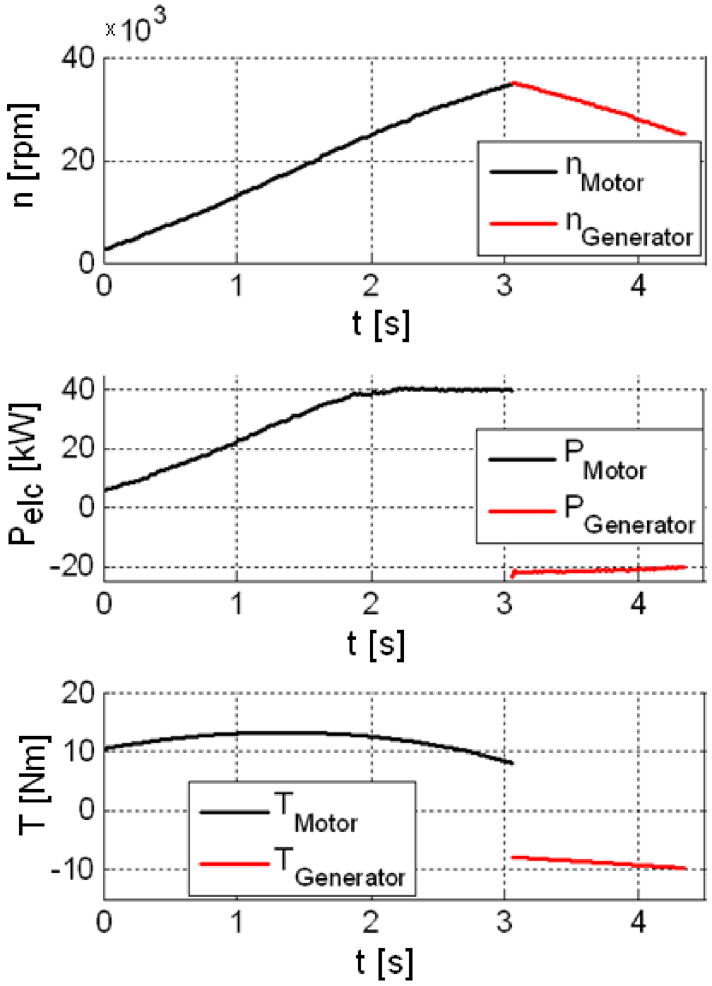

Figure 4.21: Motor and generator performance of the SR S/G

4.6.2 Validation of the SR Generator Performances

The torque and power results measured by the acceleration and deceleration tests have been compared with the performance requirements on the SR S/G drive system as depicted in fig 4.22. The torque curves were considered in starting mode while the power curves were investigated in generator mode.

The measured torque and power results are lower than required. The main reason given by manufacturing problems concerning the air gap length has been published before. The reduction of generating torque obviously exceeds the one of motoring torque.

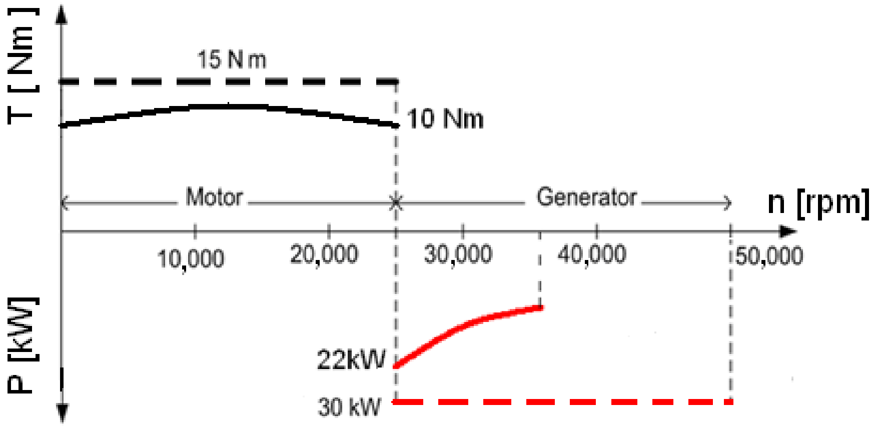

Figure 4.22: The SR S/G torque and power curves (dashed: requirement and line: measurement)

4.7 Summary

This chapter includes some important results about the maximum torque control of the SR S/G drive system as follows:

- The maximum torque control strategy for the high speed SR S/G drive system has been implemented and validated by acceleration tests.
- A novel acceleration and speed control strategy has been investigated for the indirect torque measurement method.
- The torque and output power of the SR S/G have been validated experimentally and the accuracy of the measurement method was discussed.

5 Conclusion and further work

5.1 Conclusion

This thesis gave a detailed overview of a maximum torque control strategy for the high speed SR S/G drive system used in a More Electric Aircraft. The SR S/G and additional inertia load test bench has been implemented to investigate the wide range of torque and speed by an indirect torque measurement method. The algorithm of the maximum average torque strategy has been validated in starting mode with speeds up to 35,000 rpm. The main work and results of this thesis are summarized as follows:

5.1.1 Determination of the magnetization characteristics

An accurate measurement method has been used to obtain the flux linkage curves. In comparison with conventional methods, the experimental results are not affected by iron losses and saturation. The experimental results confirm a FEA static simulation. The static torque and flux linkage were used to simulate a dynamic SRM model.

5.1.2 Losses and heating

The iron losses at high frequency and flux density has been investigated both by simulation and experiment. A new measurement technique was applied to measure the SRM core losses. This method allows a detailed analysis of the core loss rates in predefined rotor and stator parts characterized by constant flux density.
The temperature distribution has been investigated by 3D and 2D FEA models and the fluid velocity distribution in the stator jackets was simulated by a CFD model. The influence of the flow rate of the liquid stator cooling on the temperature distribution was calculated and discussed.

5.1.3 Maximum torque control strategy validation

Based on a novel method for constant acceleration and speed control strategy, the mechanical torque value can be kept constant in a wide speed range. This method was used to validate the torque and power performance in both starting and generator modes. The torque was measured speed up 35,000 rpm and the output power was investigated in between 25,000 and 35,000 rpm.

5.2 Potential Further Work

To investigate the torque control of the switched reluctance motor and the output power of the switched reluctance generator at a full load also for higher speeds from 27,000 to 50,000 rpm, a back to back experimental setup of SR Starter and Generator is suggested including a torque transducer. Such a test system will also allow the verification of the thermal behavior of the machines.

A Abbreviations

CFD	Computational Fluid Dynamics
CCM	Continuous Conduction Mode
CAD	Computer-aided design
CPLD	Complex Programmable Logic Device
DOF	Degrees of Freedom
DCM	Discontinuous Conduction Mode
DAQ	Data Acquisition Device
DB9	Digital Bit 9
FEA	Finite Element Analysis
FEM	Finite Element Method
FEMM	Finite Element Method Magnetics
FFT	Fast Fourier Transform
FTBL	Radial Force Lookup Table
ITBL	Current Lookup Table Blocks
IGBT	Insulated-gate bipolar transistor
kS/s	kilo Samples per second
LUT	Lookup Table
MEA	More Electric Aircraft
M/AEA	More/All Electric Aircraft
NI-USB	National Instrument-USB
PC-SRD	Personal Computer-Switched Reluctance Machine
R/D	Resolver/Digital
SR S/G	Switched Reluctance Starter/Generator
SRM	Switched Reluctance Machine
SDOF	Single Degree of Freedom
TTBL	Torque Lookup Table Blocks

B Symbols

Latin Symbols

A_{ST}	m^2	cross-sectional area of stator tooth
A_{RT}	m^2	cross-sectional area of rotor tooth
A_{SY}	m^2	cross-sectional area of stator yoke
A_{RY}	m^2	cross-sectional area of rotor yoke
A_g	m^2	cross-sectional area of air gap
B_{ST}	T	flux density of stator teeth
B_{RT}	T	flux density of rotor teeth
B_{SY}	T	flux density of stator yoke
B_{RY}	T	flux density of rotor yoke
B_r	T	flux density of air gap
c	$\frac{\mathrm{m}}{\mathrm{s}}$	traveling speed of sound
d_s	m	length of stator teeth
d_s	m	length of rotor teeth
E	J	kinetic energy
e	V	back-emf
F		force vector
F_t	$\frac{\mathrm{N}}{\mathrm{m}^2}$	tangential force density
F_r	$\frac{\mathrm{N}}{\mathrm{m}^2}$	radial force density
g	m	air gap length
H	$\frac{\mathrm{A}}{\mathrm{m}}$	magnetic field
H_s	$\frac{\mathrm{A}}{\mathrm{m}}$	magnetic field of stator
H_r	$\frac{\mathrm{A}}{\mathrm{m}}$	magnetic field of rotor
H_{sy}	$\frac{\mathrm{A}}{\mathrm{m}}$	magnetic field of stator yoke
H_{ry}	$\frac{\mathrm{A}}{\mathrm{m}}$	magnetic field of rotor yoke
H_s	$\frac{\mathrm{A}}{\mathrm{m}}$	magnetic field of air gap
I	A	phase current
I_r	A	rising phase current
I_f	A	falling phase current
I_μ	A	magnetizing current
I_{DC}	A	DC current
J	$\frac{\mathrm{A}}{\mathrm{m}^2}$	current density
J_R	$\mathrm{kg\,m}^2$	moment of the rotor inertia
J_L	$\mathrm{kg\,m}^2$	moment of the inertia load
J_C	$\mathrm{kg\,m}^2$	moment of the coupling inertia
$J_{\sum}$	$\mathrm{kg\,m}^2$	total moment of the rotor inertia
k_{fr}		friction loss factor

k_{SP}		iron loss ratio of stator pole and SRM
k_{RP}		iron loss ratio of rotor pole and SRM
k_{RY}		iron loss ratio of rotor yoke and SRM
k_{SY}		iron loss ratio of stator yoke and SRM
l_{stk}	m	stator stack length
L	H	phase inductance
L_u	H	unaligned inductance
L_a	H	aligned inductance
l_{ST}	m	length of stator
l_{RT}	m	length of rotor
l_{SY}	m	length of stator yoke
l_{RY}	m	length of rotor yoke
M_{fm}	$\frac{\mathrm{N\,m\,s}}{\mathrm{rad}}$	frictional torque factor
m_{ST}	kg	mass of stator tooth
m_{RT}	kg	mass of rotor tooth
m_{SY}	kg	mass of stator yoke
m_{ST}	kg	mass of rotor yoke
m_{SRM}	kg	mass of SRM
N_S		stator pole number
N_R		rotor pole number
N_{ph}		phase number
N_t		number of turn
p	W	electric power
P_{in}	W	input power
P_{out}	W	output power
P_{mech}	W	mechanical power
$p_{mechanical}$	W	instantaneous mechanical power
$p_{electrical}$	W	instantaneous electrical power
p_{loss}	W	ohmic stator resistance
P_{fr}	W	friction loss
P_{Fe}	W	iron loss
P_{cu}	W	copper loss
Q	$\frac{\mathrm{l}}{\mathrm{s}}$	flow rate
R_{ac}	Ω	actual resistance
R_{ph}	Ω	phase resistance
R_e		Reynolds number
r_s	m	radius of stator
r_r	m	radius of rotor
r_{sh}	m	radius of shaft
Pr		the Prandtl number
T_e	s	the time for energizing
T_d	s	the time for de-energizing
T_{co}	N m	conversion torque
T_{avg}	N m	average torque
T_m	N m	maximum torque
T	N m	electromagnetic torque
T_{in}	K	inlet temperature

T_{out}	K	outlet temperature
T_{mea}	K	torque measurement
T_{sim}	K	torque simulation
t_l	m	lamination thickness
u	V	phase voltage
U_{DC}	V	DC link voltage
v_{av}	$\frac{\mathrm{m}}{\mathrm{s}}$	fluid velocity
v_{gap}	$\frac{\mathrm{m}}{\mathrm{s}}$	air velocity
v_m	$\frac{\mathrm{m}}{\mathrm{s}}$	maximum cylinder velocity
V_{max}	$\frac{\mathrm{m}}{\mathrm{s}}$	maximum velocity
W	J	magnetic energy
W_{co}	J	conversion energy
$W_{unaligned}$	J	unaligned energy
$W_{aligned}$	J	aligned energy
W_t	kg	the total mass of poles, windings and yoke
w_s	m	stator pole width
w_r	m	rotor pole width
y_s	m	stator yoke thickness
y_r	m	rotor yoke thickness

Greek and Other Symbols

β_s	°	stator tooth angle
β_r	°	rotor tooth angle
λ	m	penetration depth of eddy current
λ_s		shape factor
ρ_s	$\frac{\mathrm{kg}}{\mathrm{m}^3}$	sand mass density
Φ	V s	flux
η	%	efficency
Ψ	V s	flux linkage
Ψ_r	V s	rising flux linkage
Ψ_f	V s	fallin flux linkage
ρ_s	$\frac{\mathrm{kg}}{\mathrm{m}^3}$	density of stator material
μ_0	$\frac{\mathrm{V\,s}}{\mathrm{A\,m}}$	magnetic permeability of free space
μ_r		relative magnetic permeability
σ_{rel}		relative sound intensity
γ	°	angle rotor position
δ	m	air gap
ω	$\frac{\mathrm{rad}}{\mathrm{s}}$	angular volocity
θ_r	°	rotor pole overlap angle
θ_{dwell}	°	conduction angle
θ_{on}	°	turn-on angle
θ_{off}	°	turn-off angle

C List of Figures

D List of Tables

E Bibliography

[1] Abdel Hafez, A and Forsyth, A. J. *"A Review of More-Electric Aircraft",* Proceedings of The 13rd international conference on Aerospace Science and Aviation Technology conference, ASAT-13. Cairo, Egypt, May 26-28, 2009.

[2] Ahmed Abdel-Hafez *"Power Generation and Distribution System for a More Electric Aircraft - A Review",* Shaqra University Kingdom of Saudi Arabia.

[3] R. T. Naayagi *"A Review of More Electric Aircraft Technology ",* Energy Efficient Technologies for Sustainability (ICEETS), 2013 International Conference on 10-12 April 2013.

[4] Aircraft electrical power systems- charged with opportunities, Aerospace and Defense Executive briefing of Frost and Sullivan, 24th Nov 2008.

[5] Richard E. Quigley, *"More Electric Aircraft",* Proc. 8th Annual Applied Power Electronics Conference and Exposition, pp. 906-911, March 1993.

[6] M. Rinaldi, S. Jones, *" Aircraft Electrical system architectures to support more electric aircraft",* in Proc. Society of Aerospace Engineers Conference, pp. 10.1-10.7, April 2004.

[7] E.H.J. Pallet, *"Aircraft Electrical Systems",* Longman Scientific and Technical, Third edition,1987.

[8] J.A. Weimer, *" Electric power technology for the more electric aircraft",* in Proc. IEEE Digital Avionics Systems Conference, pp.445-450, October 1993.

[9] J.A. Weimer, *" The role of electrical machines and drivers in the more electric aircraft",* in Proc.IEEE Electrical Machines and Drives Conference, pp. 11-15, June 2003.

[10] Heon-Hyeong Lee, Qi Wang, Se-Joo Kim, Woongchul Choi, and Geun-Ho Lee *"A Simplified Torque Ripple Reduction using the Current Shaping of the Flux Switched Reluctance Motor",* Journal of Magnetics 17(3), 200-205 (2012)

[11] P. Srinivas, P. V.N. Prasad, *"Direct Instantaneous Torque Control of 4 Phase 8/6 Switched Reluctance Motor ",* International Journal of Power Electronics and Drive System (IJPEDS) Vol.1, No.2, December 2011, pp. 121 - 128.

[12] Jones, R. *" The More Electric Aircraft: the past and the future",* in IEE Colloquium on Electrical Machines and Systems for the More Electric Aircraft,(November 1999), pp. 1-4.

[13] Moir, I. *"More-electric aircraft-system considerations",* in IEEE Colloquium on Electrical Machines and Systems for the More Electric Aircraft, 1999, pp. 1-9.

[14] Hoffman, A; Hansen, A. Beach, R.; Plencner, R.; Dengler, R.; Jefferies, K. and Frye, R. *"Advanced secondary power system for transport aircraft",* NASA Technical Paper 2463,May 1985.

[15] E. Richter, *"Switched reluctance machines for high performance operations in a harsh environment-A review paper",* invited paper presented at the Int. Conf. on Electrical Machines (ICEM) 1990, Boston, MA, 1990.

[16] E. Richter et al., *"The integral Start/generator development progress",* in Proc. SAE Aerospace Atlantic 92, Dayton, OH, 1992.

[17] S. R. MacMinn and W. D. Jones,*"A very high speed switched reluctance starter/generator for aircraft engine applications",* in Proc. NAECON' 89, Dayton, OH, May 1989.

[18] S. R. MacMinn and J. W. Sember,*"Control of a switched reluctance aircraft engine starter-generator over a very wide speed range",* in Proc. IECEC'89, vol. I , pp. 631-638.

[19] E. Richter and C. Ferreira,*"Performance Evaluation of a 250 kW Switched Reluctance Starter Generator",* Proc. of the 1995 IEEE-IAS Annual Meeting, pp. 434-440.

[20] Caio A. Ferreira, Stephen R. Jones, William S.Heglund, *" Performance Evaluation of a Switched Reluctance Started Generator System Under Constant Power and Capacitive Type Loads",* Applied Power Electronics Conference and Exposition, 1995. APEC '95. Conference Proceedings 1995., Tenth Annual, Page(s): 416 - 424 vol.1.

[21] Arthur V. Radun, Caio A. Ferreira, and Eike Richter, 1995,*"Two-Channel Switched Reluctance Starter/Generator Results",* IEEE TRANSACTIONS ON INDUSTRY APPLICATIONS, VOL. 34, NO. 5, SEPTEMBER/OCTOBER 1998.

[22] C. A. Ferreira and E. Richter, *"Detailed design of a 250 kW switched reluctance starter/-generator for an aircraft engine",* presented at the SAE Aerospace Atlantic Conf. and Exposition, Dayton, OH, Apr. 20 - 23, 1993, SAE Paper 931389.

[23] A. Radun and E. Richter, *"A detailed power inverter design for a 250 kW switched reluctance aircraft engine starter/generator,"* presented at the SAE Aerospace Atlantic Conf. and Exposition, Dayton, OH, Apr 1993, SAE Paper 931388.

[24] E. Richter et al., *"Initial testing of a 250 kW starter/generator for aircraft applications,"* presented at the 1994 SAE Aerospace Atlantic Conf. and Exposition, Dayton, OH, Apr. 18-22, 1994, Paper 941160.

[25] T.J.E. Miller, *"Switched Reluctance Motors and Their Control",* Magna Physics, 1993.

[26] H.Bausch, H.D Kolletschke., *"A novel polyphase multipole permanent magnet machine for wheel drive application"* ICEM 1984. Lausanne, pp 591-594.

[27] T.J.E. Miller, *"Automation with SPEED Motor Design Software ",* SPEED Laboratory, University of Glasgow, 2007.

[28] P. Andrada, E. Martinez, J.I. Perat, J.A. Sanchez, M. Torrent, *"Experimental determination of magnetization curves of switched reluctance motor",* ICEM 2000, Espoo Finland, pp. 761-765.

[29] Peng Zhang, Pablo A. Cassani, and Sheldon S. Williamson, *"An Accurate Inductance Profile Measurement Technique for Switched Reluctance Machine",* IEEE Trans. Ind. Appl., vol. 57, no. 9, Sep. 2010.

[30] T.J.E. Miller, *"Automation with SPEED Motor Design Software ",* SPEED Laboratory, University of Glasgow, 2007.

[31] J. Corda and S. M. Jamil, *"Experimental determination of equivalent circuit parameters of a tubular switched reluctance machine with solid-steel magnetic core",* IEEE Trans. Ind. Electron., vol. 57, no. 1, pp. 304-310, Jan. 2010.

[32] Thyssen-Krupp Stahl. Datenblatt PowerCore M 270-35 A. MDB - TAB2A.XLS - Version 2.4. September 2005.

[33] Surahammars Bruks AB. Datenblatt SURA M270-35A. www.sura.se. Surahammar (Schweden). Juni 2008.

[34] R. Krishnan, P. Materu, *"Measurement and instrumentation of a switched reluctance motor",* in Proc. Industry Applications Society Annual Meeting, 1-5 Oct. 1989, vol.1, pp. 116-121.

[35] Reinert J, Inderka R, de Donker RW, *"A novel method for the prediction of losses in switched reluctance machines",* EPE'97 1997 ;pp. 3.608-3.611.

[36] Baltazar Parreira, Silviano Rafael, *"Obtaining the Magnetic Chacteristics of an 8/6 Switched Reluctance Machine: From FEM Analysis to the Experimental Tests",* IEEE Trans. Ind. Electron., vol. 52, No. 6, pp. 1635-1643, December. 2005.

[37] R. Gobbi, N.C. Sahoo, R. Vejian Rajandran,*"Rising and Falling Current Methods for Measurement of Flux-Linkage Characteristics of Switched Reluctance Motors: A Comparative Study",* in Proc. IEEE International Conference on Power and Energy (PECon), 28-29 Nov. 2006, pp. 383-387.

[38] J. Reinert, R. Inderka, M. Menne, and R. W. D. Doncker ,*"Optimizing performance in switched reluctance drives ",* IEEE Ind. Applicat. Mag., Vol. 6, pp. 63-70, July/Aug. 2000.

[39] K. M. Rahman, and S. E. Schulz, *" High-Performance fully digital switched reluctance motor controller for vehicle propulsion ",* IEEE Trans. Ind. Applicat., Vol. 38 (4), pp. 1062-1071, Jul./Aug. 2002.

[40] H. Hannoun, M. Hilairet, and C. Marchand, *"Design of an SRM speed control strategy for a wide range of operating speeds",* IEEE Trans. Ind. Electron., vol. 57, no. 9, pp. 2911-2921, Sep. 2010.

[41] M. Rekik, M. Besbes, C. Marchand, B. Multon, S. Loudot, and D. Lhotellier, *"High-speed-range enhancement of switched reluctance motor with continuous mode for automotive applications",* Eur. Trans.Elect. Power, vol. 18, no. 7, pp. 674-693, Oct. 2008.

[42] R. B. Inderka, M. Menne, and R. W. A. A. De Doncker, *"Control of switched reluctance drives for electric vehicle applications",* IEEE Trans. Ind. Electron., vol. 49, no. 1, pp. 48Ű53, Feb. 2002.

[43] Ferreira, C.A.; Jones, S.R.; Heglund, W.S.; Jones, W.D. *"Detailed design of a 30-kW switched reluctance starter/generator system for a gas turbine engine application",* Industry Applications, IEEE Transactions on, vol. 31, no. 3, pp. 553-561 , 1995.

[44] R. T. Naayagi and V. Kamaraj, *"Shape optimization of switched reluctance machine for aerospace applications",* in Proc. 31st IEEE IECON, Nov. 2005, pp. 1748 Ũ 1751.

[45] A. V. Radun, *"High-power density switched reluctance motor drive for aerospace applications",* IEEE Trans. Ind. Appl., vol. 28, no. 1, pp. 113-119, Jan./Feb. 1992.

[46] Stefan Hoffmann, *"Aufbau und Inbetriebnahme eines SR-Flugzeug-Starter- Generatorsystems",* Master's thesis, TU-Berlin, 2010.

[47] Minh Dinh Bui, Stefan Hoffmann, Uwe Schäfer, *"An Accurate Magnetic Characteristics Measurement Method for Switched Reluctance Machines",* ICEMs 2011, Sep. 2011.

[48] Minh Dinh Bui, Uwe Schäfer, *"Core Losses Measurement Technique for High Frequency and Flux Density of Switched Reluctance Machines",* ICEM 2012, Sep. 2012.

[49] Stuart D. Calverley, Geraint W. Jewell1, and Robin J.: Saunders.: *"Prediction and Measurement of Core Losses in a High-Speed Switched-Reluctance Machine",* IEEE Trans. Magn., vol. 41, no. 11 pp. 4288-4298, Nov. 2005.

[50] Materu P.N., Krishnan R.:*"Estimation of switched reluctance motor losses",* IEEE Transactions on Industry Applications 1992; 28(3):668-679.

[51] Hayashi Y., Miller T.J.E.:*"A new approach to calculating core losses in the SRM",* IEEE Transactions on Industrial Applications 1995; 31(5):1039-1045.

[52] Faiz J., Ganji B., Carstensen C. E., De Doncker R.W.:*"Loss prediction in switched reluctance motors using finite element method",* European Transactions on Electrical Power 2008; 19(5): 731-748.

[53] Mthombeni, L.T. Pillay, P.:*"Core losses in motor laminations exposed to high-frequency or nonsinusoidal excitation",* Industry Applications, IEEE Transactions on, On page(s): 1325-1332, Volume: 40 Issue: 5, Sept.-Oct. 2004.

[54] Reinert J., Brockmeyer A., De Doncker R.W.:*"Calculations of losses in ferro- and ferromagnetic materials based on the modified Steinmetz equation",* IEEE Transactions on Industry Applications 2001; 37(5): 1055-1061.

[55] Charton J.T., Corda J., Stephenson J.M., McClelland M.L.:*"Modelling and prediction of iron loss with complex flux waveforms",* IEEE Proceedings-Electric Power Applications 2005; 152(3):862-870.

[56] Raulin V, Radun A, Husain I.:*"Modeling of losses in switched reluctance machines",* IEEE Transactions on Industry Applications 2004; 40(6):1560-1564.

[57] Finite Element Method Magnetics Version 4.2 User's Manual, October 16, 2010.

[58] Vogt, K.: *"Elektrische Maschinen: Berechnung rotierender elektrischer Maschinen",* VEB Verlag Technik, Berlin, 4. Aufl., 1988

[59] M. Torrent, P. Andrada, B. Blanqueť, E. Martinez, J. I. Perat and J. A. Sanchez.:*"Method for estimating core losses in switched reluctance motors",* Euro. Trans. Electr. Power (2010).

[60] Chindurza, David G. Dorrell, Member, IEEE, and C. Cossar.:*"Assessing the Core Losses in Switched Reluctance Machines",* IEEE Trans. Magn., vol. 41, no. 10 pp. 3907-3909, Oct. 2005.

[61] Ion Daniel Ilina, *"Experimental Determination of Moment to Inertia and Mechanical Losses vs. Speed, in Electrical Machines",* International Symposium on Advanced Topics of electrical engneerings, 2011.

[62] P. D. Mellor, D. Roberts, and D. R. Turner, *"Lumped parameter thermal model for electrical machines of TEFC design",* Proc. Inst. Electr. Eng. Electric Power Applications, vol. 138, no. 5, pp. 205-218, Sep. 1991.

[63] F. P. Incropera and D. P. DeWitt, *Fundamentals of Heat and Mass Transfer,* 4th ed. New York: Wiley, 2001.

[64] Y. T. Wei, D. W. Meng, and J. B. Wen, *"The heat transfer in electrical machines",* Beijing: China mechanism publisher, 1998.

[65] David A. Staton and Andrea Cavagnino, *"Convection Heat Transfer and Flow Calculations Suitable for Electric Machines Thermal Models",* IEEE TRANSACTIONS ON INDUSTRIAL ELECTRONICS, VOL. 55, NO. 10, OCTOBER 2008.

[66] V. Gnielinski, *"New equations for heat and mass transfer in turbulent pipe and channel flow",* Int. Chem. Eng., vol. 16, pp. 359-368, 1976.

[67] David A. Howey, Peter R. N. Childs, and Andrew S. Holmes, *"Air-Gap Convection in Rotating Electrical Machines",* IEEE TRANSACTIONS ON INDUSTRIAL ELECTRONICS, VOL. 59, NO. 3, MARCH 2012.

[68] P. K. Vong and D. Rodger, *"Coupled electromagnetic - thermal modeling of electrical machines",* IEEE Trans. Magn., vol. 39, no. 3, pp. 1614-1617, May 2003.

[69] P. D. Mellor, D. Roberts, and D. R. Turner, *"Lumped parameter thermal model for electrical machines of TEFC design",* Proc. Inst. Electr. Eng.-Electric Power Applications, vol. 138, no. 5, pp. 205-218, Sep. 1991.

[70] David A. Howey, Peter R. N. Childs, and Andrew S. Holmes, *"Air-Gap Convection in Rotating Electrical Machines",* IEEE TRANSACTIONS ON INDUSTRIAL ELECTRONICS, VOL. 59, NO. 3, MARCH 2012.

[71] Song Shoujun, Liu Weiguo, Uwe Schaefer, *"Thermal Analysis of a 30kW Switched Reluctance Starter/Generator System Used in Aircraft",* POWERENG 2009, Lisbon, Portugal, March 18-20, 2009.

[72] Song Shoujun, Liu Weiguo, Uwe Schaefer, *"Detailed design of a 30kW switched reluctance starter/generator system used in more/all electric aircraft",* PhD thesis, Berlin 2009.

[73] JinXin. Fan Student Member, IEEE, ChengNing. Zhang, ZhiFu. Wang , E. G. Strangas, *"Thermal analysis of permanent magnet for electric vehicle application considering driving duty cycle",* IEEE Trans. Magn., vol. 46, no.6, pp. Jun 2010

[74] Devdatta P. Kulkarni, Gabriel Rupertus, and Edward Chen, *"Experimental Investigation of Contact Resistance for Water Cooled Jacket for Electric Motors and Generators"*, IEEE TRANSACTIONS ON ENERGY CONVERSION, VOL. 27, NO. 1, MARCH 2012.

[75] David A. Staton and Andrea Cavagnino, Member, IEEE, *"Convection Heat Transfer and Flow Calculations Suitable for Electric Machines Thermal Models "*, IEEE TRANSACTIONS ON INDUSTRIAL ELECTRONICS, VOL. 55, NO. 10, OCTOBER 2008.

[76] E. Annie Elisabeth Jebaseeli and S. Paramasivam *"Steady State and Transient Thermal Analysis of Switched Reluctance Machine"*, International Journal of Computer and Electrical Engineering, Vol. 4, No. 5, October 2012.

[77] Yunkai Huang, Jianguo Zhu, Youguang Guo, and Qiansheng Hu, *"Core Loss and Thermal Behavior of High-Speed SMC Motor Based on 3- FEA"*, IEEE Transactions on Industry Applications 2007.

[78] LI Cuiping, PEI Yulong, NI Ronggang, CHENG Shukang, *"Analysis of 3D static temperature field of water cooling induction motor in mini electric vehicle"*, Electrical Machines and Systems (ICEMS), 2011 International Conference on. IEEE, 2011.

[79] Staton D, Boglietti A, Cavagnino A, *" Solving the More Difficult Aspects of Electric Motor Thermal Analysis in Small and Medium Size Industrial Induction Motors"*, IEEE Transactions on Energy Conversion, 2005, 20(3):620-628.

[80] Jawad Faiz, Babak Ganji, Christian E. Carstensen, Knut A. Kasper, and Rik W. De Doncker, Fellow, IEEE, *"Temperature Rise Analysis of Switched Reluctance Motors Due to Electromagnetic Losses "*, IEEE TRANSACTIONS ON MAGNETICS, VOL. 45, NO. 7, JULY 2009.

[81] J. F. Trigeol, Y. Bertin, and P. Lagonotte, *"Coupling control volume modeling in fluid and lumped thermal model and Application to an induction machine"*, in Proc. IECONŠ06, Nov. 2006, pp. 4829Ű4834.

[82] Pfister, P.D. and Perriard, Y. (2010), *"Very high speed slotless permanent magnet motors: analytical modeling, optimization, design, and torque measurement methods"*, IEEE Transactions on Industrial Electronics, Vol. 57 No. 1, pp. 296 303.

[83] Warachart Sae kok, Pichit Lumyong, *"Characteristics Evaluation of 3 Phase Induction Motors Based on an Acceleration Method with Increasing Moment of Inertia Technique "*, SDEMPLD 2003 , USA. 24-26 August 2003.

[84] Radoslav Cipn1, Miroslav Patoka2, Ji Vondru3, *" Acceleration method of the IM torque-speed characteristics measurement"*, Proceedings of the 2011 International Conference on Power Engineering, Energy and Electrical Drives, Torremolinos (Malaga), Spain. May 2011.

[85] J.J.Gribble, P.C. Kjaer, T.J.E. Miller., *"Optimal commutation iin average torque control of switched reluctance motors "*, IEE Proc.-Electr. Power Appl., Vol 146, No. I,January 1999.

[86] Vasan Prabhu, V.; Mahesh, K.S.; Renuka, C., *" Simulation of Switched Reluctance motor/generator with optimum turn-on and turn-off control for the application of variable speed drives ",* IET Conference Publications, 2011 , Page(s): 501-506.

[87] Mademlis, C.; Kioskeridis, I. , *"Performance optimization in switched reluctance motor drives with online commutation angle control",*

[88] Takayoshi Matsuo and Thomas A.Lipo , *" Rotor position detection scheme for synchronous reluctance motor based on current measurements ",* IEEE, 1994 , Page(s): 627-635.

[89] R. T. Naayagi and V. Kamaraj, *"Shape optimization of switched reluctance machine for aerospace applications",* in Proc. 31st IEEE IECON, Nov. 2005, pp. 1748 - 1751.

[90] Xue, X.D.; Cheng, K.W.E.; Lin, J.K.; Zhang, Z.; Luk, K.F.; Ng, T.W.; Cheung, N.C., *"Optimal Control Method of Motoring Operation for SRM Drives in Electric Vehicles ",* IEEE Transactions on vehicular technology, vol. 59, NO. 3, MARCH 2010.

[91] X. D. Xue, Member, K.W. E. Cheng, T.W. Ng, and N. C. Cheung, *"Multi-Objective Optimization Design of In-Wheel Switched Reluctance Motors in Electric Vehicles ",* IEEE TRANSACTIONS ON INDUSTRIAL ELECTRONICS, VOL. 57, NO. 9, SEPTEMBER 2010.

[92] Atkinson, C.R. ; Downie, E.G. *"Acceleration-Oscillograms Method of Motor-Torque Measurment",* American Institute of Electrical Engineers, Transactions of the Volume: 61 , Issue: 1 . 1994.

[93] Simon Michael Schneider. *" Analysis and Reduction of Acoustic Noise in High Speed Switched Reluctance Motor",* Berlin, 19th January 2013.

[94] Samy Arnaout. *"Indirekte Drehmomentmessung für eine hochdrehende Geschaltete Reluktanzmaschine ",* Berlin, 13th July 2013.

[95] Christos Mademlis, Associate Member, IEEE,and Iordanis Kioskeridis *"Performance Optimization in Switched Reluctance Motor Drives With Online Commutation Angle Control ",* IEEE TRANSACTIONS ON ENERGY CONVERSION, VOL. 18, NO. 3, SEPTEMBER 2003.

[96] Savvateev A.F.; Budin A.V. *"High-speed penetration into sand",* International Journal of Impact, 1 Dec 2001.

[97] http://www.ni.com/pdf/manuals.

[98] http://www.lem.com/docs/products/LA 305-S.pdf

[99] http://www.lem.com/docs/products/LV 25-400.pdf

[100] http://www.hoskin.qc.ca/uploadpdf/Instrumentation/Staiger/Mohilo

[101] Electrical machines script, TU-Berlin.